Title
Comprehensive Pyrometry of Incandescent Multiwalled Carbon Nanotubes and Graphene in the Visible and Near Infrared

Author
Singer, Scott

Publication Date
2012

Peer reviewed|Thesis/dissertation

University of California

Los Angeles

Comprehensive Pyrometry of Incandescent Multiwalled Carbon Nanotubes and Graphene in the Visible and Near Infrared

A dissertation submitted in partial satisfaction

of the requirements for the degree

Doctor of Philosophy in Physics

by

Scott Benjamin Singer

2012

Abstract of the Dissertation

Comprehensive Pyrometry of Incandescent Multiwalled Carbon Nanotubes and Graphene in the Visible and Near Infrared

by

Scott Benjamin Singer

Doctor of Philosophy in Physics

University of California, Los Angeles, 2012

Professor Brian Christopher Regan, Chair

Pyrometry via blackbody radiation is used to measure temperature of systems throughout physics. The spectrum, described by Planck's law, depends solely on the temperature T and surface area A of a black source. However, the derivation of Planck's law considers only the limit where wavelength $\lambda \ll L$, the linear dimension of the source. Many nanosystems, however, exist in the opposite limit, $\lambda \gtrsim L$, in the visible and near infrared.

We investigate this subwavelength limit of thermal radiation by bringing multi-walled carbon nanotubes, for which $r \ll \lambda \lesssim L$, to incandescence via joule heating. Their light is measured in an optical microscope, and their geometry is measured with a transmission electron microscope. With complete knowledge of the source geometry and the photon emission, a full characterization of the temperature, thermal conductivity, and electrical conductivity of each nanofilament is possible. We find that the filaments emit highly polarized light with suprablack effective emissivities, indicative of thermal radiation originating in a phase coherent manner from the nanotube's volume as opposed to its surface area, in concordance with classical electromagnetism.

Multiwavelength pyrometry is then performed on graphene, which has linear dimensions in the classical blackbody limit and theoretical gray emission. This pyrometry allows

us to measure the number of layers in the graphene, a result confirmed with absorption measurements in agreement with Kirchoff's law of thermal radiation. Light emitted from incandescent graphene's bulk is found to be unpolarized, yet exhibits polarization as high as 20% near the sheet edge in accordance with diffraction theory. However, light polarized to 5% is observed originating from the bulk away from the hot region, which we attribute to anisotropy in the temperature gradient.

We also find that as temperature of a nanotube and graphene increases, the signal in the near infrared becomes suppressed compared to the emission models. As trapped surface states and contaminants on graphene samples shift the Fermi energy away from the Dirac point, long wavelength transitions become disallowed. Thus, this infrared effect owes to the transparency at long wavelengths of carbon nanostructures with a Fermi level shifted away from the Dirac point, implying that broadband optical modulation in the visible and near infrared is attainable through gating and heating of carbon nanotubes and graphene.

The dissertation of Scott Benjamin Singer is approved.

Shimon Weiss

Ned Wright

Eric Hudson

Brian Christopher Regan, Committee Chair

University of California, Los Angeles

2012

To Mom and Dad,

Deanne my rock,

Haley and Brooke,

and the “littles”

Corky, Joe, Hazel, and Tucker.

Table of Contents

List of Figures

List of Tables

Acknowledgments

This work could not have been done without the help of many others. First and foremost, I would like to thank my advisor Dr. Brian Chris Regan for his countless hours of guidance and numerous discussions and debates in the direction of this project. He also coded the entire Labview architechture and drivers for operating the experiment, and was integral to giving me direction in the analysis and math related to the project whenever I got stuck.

Dr. Matt Mecklenburg was essential in taking many transmission electron micrographs of the carbon nanotube devices and paving the way to the diffraction analysis of graphene. His numerous discussions regarding graphene theory were immensely helpful in graphene analysis.

I also thank Dr. Yuwei Fan for developing the initial fabrication process for the devices. Furthermore, working devices would not have been possible without her assistance with electron-beam lithography at the Integrated Systems Nanofabrication Cleanroom (ISNC) in the California NanoSystems Institute (CNSI) at UCLA.

I thank Ed White for his *in situ* transmission electron microscopy. His operation of the biasing holder as well as burning unwanted nanotube devices with the electron beam proved invaluable to producing ideal and stable nanofilaments.

Billy Hubbard pioneered the procedure for fabricating graphene nanostrips on our device architechture. The results of Chapter 6 would not be possible without his innovation. I am also thankful for his operation of the transmission electron microscope.

Thanks to Brian Shevitzky for his operation of the transmission electron microscope. His diffraction and dark field imaging of graphene sheets proved invaluable to characterizing graphene devices.

The fabrication of devices was done entirely at UCLA's Nanoelectronics Research Facility (NRF) and ISNC cleanrooms. All transmission electron microscopy was performed at the Electron Imaging Center for NanoMachines (EICN) in the CNSI.

This work was funded by NSF Career Grant No. 0748880.

Vita

2005 B.S. (Physics), California Institute of Technology

2006 M.S. (Physics), University of California, Los Angeles

2012 Staff Engineer, Advanced Technology Products, Spectrolab Inc.

Publications

Yuwei Fan, S. B. Singer, Raymond Bergstrom, and B. C. Regan, "Probing Planck's Law with Incandescent Light Emission from a Single Carbon Nanotube", *Physical Review Letters*, 102, 187402 (2009).

S. B. Singer, Matthew Mecklenburg, E. R. White, and B. C. Regan, "Polarized light emission from individual incandescent carbon nanotubes',' *Physical Review B*, 83, 233404 (2011).

Edward R. White, Matthew Mecklenburg, Scott B. Singer, Shaul Aloni, Brian Christopher Regan, "Imaging Nanobubbles in Water with Scanning Transmission Electron Microscopy", *Applied Physics Express*, 4, 055201 (2011).

S. B. Singer, Matthew Mecklenburg, E. R. White, and B. C. Regan, "Single-color pyrometry of individual incandescent multiwalled carbon nanotubes", *Physical Review B*, 84, 195468 (2011).

E. R. White, Matthew Mecklenburg, Brian Shevitski, S. B. Singer, and B. C. Regan,

"Charged Nanoparticle Dynamics in Water Induced by Scanning Transmission Electron Microscopy", *Langmuir*, 28, 3695 (2012).

CHAPTER 1

Introduction

1.1 Pyrometry

1.1.1 Planck's Law of Thermal Radiation

Max Planck's description of the thermal radiation of a "blackbody" in 1900 remains one of the most important results of physics, historically as well as scientifically. The thermal radiation spectra seen experimentally by Lummer and Pringsheim[3], and Rubens and Kurlbaum[4], had been described by Wien[5] as

$$\frac{I(\lambda,T)}{d\lambda dA} = \frac{2hc^2}{\lambda^5} e^{-C_2/\lambda T}, \tag{1.1}$$

where $I(\lambda,T)$ represents the power flux from within plane waves of wavelength between λ and $\lambda+d\lambda$ across an area dA; here $h = 6.626\times10^{-34}$ J·s is Planck's constant, $c = 2.998\times10^{17}$ nm/s is the speed of light in a vacuum, $C_2 = hc/k_B = 1.44 \times 10^7$ nm·K is the second radiation constant, and $k_B = 1.381 \times 10^{-23}$ J/K is Boltzmann's constant. Equation 1.1, known as Wien's law, fits observed thermal spectra at short wavelengths, yet underestimates it at longer wavelengths. Planck corrected Wien's law by considering the electromagnetic field inside the blackbody as a system of Hertzian oscillators with discretized energy, obtaining the well known Planck's law[6],

$$\frac{I(\lambda,T)}{d\lambda dA} = \frac{2hc^2}{\lambda^5} \frac{1}{e^{C_2/\lambda T} - 1}. \tag{1.2}$$

For oblique incidence, the effective area is modified by a Lambertian factor, $dA' = \cos\theta dA$, and the complete spatial distribution for blackbody radiation is

$$\frac{I(\lambda,T,\theta)}{d\lambda dA d\Omega} = \frac{2hc^2}{\lambda^5} \frac{\cos\theta}{e^{C_2/\lambda T} - 1}. \tag{1.3}$$

Planck's assumption of quantizing the allowed energies of electromagnetic radiation was an important step in the development of quantum physics. Furthermore, Planck's law has proved valid and unaltered since its formulation at the turn of the twentieth century.

1.1.2 Pyrometry

While many methods exist for determining the temperature of a system, ranging from measuring the shot noise[7] to observing fiducials with known melting temperatures[8], fitting thermal radiation to Planck's law is the only method with spans all the decades of accessible temperatures. The cosmic microwave background (CMB) fits a Planck spectrum corresponding to 2.725 K on average, and anisotropies in this very low temperature point to interesting physics from the early universe[9]. On the other side of the temperature scale, a Planck fit of starlight reveals that stars have surface temperatures in excess of 10^4 K. In fact, the International Temperature Scale ITS-90[10] uses Planck's law to define and standardize temperatures above 1235 K, the melting point of silver. From extremely cold to extremely hot, Eq. 1.2 can be utilized to determine the temperature of metals, plasmas, stars, and many other physical systems.

1.1.3 Challenges of Pyrometry

In practice, exact pyrometry of a thermal body proves difficult because few objects outside of stars are black to a good approximation. The absolute emission of a material is modified by its emissivity $\epsilon(\lambda, T, \Omega)$, which represents the fraction of light produced in comparison to Eq. 1.3. For a "graybody", or ϵ independent of wavelength, a fit to Planck's law is still possible; such a graybody assumption is often employed in pyrometry.

By Kirchoff's law of thermal radiation and the principle of detailed balance, this emissivity is equal to the absorptivity of the material[11]. Absorptivity is related to the complex dielectric constant ε, which is related to the optical conductivity $\sigma(\omega)$ by

$$\varepsilon = \varepsilon_\infty + i\frac{4\pi\sigma(\omega)}{\omega}, \tag{1.4}$$

where $\omega = 2\pi c/\lambda$, and ε_∞ represents the material, DC dielectric response. The optical

conductivity is directly related to the electron-photon interaction, which increases in complexity with the band structure of the material. Furthermore, absorption also depends on the surface quality of the sample, and surface roughness will alter the local reflection and transmission.

Two-color, or ratio, pyrometry circumvents this issue by comparing the intensity at two wavelengths within a range where ϵ is assumed to vary weakly with wavelength. However, the uncertainty in this method can be large[12]. An alternative method of pyrometry is to fit to a functional form of $\epsilon(\omega)$. Fitting the functionality of the emissivity directly produces errors increasing uncontrollably with the number of data points[13]; assuming a functional form for the fit does not have such errors[14], but necessitates a model for $\epsilon(\omega)$[15].

Carbon nanostructures have well-defined molecular structures, so surface inhomogenities are minimized and do not affect the absorption. Furthermore, these well-defined structures allow complete calculation of the electronic bands, and fully realized models for the emissivity can be obtained.

1.2 Carbon Nanostructures

1.2.1 Electronic Devices

Recently, carbon nanostructures have become promising materials for the fabrication of advanced electronic and optical devices. Graphene, an atomically thin sheet of sp^2 bonded carbon, is a zero-bandgap semiconductor and has mobilities in excess of 10^5 $cm^2/V \cdot s$[16], far superior to typical semiconductor technology. The performance of graphene devices is directly affected by graphene's thermal and optical properties. Its planar structure is conducive to incorporation into transistors, where the performance is restricted by current saturation. This current saturation stems from self-heating and scattering between the electrons and optical phonons[17, 18]. Graphene has been observed to emit as a graybody[19, 17, 20, 21] with emissivity 2.3% equal to its absorption in the visible[22, 23]; this broadband thermal emission allows graphene to be utilized as an optical modulator[24, 21], an optical absorber[25], or incandescent display[20].

Rolling a graphene sheet into a cylinder produces a carbon nanotube (CNT). A nanotube's electronic properties are related to its size, becoming semiconducting or metallic depending on the diameter. Since the length of a carbon nanotube is much larger than its width, it can be used as a sensitive polarization detector or source. Cylindrical and ellipsoidal carbon grains are also theorized to comprise stellar dust, which are directly observable via thermal radiation[26, 27]. The thermal response of the emission or absorption of CNTs thus has importance to astronomy as well as device physics.

1.2.2 Thermal Stability

Equation 1.3 is monotonically increasing with T; thus, higher temperatures increase the signal from an object. Materials limit the temperatures acheivable in a laboratory environment, with carbon and transition metals such as tungsten, molybdenum, and tantalum among the few with melting points near or above 3000 K in 1 atm. Referring to Eq. 1.1, the intensity peaks at $\lambda_{2000\text{ K}} \approx 1438$ nm and $\lambda_{3000\text{ K}} \approx 959$ nm. Therefore, large signal, in addition to accessibility of equipment, make it advantageous to measure light from bodies at $T \gtrsim 2000$ K in the visible and near infra-red (NIR) spectrum (ranging from ~ 300 nm to ~ 1200 nm), and both graphene[28] and carbon nanotubes[29] can be heated to this range before device failure.

1.2.3 Experimentally Accessible Subwavelength Radiators

Two distinct morphologies of carbon nanotubes exist–single-walled carbon nanotubes (SWCNTs) consisting of a single carbon layer, and multi-walled carbon nanotubes (MWCNTs) consisting of several concentric SWCNTs. SWCNTs have several quantum properties arising from their cylindrical geometry, including quantized conductance and distinct electrical subbands; this quantization leads to strong spectral peaks. On the other hand, the electronic properties of MWCNTs lie in the classical limit; MWCNTs are thus broadband spectral sources, proving optimal for using classical methods to analyze their thermal radiation.

A carbon nanotube has a typical diameter ~ 10 nm and length $\gtrsim 1$ μm; thus in the visible-NIR, $r \ll \lambda \lesssim L$, outside the typical blackbody assumption that the length scale

$r \gg \lambda$. Since CNTs have a cylindrical geometry, bringing them to incandescence via joule heating is straightforward; furthermore, the temperature profile will be described by the one-dimensional heat equation. Therefore, multi-walled carbon nanotubes make ideal candidates to probe the properties of blackbody radiation in this extraordinary size regime, where effects such as enhanced coherence[30, 31] and emission are expected.

1.3 Band Theory of Graphene and Carbon Nanotubes

1.3.1 The Graphene Lattice

The two-dimensional allotrope of carbon, graphene, provides the foundation for the physical structure of buckyballs, CNTs, and graphite. A two-dimensional network of sp^2 bonded carbon atoms forms a honeycomb lattice. This honeycomb lattice is comprised of a trigonal lattice with primitive vectors

$$\begin{aligned} \vec{a}_1 &= \frac{a_g}{2}(\sqrt{3}\hat{x} + \hat{y}) \\ \vec{a}_2 &= \frac{a_g}{2}(\sqrt{3}\hat{x} - \hat{y}) \end{aligned} \tag{1.5}$$

and basis

$$\begin{aligned} \vec{r}_1 &= -\frac{a_g}{2}\hat{x} \\ \vec{r}_2 &= \frac{a_g}{2}\hat{x}, \end{aligned} \tag{1.6}$$

where the primitive vector length a is related to the length of the C-C bond a_{C-C} by $a_g = \sqrt{3}a_{C-C} \approx 2.461$ Å. The unit cell, which has area $|\vec{a}_1 \times \vec{a}_2| = \sqrt{3}a_g^2/2$, contains 2 carbon atoms, and is illustrated in Fig. 1.1 along with the lattice and primitive vectors. We denote the two sublattices as "A" and "B", comprised of all locations $\vec{R}_A = \nu_1\vec{a}_1 + \nu_2\vec{a}_2 + \vec{r}_1$ and $\vec{R}_B = \nu_1\vec{a}_1 + \nu_2\vec{a}_2 + \vec{r}_2$ respectively for ν_1, ν_2 integers.

1.3.2 CNT Structure

We construct a single-walled carbon nanotube from graphene by imposing the periodic boundary condition equating all lattice points separated by the chiral vector $\vec{C} = n\vec{a}_1 + m\vec{a}_2$, for fixed integers n and m. This nanotube, denoted an (n, m) SWCNT, has the circumfer-

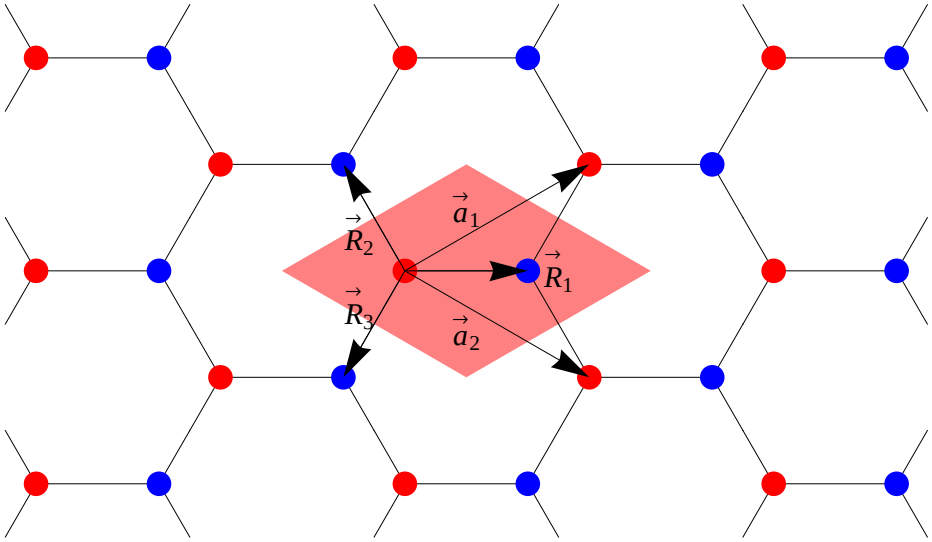

Figure 1.1: The honeycomb graphene lattice. Sublattices A and B are represented by red and blue sites, respectively, and shaded area represents the unit cell. The vectors $\vec{R}$ indicate nearest-neighbors to an atom on the A sublattice, as used in the tight-binding calculation of electronic bands.

ence $|\vec{C}| = a_g\sqrt{n^2+m^2+nm}$. The unit cell of this SWCNT is larger than graphene's unit cell, and the number of atoms per unit length[32] is

$$\frac{N}{L} = \frac{4}{\sqrt{3}a_g}\sqrt{n^2+m^2+nm} = \frac{4}{\sqrt{3}a_g^2}|\vec{C}|. \tag{1.7}$$

Several concentric single-walled nanotubes form a multi-walled carbon nanotube (MWCNT). The spacing of walls in a MWCNT equals the interlayer spacing in graphite $\delta = 3.4$ Å. A MWCNT with inner and outer radii a and b, respectively, has

$$N = \frac{8\pi}{\sqrt{3}a_g^2}\sum_{i=1}^{n}[a+(i-1)\delta] \tag{1.8}$$

carbon atoms, where $n = (b-a)/\delta$ is the number of walls. A 1 μm long SWCNT of radius 2 nm has $\approx 5\times10^5$ carbon atoms, and a 10-wall, 1 μm long MWCNT with inner and outer radii 2 nm and 5 nm has $\approx 8\times10^6$ carbon atoms. Thus, MWCNTs and SWCNTs of reasonable length exist in the large particle limit, where electron and phonon bands are continuous rather than quantized, as well as the thermodynamic limit, where temperature T is well-defined on a nanotube.

1.3.3 Thermal Phonon Lengths

With carbon nanostructures supporting a well-defined temperature, the wavelength of a typical phonon at temperature T determines the minimum length scale on which it makes sense for the temperature to vary. The thermal phonon wavelength is $\lambda_{ph} = hv_s/k_BT$ where v_s is the speed of sound. We approximate the speeds of sound in graphene and MWCNTs by the speeds of sound in graphite: $v_{TA} = 12.3$ km/s and $v_{LA} = 21.0$ km/s for the transverse and longitudinal modes, respectively[32]. Thus, $\lambda_{ph} \approx 1\ \mu\text{m}/T \approx 3$ nm at room temperature. Because typical graphene sheets and MWCNTs have lengths L on the order of several μm, $\lambda_{ph} \ll L$, and temperature gradients are also well-defined.

1.3.4 Electronic Bands of Graphene

The electronic transitions within a thermal body drive the emission of its electromagnetic radiation. The graphene lattice's simplicity and high symmetry allows direct calculation of the

electronic energy bands governing these transitions using a tight-binding model. Graphene's reciprocal lattice, shown in Fig. 1.2, is a trigonal lattice with reciprocal lattice vectors

$$\begin{aligned}\vec{b}_1 &= \frac{2\pi}{a_g}\left(\frac{\hat{x}}{\sqrt{3}} + \hat{y}\right) \\ \vec{b}_2 &= \frac{2\pi}{a_g}\left(\frac{\hat{x}}{\sqrt{3}} - \hat{y}\right).\end{aligned} \tag{1.9}$$

Electron wavevectors $\vec{k}$ can be translated to equivalent points in reciprocal space by any reciprocal lattice vector $\vec{G} = v_1\vec{b}_1 + v_2\vec{b}_2$ for v_1, v_2 integers, and thus this translation does not alter the physics of that electron. Thus, we restrict our discussion to the first Brillouin zone (BZ), also shown in Fig. 1.2 along with points of high symmetry designated the Γ, M, and K points.

The tight-binding model supposes only that an electron can "hop" from an orbital of one lattice atom onto the orbital of the atom's nearest-neighbor with some probability. For a given Hamiltonian $\hat{H}$, the probability that an electron on the A sublattice hops to one of the nearest neighbors on the B sublattice is the hopping integral

$$t = \langle\phi_A(r - R)|\hat{H}|\phi_B(r - R - a_g/2)\rangle. \tag{1.10}$$

Because the π-orbitals of the C-C bond overlap slightly, the overlap integral

$$s = \langle\phi_A(r - R)|\phi_B(r - R - a_g/2)\rangle \tag{1.11}$$

relates to the probability of the electron "belonging" to the A sublattice to begin with, and will affect the transition energies as well.

The energy bands from this method are[32]

$$E_g^{\pm}(\vec{k}) = \frac{\epsilon_{2p} \pm t\sqrt{|f(\vec{k})|^2}}{1 \pm s\sqrt{|f(\vec{k})|^2}}, \tag{1.12}$$

where ϵ_{2p} is the difference of the sublattices' $2p$ orbital energies; $\epsilon_{2p} = 0$ for graphene, but is non-zero for heterogenous honeycomb structures. The phase factor $f(\vec{k})$ sums over the phase contribution from the 3 nearest neighbors, at relative positions $\vec{R}_1$, $\vec{R}_2$, and $\vec{R}_3$ (see Fig. 1.1):

$$\begin{aligned}f(\vec{k}) &= e^{i\vec{k}\cdot\vec{R}_1} + e^{i\vec{k}\cdot\vec{R}_2} + e^{i\vec{k}\cdot\vec{R}_3} \\ &= e^{ik_x a_g/\sqrt{3}} + 2e^{-ik_x a_g/2\sqrt{3}}\cos\left(\frac{k_y a_g}{2}\right).\end{aligned} \tag{1.13}$$

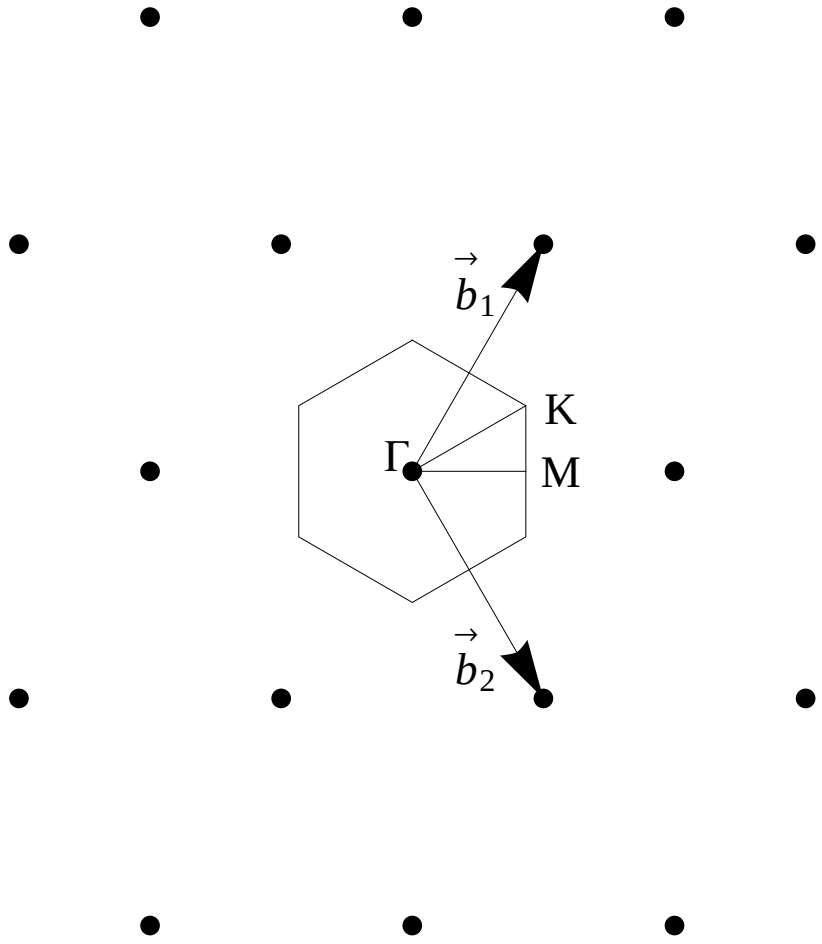

Figure 1.2: Graphene's reciprocal lattice. The first Brillouin zone (BZ) is designated, and wavevectors of high symmetry are designated as the Γ, M, and K points within the BZ.

The full solution, using the carbon-carbon π-bond values $t = -3.033$ eV and $s = 0.129$ [32] is shown in Fig 1.3. However, we are only concerned with low-energy excitations, we approximate no orbital overlap, or $s = 0$, and the energy bands of graphene are

$$E_g(\vec{k}) = \pm t \left[1 + 4\cos\frac{\sqrt{3}k_x a_g}{2}\cos\frac{k_y a_g}{2} + 4\cos^2\frac{k_y a_g}{2} \right]^{1/2}. \tag{1.14}$$

The lower and upper branches of E_g are identified with valence and conduction bands, respectively. At the K points of the Brillouin zone, $E_{\text{Dirac}} \equiv E_g^v(\vec{K}) = E_g^c(\vec{K}) = 0$. These Dirac points represent the level of half-filling for undoped graphene, and thus we set the undoped Fermi level at $E_F = E_{\text{Dirac}}$.

With $E_F = 0$, the lowest energy excitations of electrons occur near the K points. We expand $E_g(\vec{k}')$ near the K point using $\vec{k}' = \vec{K} - \vec{k}$ for small wavevectors $|\vec{k}|a_g \ll 1$. The bands become linear in $|\vec{k}|$,

$$E_g \approx \pm\frac{t a_g\sqrt{3}}{2}|\vec{k}| = \pm\hbar v_F|\vec{k}|, \tag{1.15}$$

where the Fermi velocity $v_F \equiv t a_g\sqrt{3}/2\hbar = 9.82 \times 10^5 \approx 10^6$ m/s. This linear dispersion indicates that electrons in graphene act as massless fermions that always travel at v_F. This velocity is much larger than typical electron drift velocities, resulting in the observed high mobility.

Interband electron transitions from the valence to the conduction band (or vice-versa) correspond to absorption (emission) of a photon. The photon energy for a transition is related to the promoted (demoted) electron's wavevector by $E_\gamma = 2\hbar v_F|\vec{k}|$. The matrix element corresponding to this emission or absorption determines the transition probability, and calculation of this element using the Kubo formalism[33] or tree-level Feynman diagrams[34] gives the optical conductivity of graphene

$$\sigma_g = \frac{\alpha c}{8}\left[\tanh\left(\frac{hck - 2E_F}{4k_B T}\right) + \tanh\left(\frac{hck + 2E_F}{4k_B T}\right)\right], \tag{1.16}$$

with $\alpha \approx 1/137$ the fine-structure constant and the Fermi level drives the chemical potential. For undoped graphene,

$$\sigma_g = \frac{\alpha c}{4}\tanh\left(\frac{C_2}{4\lambda T}\right), \tag{1.17}$$

which takes the wavelength and temperature independent limit $\sigma_g \approx \alpha c/4$ in the vis-NIR for $T \lesssim 2000$ K.

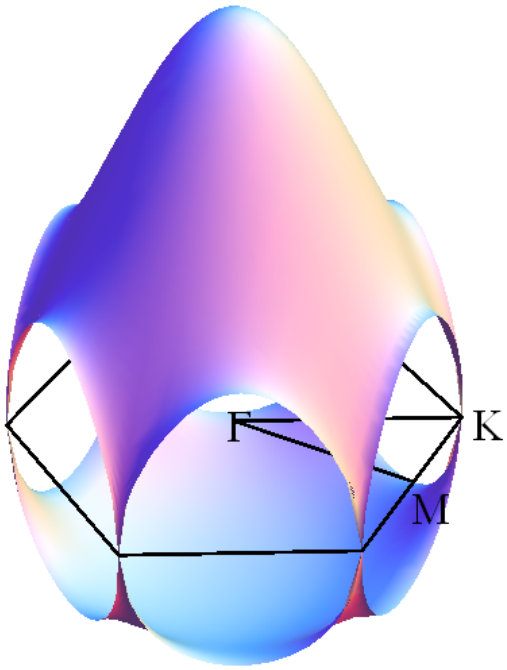

Figure 1.3: The complete valence and conduction bands of graphene shown within the BZ, solved using a tight binding model with $t = -3.033$ eV and $s = 0.129$.

1.3.5 Electrons and Holes in Graphene

As graphene is a zero-gap semiconductor, transport and subsequent heating is determined by the concentration of charge carriers. The number of charge carriers per area with $k \equiv |\vec{k}| < k_F$

$$n = \frac{g_s g_v}{4\pi(\hbar v_F)^2}|E|^2 \tag{1.18}$$

follows from Eq. 1.15 with restricting $\vec{k}$ to two dimensions. Here, $g_s = 2$ is the electron spin degeneracy and $g_v = 2$ is the valley degeneracy owing to the inequivalent K and K′ points in the BZ, which are related to each other by a rotation of 60°. Solving for E gives the Fermi level as a function of concentration

$$E_F = \pm\hbar v_F\sqrt{\pi n}, \tag{1.19}$$

taking the +(-) solution when transport is dominated by electrons (holes). Differentiation of Eq. 1.18 with respect to E gives the density of states for both electrons and holes

$$D(E) = \frac{2|E|}{\pi(\hbar v_F)^2}. \tag{1.20}$$

The total concentration of electrons n is given by integrating $D(E)$ times the Fermi-Dirac distribution from the bottom of the conduction band, and

$$\begin{aligned} n &= \int_0^\infty D(E)F(E-E_F)dE = \frac{2}{\pi(\hbar v_F)^2}\int_0^\infty \frac{EdE}{1+e^{(E-E_F)/k_BT}} \\ &= \frac{2}{\pi}\left(\frac{k_BT}{\hbar v_F}\right)^2\int_0^\infty \frac{\eta d\eta}{1+e^{\eta-\eta_F}}, \end{aligned} \tag{1.21}$$

where $\eta \equiv E/k_BT$ and $\eta_F \equiv E_F/k_BT$. Similarly, the concentration of holes is found by integrating to the top of the valence band,

$$\begin{aligned} p &= \int_{-\infty}^0 D(E)F(E-E_F)dE = \frac{2}{\pi(\hbar v_F)^2}\int_{-\infty}^0 \frac{|E|dE}{1+e^{(E-E_F)/k_BT}} \\ &= \frac{2}{\pi}\left(\frac{k_BT}{\hbar v_F}\right)^2\int_0^\infty \frac{\eta d\eta}{1+e^{\eta+\eta_F}}. \end{aligned} \tag{1.22}$$

For pristine, undoped graphene, $E_F = 0$ and the integral evaluates to $\pi^2/12$. Therefore, the intrinsic electron and hole densities of graphene are

$$n = p = n_i \equiv \frac{\pi}{6}\left(\frac{k_BT}{\hbar v_F}\right)^2, \tag{1.23}$$

which increases quadratically with temperature. At $T = 300$ K, $n_i \approx 8.4 \times 10^{10}$ cm^{-2}.

1.3.6 Electronic Bands of CNTs

The electronic energy bands of a SWCNT derive from the band structure of graphene by application of the SWCNT's periodic boundary condition. The wavefunction of an electron with wavevector $\vec{k}$ obeys the Bloch condition

$$\phi_{\vec{k}}(\vec{r}+\vec{R}) = e^{i\vec{k}\cdot\vec{R}}\phi_{\vec{k}}(\vec{r}) \tag{1.24}$$

for any lattice vector $\vec{R}$. When this lattice vector is the chiral vector, $\vec{r}+\vec{C}=\vec{r}$, the single-valuedness of the wavefunction requires $e^{i\vec{k}\cdot\vec{C}}=1$, or $\vec{k}\cdot\vec{C}=2\pi q$ for integers q. Substituting $\vec{C}=n\vec{a}_1+m\vec{a}_2$, this equation places the restriction on the allowed wavevectors,

$$\sqrt{3}k_x(n+m)+k_y(n-m)=\frac{4\pi q}{a_g}. \tag{1.25}$$

There are $2n+m$ distinct subbands formed by applying this restriction to Eq. 1.14 in the BZ of graphene; these bands are designated by $q \in -\lfloor\frac{2n+m}{3}\rfloor,\ldots,-1,0,1,\ldots,\lfloor\frac{2n+m}{3}\rfloor$ and are perpendicular to $\vec{C}$. Figure 1.4 shows these subbands for a (9,5) SWCNT.

In comparison with graphene, which has no bandgap, the lowest subband of a SWCNT will exhibit an energy gap relative to its proximity to the K point. For $2n+m$ divisible by 3, the K points lie on one of the subbands, and a (n,m) nanotube is metallic or semi-metallic as opposed to semiconducting. Thus chirality restricts the energy levels available for excitations in single-walled nanotubes. Because intersubband transitions correspond to excitations along the nanotube's circumference and intrasubband transitions correspond to excitations along the tube length, we expect strong and polarization-dependent spectral contributions at these transition energies.

As the diameter of the SWCNT increases, $2n+m$ grows large, and the separation between subbands decreases. The proximity of subbands to the K points increases as well. A SWCNT of ~ 1 nm diameter has ~ 50 subbands, approaching this metallic limit. Similarly, as the number of walls increases in a MWCNT, the accessible Brillouin zone approaches that of graphene. Figure 1.5 shows the subbands for a (85,65) SWCNT, which has diameter ~ 10 nm comparable with the average wall diameter of a MWCNT; the subbands become dense in the Brillouin zone, the Dirac points are always on allowed bands, and the tube is metallic.

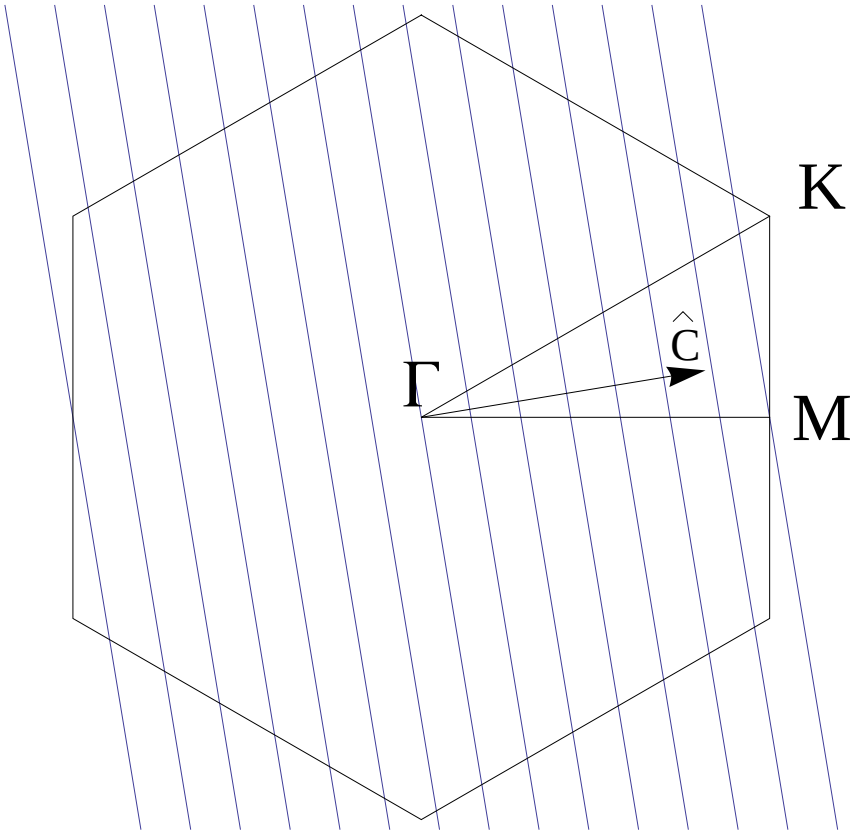

Figure 1.4: The allowed wavevectors of a (9,5) SWCNT. The $2n + m$ subbands are spaced along the chiral vector $\hat{C}$, which has been rescaled for display purposes.

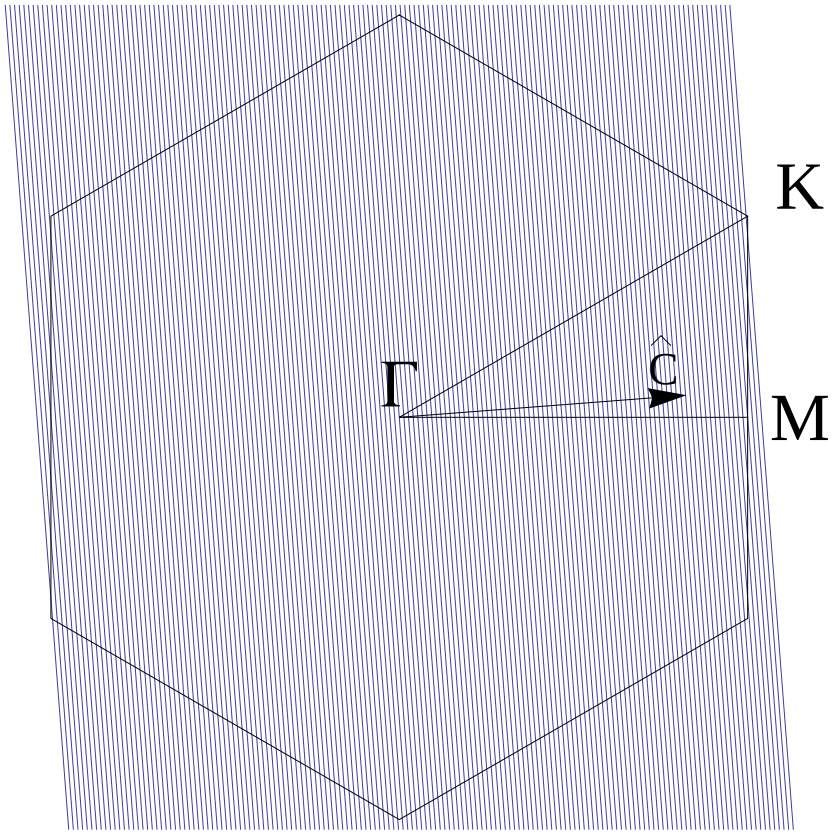

Figure 1.5: The allowed wavevectors of an (85,65) SWCNT. Almost the entire Brillouin zone of graphene is accessible.

Once interwall interactions are considered as well, the electrons in a MWCNT can take on practically any wavevector. Thus, the very metallic MWCNTs no longer have quantization conditions on allowed electronic energy states. We can treat a MWCNT of even a small number of walls and diameter $\gtrsim 7$ nm as interacting with electromagnetic waves classically, supporting a well-defined temperature gradient, and having the optical response of graphene. Thus, using classical thermodynamics and electrodynamics, we can perform a direct analysis of thermal radiation from a MWCNT with a radius much smaller than visible wavelengths.

CHAPTER 2

Thermal Radiation Theory of MWCNT Nanofilaments

2.1 Joule Heating a Filament to Incandescence

A MWCNT nanofilament emits thermal radiation in the visible-NIR spectrum at high temperatures, and its analysis requires a complete theoretical model of the spectral and directionality of this light. This thermal radiation is generated by applying a bias across the filament, raising the tube's temperature via Joule heating and bringing it to incandescence. The nanotube's ends contact large heat sinks kept at room temperature; thus, we expect a large temperature gradient from the tube's center to its end, a length which is of the order of the wavelength of visible-NIR light. On the other hand, a macroscopic filament, such as a tungsten wire in everyday incandescent bulbs, supports a constant temperature distribution over the majority of its length. The temperature distribution along the MWCNT, which directly affects the amount of light radiated, is described by the 1-D heat equation.

2.1.1 1-D Heat Equation

Because its radii $b, a \ll L$ the length, a MWCNT joule-heated by a current I can be treated as a one-dimensional wire with heat flowing only along the tube-axis, denoted $\hat{x}$ without loss of generality. Considering an infinitesimal segment spanning $[x, x+dx]$, with resistivity $\rho(x)$ and thermal conductivity $\kappa(x)$, the rate of heat flux $\dot{q}_{\text{cond}}$ through this segment by conduction is given by Fourier's Law,[35]

$$\dot{q}_{\text{cond}} = -\kappa(x)\frac{dT}{dx}, \tag{2.1}$$

or in differential form,

$$d\dot{q}_{\text{cond}} = -d\left(\kappa(x)\frac{dT}{dx}\right). \tag{2.2}$$

The units of $\dot{q}$ are power/area, so the differential heat flux due to Joule heating across the cross-sectional area $\pi(b^2 - a^2)$ is

$$d\dot{q}_{\text{heat}} = \frac{dP}{\pi(b^2 - a^2)} = \frac{I^2 dR}{\pi(b^2 - a^2)} = \frac{I^2 \rho(x)}{(\pi(b^2 - a^2))^2} dx. \tag{2.3}$$

In steady-state, the heat loss through conduction is equal to the heat gain through Joule heating, and in equating Eq. 2.2 and Eq. 2.3, we arrive at the steady state 1-D heat equation

$$\frac{d}{dx}\left(\kappa(x)\frac{dT}{dx}\right) + \rho(x)\frac{I^2}{(\pi(b^2 - a^2))^2} = 0. \tag{2.4}$$

We estimate the time required for a MWCNT to reach steady-state by comparing the input power to the power necessary to raise the nanotube to some temperature,

$$RI^2 = N\frac{C_V T}{\tau}, \tag{2.5}$$

where $C_V \approx 300$ J/mol·K is the high temperature heat capacity for graphite.[36] Using typical values of $R = 10$ kΩ, $I = 100$ μA, and $N = 10^8$ atoms, the nanotube reaches a temperature of 2000 K in no longer than $\tau \approx 1$ μs. A MWCNT filament reaches steady-state very fast compared to a typical measurement time of 1/60 s, the time of one powerline cycle (plc).

The heated MWCNT radiates light, and thus radiation must also be considered a source of heat loss to the wire. Radiative heat loss per area is given by the Stefan-Boltzmann law

$$d\dot{q}_{\text{rad}} = -\frac{(2\pi b)\epsilon\sigma_{\text{SB}}(T^4 - T_0^4)}{\pi(b^2 - a^2)}, \tag{2.6}$$

where T_0 is the temperature of the environment, ϵ is the effective emissivity, and $\sigma_{\text{SB}} = 5.67 \times 10^{-8}$ $\frac{\text{J}}{\text{m}^2\text{K}^4\text{s}}$ is the Stefan-Boltzmann constant. Comparing Eq. 2.6 to Eq. 2.2, the temperature at which radiative cooling becomes important is

$$T \sim \sqrt[3]{\frac{b\kappa}{2\sigma_{\text{SB}}(dx)^2}}. \tag{2.7}$$

For a typical nanotube, $b \sim 10$ nm, $\kappa \sim 100$ $\frac{\text{W}}{\text{m·K}}$, and we take $dx \sim \lambda_T \sim 1$ nm, resulting in a crossover temperature $T \sim \sqrt[3]{10^{19}\ \text{K}^3} \sim 10^6$ K. Therefore, at our operating temperatures, radiative cooling can be neglected. The resultant form of the heat equation in Eq. 2.4 supports analytic solutions for simple T-dependence of the ratio ρ/κ.

2.1.2 Constant Resistivity Solution

As a first approximation, we suppose both the thermal conductivity and resistivity are constant: $\kappa(x) = \kappa_0$ and $\rho(x) = \rho_0$. Then Eq. 2.4 can be integrated with respect to x twice to find

$$T(x) = \frac{-I^2\rho_0}{2\kappa_0(\pi(b^2-a^2))^2}x^2 + A_1x + A_2. \tag{2.8}$$

Applying the boundary conditions that the endpoints of the nanotube are at room temperature, $T(-L/2) = T(L/2) = T_0$, allows us to solve for the integration constants and find

$$\begin{aligned} T(x) &= \frac{I^2\rho_0}{2\kappa_0(\pi(b^2-a^2))^2}\left(\frac{L^2}{4} - x^2\right) + T_0 = T_{\max} + (T_0 - T_{\max})\left(\frac{2x}{L}\right)^2, \\ \text{with } T_{\max} &\equiv T_0 + \frac{I^2L^2\rho_0}{8\kappa_0(\pi(b^2-a^2))^2} \end{aligned} \tag{2.9}$$

the maximum temperature, reached at the tube center $x = 0$. Such a quadratic profile has been observed for Joule-heated CNTs using spatially-resolved Raman spectrography.[37, 38]

We also note that $T_{\max}$ can be written as a linear function of the power P dissipated along the nanotube,

$$T_{\max}(P) = T_0 + \frac{L}{8\kappa_0\pi(b^2-a^2)}P = T_0 + \alpha_\kappa P. \tag{2.10}$$

One obtains the thermal conductivity from the slope α_κ and the tube's geometry by

$$\kappa_0 = \frac{L}{8\pi(b^2-a^2)\alpha_\kappa}. \tag{2.11}$$

One assumption of this model is that the current-voltage response of the MWCNT is Ohmic. However, CNTs have been shown to have non-linear I-V responses,[39, 40] so we look to a more complex model of the nanotube's thermal behavior.

2.1.3 Linear Resistivity Solution

The electrical behavior of a biased MWCNT is more accurately predicted by solving Eq. 2.4 assuming constant thermal conductivity and resistivity linear with temperature, *i.e.*

$$\rho(x) = \rho_0\left(1 + \frac{T(x) - T_0}{T_\rho}\right) \tag{2.12}$$

where T_ρ is the CNT's temperature coefficient with units of K. Equation 2.4 takes the form

$$\frac{d^2T}{dx^2} + \frac{\rho_0 I^2}{\kappa_0(\pi(b^2-a^2))^2 T_\rho}(T - T_0 + T_\rho) = \frac{d^2v}{dx^2} + \frac{\rho_0 I^2}{\kappa_0(\pi(b^2-a^2))^2 T_\rho} v = 0, \tag{2.13}$$

which is simply the wave equation in $v \equiv T - T_0 + T_\rho$. This equation has solution

$$\begin{aligned} v(x) &= A_1 \cos(BIx) + A_2 \sin(BIx), \\ \text{where } B &\equiv \frac{1}{\pi(b^2-a^2)} \sqrt{\frac{\rho_0}{\kappa_0 T_\rho}}. \end{aligned} \tag{2.14}$$

Applying the same boundary conditions as before gives the temperature profile

$$T(x) = T_0 + T_\rho \left[\frac{\cos(BIx)}{\cos(BIL/2)} - 1 \right]. \tag{2.15}$$

Plugging $T(x)$ back into Eq. 2.12 yields the resistivity profile

$$\rho(x) = \rho_0 \frac{\cos(BIx)}{\cos(BIL/2)}. \tag{2.16}$$

Because the nanotube is comprised of elements $[x, x+dx]$ with resistivity $\rho(x)$, it is modeled as a chain of infinitesimally short resistors in series. Integration of the resistivity profile along the tube gives the total resistance

$$R(I) = \int_{-L/2}^{L/2} dR = \int_{-L/2}^{L/2} \frac{\rho(x)}{\pi(b^2-a^2)} dx = \frac{2\rho_0}{\pi(b^2-a^2)BI} \tan(BIL/2), \tag{2.17}$$

application of Ohm's law to which gives the voltage drop across the tube as a function of current,

$$V(I) = \frac{2\rho_0}{\pi(b^2-a^2)B} \tan(BIL/2). \tag{2.18}$$

When $\cos(BIL/2) = 0$, a singularity arises in the temperature, resistivity, resistance, and V-I profile. This singularity manifests as current saturation of the nanotube[39] at

$$I_s = \frac{\pi^2(b^2-a^2)}{L} \sqrt{\frac{\kappa_0 T_\rho}{\rho_0}}. \tag{2.19}$$

For devices studied, this saturation current is on the order of ~ 100 μA, and using typical values of $\kappa_0 = 100$ $\frac{\text{W}}{\text{m K}}$[39, 41, 8] and $\rho_0 = 10^{-5}$ $\Omega \cdot$ m, a 1 μm long and 20 nm wide tube will have temperature coefficient $T_\rho \approx 100$ K.

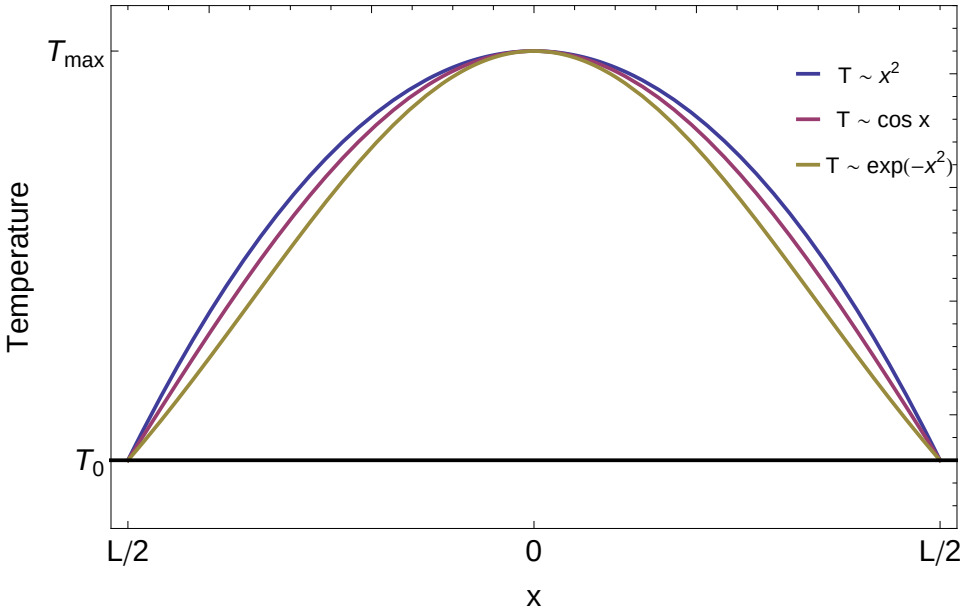

Figure 2.1: Plot of quadratic temperature profile of Eq. 2.9, cosine temperature profile of Eq. 2.15, and Umklapp solution temperature profile of Eq. 2.22. The quadratic solution is a good approximation to the other two solutions, especially near the hottest section around $x = 0$.

2.1.4 Umklapp scattering

The thermal conductivity of CNTs, however, is not constant. In fact, at temperatures above room temperature, the thermal conductivity is dominated by Umklapp scattering,[8] which has the form

$$\kappa(x) = \frac{\kappa_0}{1 + \frac{T - T_0}{T_\kappa}}. \tag{2.20}$$

Once again assuming constant resistivity, the heat equation becomes

$$\begin{aligned} 0 &= \frac{d}{dx}\left(\kappa(x)\frac{dT}{dx}\right) + \frac{P}{(\pi(b^2 - a^2))L} \\ &= \kappa_0 T_\kappa \frac{d^2}{dx^2} \log\left(1 + \frac{T - T_0}{T_\kappa}\right) + \frac{P_0}{(\pi(b^2 - a^2))L}, \end{aligned} \tag{2.21}$$

which is directly integrable in terms of $\log\left(1 + \frac{T - T_0}{T_\kappa}\right)$. The temperature distribution is

$$T(x) = T_\kappa \exp\left[\frac{PL}{8\pi(b^2 - a^2)\kappa_0 T_\kappa}\left(1 - \frac{4x^2}{L^2}\right)\right] - T_\kappa + T_0, \tag{2.22}$$

with maximum

$$T_{\max}(P) = T_\kappa \exp\left[\frac{PL}{8\pi(b^2 - a^2)\kappa_0 T_\kappa}\right] - T_\kappa + T_0. \tag{2.23}$$

Compared to Eq. 2.10, the power response is no longer linear, but depends on only the two parameters κ_0 and T_κ, which can be extracted from a direct fit with holding $T_0 = 300$ K.

The temperature profiles given by Eqs. 2.9, 2.15, and 2.22 are compared in Fig. 2.1. The quadratic solution will overestimate the temperature as compared to the cosine or Umklapp solutions, but the variations are small ($< 1\%$) in the center of the length and worst ($\sim 10\%$) near the contacts. In fact, the average error over the middle half of the tube is only $\sim 1.6\%$ compared to the cosine solution and $\sim 4\%$ compared to the Umklapp solution. Because the hottest parts of the nanotube are in the center and will contribute most to the thermal radiation, we model the nanotube's temperature profile as a parabola with minimal error, while describing the I-V response using the linear resistivity model and $T_{\max}(P)$ considering Umklapp scattering.

2.2 Radiation Profile of a Nanofilament

2.2.1 The Absorption Cross-section

The heat equation solution for a MWCNT filament has a temperature which varies very quickly on a length scale much smaller than optical wavelengths; an analytic solution to how Planck's law translates this temperature profile into radiation requires careful extension into the subwavelength regime. Because the energy carried by each photon in the wavelength range $[\lambda, \lambda + d\lambda]$ is hc/λ, Planck's Law in Eq. 1.3 can be rewritten as the photon rate

$$\dot{N}^p = \frac{c}{\lambda^4} \frac{d\lambda d\Omega dA}{e^{C_2/\lambda T} - 1}, \tag{2.24}$$

with the superscript p designating the polarization. Integrating over the surface, a macroscopic thermal object with emissivity ϵ will radiate at the rate

$$\dot{N}^p = A\epsilon \frac{c}{\lambda^4} \frac{d\lambda d\Omega}{e^{C_2/\lambda T} - 1}. \tag{2.25}$$

The combination $A\epsilon$ is identified as the emission cross-section $C^p_{em}(\lambda, \Omega)$, as it represents the effective area of the surface emitting radiation as compared to a blackbody. Invoking detailed balance and Kirchoff's law of thermal radiation, the $C^p_{em}(\lambda, \Omega) = C^p_{\text{abs}}(\lambda, \Omega)$, the absorption cross-section. Even subwavelength particles have a well-defined absorption cross-section, providing the link between two disparate size regimes.

2.2.2 Geometric Optics vs. Boundary Value Absorption

If we consider an object with linear dimension $d > \lambda$, we say we are in the geometric optics limit, and the geometric cross-sectional area A captures the fraction of all photons incident on the surface equal to its emissivity ϵ. This picture is the typical one for a thermal body, and a blackbody represents the ultimate bound on thermal radiation on these scales; thus, $0 \leq \epsilon \leq 1$ and $C^p_{\text{abs}} \leq A$. Each element of area dA contributes to the radiation independently, and any body supporting a temperature gradient or emissivity gradient across the surface can be treated as the superposition of many radiating surfaces.

An object that has one or more dimension $\lesssim \lambda$ is in the opposite limit of relative scale; nanofilaments are in this regime for wavelengths in the visible-NIR. Instead of the energy

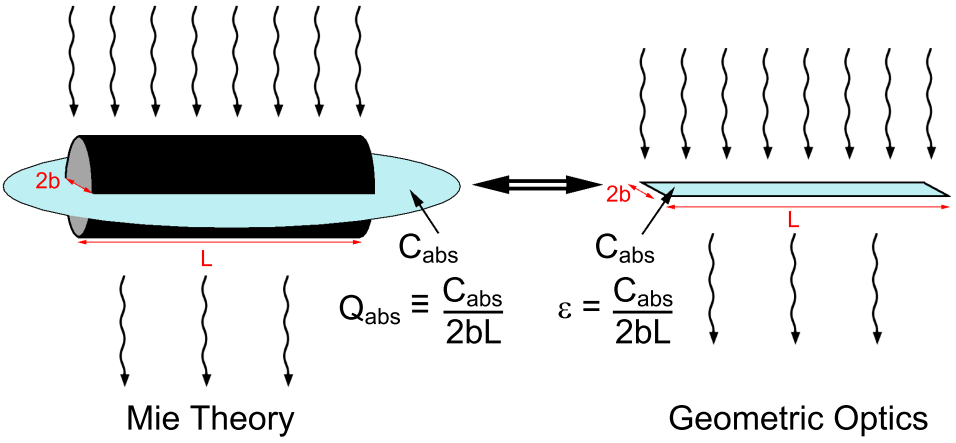

Figure 2.2: Illustration of the relationship between the boundary value problem and geometric optics paradigms of absorption by an object. The cross-sections C_{abs} both represent the effective projected absorbing area, and the absorption coefficient Q_{abs} and emissivity ϵ are analogous, although Q_{abs} has no upper bound.

being absorbed by an element of surface area, the entire volume contributes to absorption. This absorption is obtained from the classical solution to a boundary value scattering problem in electrodynamics.[42] As in geometric optics, the cross-section is C^p_{abs} is well-defined; unlike the geometric optics case, however, the absorption coefficient, defined by $Q^p_{\text{abs}}(\Omega) \equiv C^p_{\text{abs}}(\Omega)/A$, can have values > 1.[43]

These geometric optics and boundary value pictures represent differing paradigms of emission; the former supposes the emission is solely determined by the surface and that each element of surface area emits independently, whereas the latter supposes emission by the entire volume as a whole. Nevertheless, these two pictures are equivalent through their analogous cross-sections–the amount of light radiated by a small particle is equivalent to the amount radiated by a surface with the same geometric cross-sectional area and emissivity $\epsilon = Q^p_{\text{abs}}$–and analysis can be performed by treating a small object as a surface, as illustrated in Fig. 2.2.

2.2.3 Photon Emission of a Nanofilament with a Quadratic Thermal Gradient

We thus project the nanotube onto a plane as a rectangle of length L and width $2b$ with emissivity $Q_{\rm abs}$ and apply Planck's law as usual. We define coordinates (l, w) on this plane, with the nanotube's axis oriented in the $\hat{l}$ direction. The rate of photons within a bandwidth $\Delta\lambda$ about λ that this plane emits into $d\Omega$ from area element $[l, l+dl] \times [w, w+dw]$

$$d\dot{N}^p(l,w) = \frac{c\Delta\lambda}{\lambda^4} Q^p_{\rm abs}(\Omega) H(l-L/2) H(l+L/2) H(w-b) H(w+b) \frac{dl dw}{e^{C_2/\lambda T(l)-1}} d\Omega, \quad (2.26)$$

where $H(u)$ is the Heaviside step function.

The total radiation is obtained from Eq. 2.26 by integrating over the entire plane,

$$\dot{N}^p = \iint_{-\infty}^{\infty} d\dot{N}^p(l,w) = \frac{2bc\Delta\lambda}{\lambda^4} Q^p_{\rm abs}(\Omega) d\Omega \int_{-L/2}^{L/2} \frac{dl}{e^{C_2/\lambda T(l)-1}}, \quad (2.27)$$

the w-integral resulting in the multiplicative factor $2b$. The amount of photons from the incandescent MWCNT reduces to an integral over a temperature profile-dependent Planck factor. In the visible-NIR spectrum, and at $T \lesssim 10^4$ K, $\exp[C_2/\lambda T] \gg 1$, and it is appropriate to take the Wien approximation $(\exp[C_2/\lambda T] - 1)^{-1} \approx \exp[-C_2/\lambda T]$.

The Planck factor becomes large as T becomes large, so the integral is dominated by the length over which the temperature profile is highest. We thus expand the temperature profile of Eq. 2.9 about $l = 0$, such that

$$\frac{1}{T(l)} \approx \frac{1}{T_{\rm max}} \left[1 + \frac{T_{\rm max} - T_0}{T_{\rm max}} \left(\frac{2l}{L} \right)^2 \right]. \quad (2.28)$$

The l integral becomes

$$\begin{aligned} \int_{-L/2}^{L/2} \frac{dl}{e^{C_2/\lambda T(l)-1}} &\approx \int_{-L/2}^{L/2} e^{-C_2/\lambda T_{\rm max}} \exp\left[-\frac{C_2(T_{\rm max}-T_0)}{\lambda T_{\rm max}^2} \left(\frac{2l}{L} \right)^2 \right] \\ &= \sqrt{\frac{\lambda T_{\rm max}^2 L^2}{4C_2(T_{\rm max}-T_0)}} e^{-C_2/\lambda T_{\rm max}} \int_{-u_0}^{u_0} e^{-u^2} du \\ &= \sqrt{\frac{\pi\lambda T_{\rm max}^2 L^2}{4C_2(T_{\rm max}-T_0)}} e^{-C_2/\lambda T_{\rm max}} {\rm erf}(u_0), \end{aligned} \quad (2.29)$$

where $u_0 \equiv \sqrt{C_2(T_{\rm max}-T_0)/\lambda T_{\rm max}^2}$. Because we are in the Wien approximation, $u_0 \gg 1$ always, and ${\rm erf}(u_0) \to 1$. The total photon flux originating from the incandescent MWCNT

is

$$\dot{N}^p = Q^p_{\text{abs}}(\Omega)\frac{2bc\Delta\lambda}{\lambda^3}\frac{L}{\lambda}\sqrt{\frac{\lambda T_{\max}}{C_2}\frac{\pi T_{\max}}{4(T_{\max}-T_0)}}e^{-C2/\lambda T_{\max}}d\Omega. \tag{2.30}$$

Obtaining $Q^p_{\text{abs}}(\Omega)$ from a standard electrodynamic boundary value problem thus completely determines the MWCNT's radiation profile.

2.3 Mie Theory of MWCNT Absorption

2.3.1 Mie Theory of Classical Electrodynamics

The absorption coefficients Q_{abs}, representing the ratio of absorbed energy to incident energy, are determined classically by the Mie theory of a scattered electromagnetic wave. The electromagnetic fields must solve the vector wave equation $\nabla^2\vec{\Psi} - k^2\vec{\Psi} = 0$. A plane wave of wavevector $k = 2\pi/\lambda$ is incident on a particle, which both scatters and absorbs some of the incident power. The extinction coefficient Q_{ext} represents the total energy lost from the incident plane wave, and the scattering coefficient Q_{sca} is the fraction of that energy lost to scattering. The absorption is found by $Q_{\text{abs}} = Q_{\text{ext}} - Q_{\text{sca}}$. These coefficients are in analogy to the transmission, reflection, and absorption coefficients of planar geometry by

$$\begin{aligned} 1 - Q_{\text{ext}} &\longleftrightarrow T, \\ Q_{\text{sca}} &\longleftrightarrow R, \\ Q_{\text{abs}} = Q_{\text{ext}} - Q_{\text{sca}} &\longleftrightarrow A = 1 - T - R. \end{aligned} \tag{2.31}$$

Mie theory is often utilized for modeling the scattering of small particles, particularly gold nanoparticles[44] and interstellar dust.[27, 45] These models typically assume a spherical geometry, although some models treat interstellar dust as solid cylinders[27] or ellipsoids.[46, 26] Because a MWCNT consists of several SWCNTs of non-vanishing diameter, the MWCNT has a core region with the same optical constants as the medium. Thus, we apply Bohren and Huffman's treatment of Mie scattering for solid cylinders[43] to the particular case of a hollow cylinder representing a MWCNT.

2.3.2 Electromagnetic Fields of the MWCNT

Treating the MWCNT as an infinite cylinder, the wave equation can be easily separated in cylindrical coordinates (r, ϕ, z). Vector wave solutions are obtained from curling the solutions of the scalar wave equation around a "pilot" vector $\hat{p}$: *i.e.* $\Psi = \vec{\nabla} \times \hat{p}\psi$ where $\nabla^2\psi - k^2\psi = 0$. In cylindrical coordinates, the scalar wave equation

$$\frac{1}{r}\frac{\partial}{\partial r}\left(r\frac{\partial \psi}{\partial r}\right) + \frac{1}{r^2}\frac{\partial^2 \psi}{\partial \phi^2} + \frac{\partial^2 \psi}{\partial z^2} + k^2\psi = 0, \tag{2.32}$$

has solutions

$$\psi_n(r, \phi, z) = Z_n^{(j)}(\rho)e^{in\phi}e^{ihz}, \;\; n \in \mathbb{Z} \tag{2.33}$$

where $Z_n^{(j)}(\rho)$ solves the cylindrical Bessel equation and $\rho = r\sqrt{k^2 - h^2}$. The superscript (j) indicates which solution to use:

$$\begin{aligned} Z_n^{(1)}(\rho) &= J_n(\rho), & Z_n^{(2)}(\rho) &= Y_n(\rho) \\ Z_n^{(3)}(\rho) = H_n^{(1)}(\rho) &= J_n(\rho) + iY_n(\rho), & Z_n^{(4)}(\rho) = H_n^{(2)}(\rho) &= J_n(\rho) - iY_n(\rho), \end{aligned} \tag{2.34}$$

where $J(\rho)$ $(Y(\rho))$ is the cylindrical Bessel function of the first (second) kind. An orthogonal set of vector wave solutions solutions are

$$\vec{M}_n^{(j)} = \vec{\nabla} \times (\hat{p}\psi_n) \text{ and } \;\; \vec{N}_n^{(j)} = \frac{\vec{\nabla} \times \vec{M}_n^{(j)}}{k}, \tag{2.35}$$

which are additionally related by $\vec{M}_n^{(j)} = \frac{\vec{\nabla} \times \vec{N}_n^{(j)}}{k}$. Choosing $\hat{p} = \hat{e}_z$ results in the vector harmonics

$$\begin{aligned} \vec{M}_n^{(j)} &= \sqrt{k^2 - h^2}e^{i(n\phi + hz)}\left(in\frac{Z_n^{(j)}(\rho)}{\rho}\hat{e}_r - Z_n^{(j)\prime}(\rho)\hat{e}_\phi\right) \\ \vec{N}_n^{(j)} &= \frac{\sqrt{k^2 - h^2}}{k}e^{i(n\phi + hz)}\left(ihZ_n^{(j)\prime}(\rho)\hat{e}_r - hn\frac{Z_n^{(j)}(\rho)}{\rho}\hat{e}_\phi + \sqrt{k^2 - h^2}Z_n^{(j)}(\rho)\hat{e}_z\right). \end{aligned} \tag{2.36}$$

We can now expand the electromagnetic fields interacting with a CNT in terms of $\vec{M}_n$ and $\vec{N}_n$. We consider an infinite cylindrical tube oriented with its long axis in the z-direction, having inner and outer radii a and b, respectively, and with complex index of refraction m. A plane wave of polarization $\hat{\epsilon}$ propagating in the x-z plane and incident on the cylinder at an angle ζ as measured from the z-axis, as illustrated in Fig. 2.3, is

$$\vec{E}_i = \hat{\epsilon}E_0 e^{-ik(r\sin\zeta\cos\phi + z\cos\zeta)} = \sum_{n=-\infty}^{\infty} A_n\vec{M}_n^{(1)} + B_n\vec{N}_n^{(1)}. \tag{2.37}$$

Multiplying both sides by $e^{-in\phi}$, and integrating over ϕ, we can use the relations

$$\begin{aligned}
\int_0^{2\pi} d\phi e^{-i[n\phi+kr\sin\zeta\cos\phi]} &= 2\pi(-i)^n J_n(kr\sin\zeta) \\
\int_0^{2\pi} d\phi e^{-i[n\phi+kr\sin\zeta\cos\phi]}\cos\phi &= 2\pi i(-i)^n J_n'(kr\sin\zeta) \\
\int_0^{2\pi} d\phi e^{-i[n\phi+kr\sin\zeta\cos\phi]}\sin\phi &= \frac{2\pi(-i)^n n}{kr\sin\zeta} J_n(kr\sin\zeta)
\end{aligned} \tag{2.38}$$

and solve for A_n and B_n. Comparison of the exponentials gives $h = -k\cos\zeta$, which allows us to simplify the harmonics:

$$\begin{aligned}
\vec{M}_n^{(j)} &= e^{i(n\phi+hz)}\frac{k}{x}\left(inZ_n^{(j)}(\mu x)\hat{e}_r - \mu x Z_n^{(j)\prime}(\mu x)\hat{e}_\phi\right), \\
\vec{N}_n^{(j)} &= e^{i(n\phi+hz)}\frac{k}{mx}\left(i\mu x Z_n^{(j)\prime}(\mu x)\hat{e}_r - n\cos\zeta Z_n^{(j)}(\mu x)\hat{e}_\phi + \mu^2 x Z_n^{(j)}(\mu x)\hat{e}_z\right),
\end{aligned} \tag{2.39}$$

where $x \equiv kr$, $\mu \equiv \sqrt{m^2 - \cos^2\zeta}$, and $\nu \equiv \sin\zeta$.

The incident wave is composed of a "parallel" polarized wave, with electric field in the x-z plane, and a "perpendicular" polarized wave, with electric field in the y direction. In terms of the incident angle,

$$\begin{aligned}
\hat{\epsilon}^{||} &= \hat{e}_z\sin\zeta - \hat{e}_x\cos\zeta = -\hat{e}_r\cos\zeta\cos\phi + \hat{e}_\phi\cos\zeta\sin\phi + \hat{e}_z\sin\zeta \\
\hat{\epsilon}^{\perp} &= \hat{e}_y = \hat{e}_r\sin\phi + \hat{e}_\phi\cos\phi.
\end{aligned} \tag{2.40}$$

Plugging these unit vectors into Eq. 2.37 and utilizing Eqs. 2.38, we find A_n and B_n for both polarizations, and the incident fields can be written

$$\begin{aligned}
\vec{E}_i^{||} &= \textstyle\sum_{n=-\infty}^{\infty} E_n N_n^{(1)} \qquad \vec{H}_i^{||} = \frac{-i}{Z_0}\sum_{n=-\infty}^{\infty} E_n M_n^{(1)} \\
\vec{E}_i^{\perp} &= -i\textstyle\sum_{n=-\infty}^{\infty} E_n M_n^{(1)} \quad \vec{H}_i^{\perp} = \frac{-1}{Z_0}\sum_{n=-\infty}^{\infty} E_n N_n^{(1)}
\end{aligned} \tag{2.41}$$

with $E_n = E_0(-i)^n/k\sin\zeta$ and $Z_0 = 4\pi/c$ the impedance of free space.

Waves that are scattered off the tube will be outward-traveling cylindrical waves at large r from the tube. As such, we expand the scattered fields in terms of the Hankel function of the first kind:

$$\vec{E}_s^p = -\textstyle\sum_{n=-\infty}^{\infty} E_n(b_n^p\vec{N}_n^{(3)} + ia_n^p\vec{M}_n^{(3)}) \quad \vec{H}_s^p = \frac{i}{Z_0}\sum_{n=-\infty}^{\infty} E_n(b_n^p\vec{M}_n^{(3)} + ia_n^p\vec{N}_n^{(3)}), \tag{2.42}$$

the superscript p indicating the polarization of the incident wave. Within the nanotube itself, there exist two regions–internal to the CNT ($a < r < b$) and the vacuum core ($0 \le r < b$).

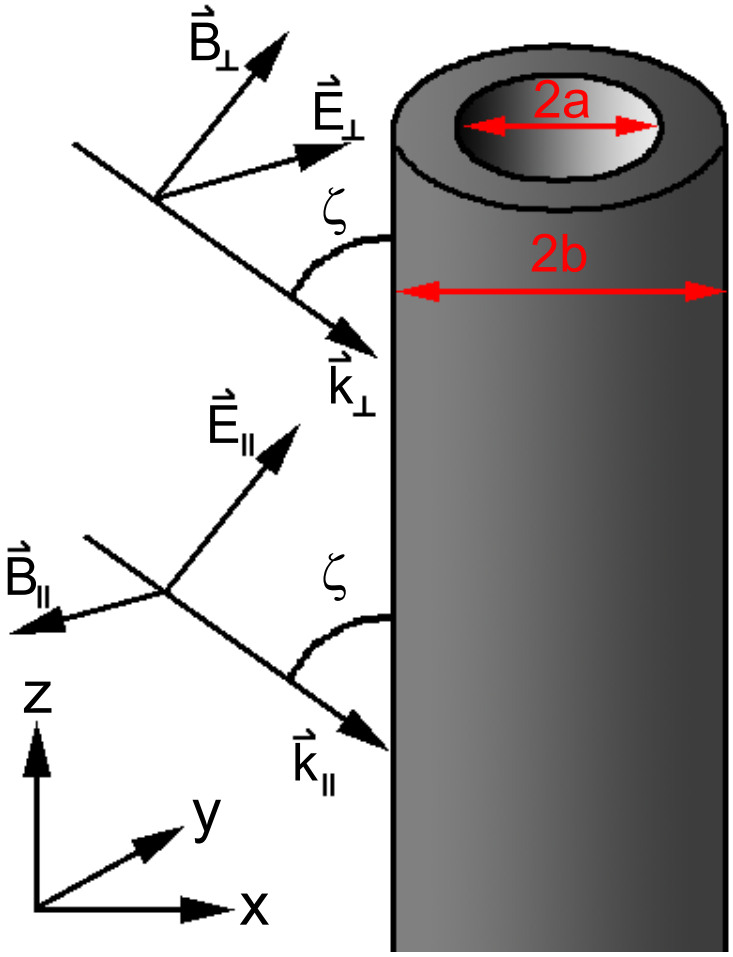

Figure 2.3: Illustration of plane waves incident with angle ζ on a cylindrical tube with inner and outer radii a and b, respectively. Orientations of incident waves with "parallel" polarization ($\vec{E}$ in the x-z plane) and "perpendicular" polarization ($\vec{E}$ in the y-plane) are shown.

Because the fields in the core must remain finite as $r \to 0$, we expand them in terms of the Bessel function of the first kind:

$$\vec{E}^p_{core} = \sum_{n=-\infty}^{\infty} E_n(c_n^p \vec{N}_n^{(1)} + d_n^p \vec{M}_n^{(1)}) \quad \vec{H}^p_{core} = \frac{-i}{Z_0} \sum_{n=-\infty}^{\infty} E_n(c_n^p \vec{M}_n^{(1)} + d_n^p \vec{N}_n^{(1)}). \tag{2.43}$$

Inside the tube itself, there are no restrictions on the behavior of the fields, so they must be a linear combination of Bessel and Hankel functions:

$$\begin{aligned} \vec{E}^p_{int} = \sum_{n=-\infty}^{\infty} E_n[f_n^p(\vec{N}_n^{(1)} - \vec{N}_n^{(3)}) + g_n^p(\vec{M}_n^{(1)} - \vec{M}_n^{(3)}) \\ + p_n^p(\vec{N}_n^{(1)} + \vec{N}_n^{(3)}) + q_n^p(\vec{M}_n^{(1)} + \vec{M}_n^{(3)})] \\ \vec{H}^p_{int} = \frac{-i}{Z} \sum_{n=-\infty}^{\infty} E_n[f_n^p(\vec{M}_n^{(1)} - \vec{M}_n^{(3)}) + g_n^p(\vec{N}_n^{(1)} - \vec{N}_n^{(3)}) \\ + p_n^p(\vec{M}_n^{(1)} + \vec{M}_n^{(3)}) + q_n^p(\vec{N}_n^{(1)} + \vec{N}_n^{(3)})] \end{aligned} \tag{2.44}$$

where Z is the impedance inside the tube.

2.3.3 Hollow Cylinder Absorption Coefficients

With the fields thus defined, we consider the amount of energy from the incident plane wave that is lost to scattering to find the absorption. The total fields outside the tube are $\vec{E} = \vec{E}_i + \vec{E}_s$ and $\vec{H} = \vec{H}_i + \vec{H}_s$, thus the Poynting vector is

$$\vec{S} = \frac{1}{2}\mathrm{Re}\left[\vec{E}_i \times \vec{H}_i^* + \vec{E}_s \times \vec{H}_s^* + \vec{E}_i \times \vec{H}_s^* + \vec{E}_s \times \vec{H}_i^*\right]. \tag{2.45}$$

The first term represents energy stored in the incident wave; the second, in the scattered wave; and the third and fourth terms represent extinction of the incident wave. Thus, we find the cross-sections per unit length by considering the energy flux through a Gaussian cylinder of radius R and length L,

$$\begin{aligned} C_{\text{ext}} &= \frac{RL}{I_i L}\int_0^{2\pi} \vec{S}_{\text{ext}} \cdot \hat{e}_r d\phi = \frac{R}{2I_i}\int_0^{2\pi} \mathrm{Re}\left[\vec{E}_i \times \vec{H}_s^* + \vec{E}_s \times \vec{H}_i^*\right] \cdot \hat{e}_r d\phi, \\ C_{\text{sca}} &= \frac{RL}{I_i L}\int_0^{2\pi} \vec{S}_{\text{sca}} \cdot \hat{e}_r d\phi = \frac{R}{2I_i}\int_0^{2\pi} \mathrm{Re}\left[\vec{E}_s \times \vec{H}_s^*\right] \cdot \hat{e}_r d\phi, \end{aligned} \tag{2.46}$$

where $I_i = |\vec{E}_i|^2/2$. Plugging in the fields from Eqs. 2.41 and 2.42 and performing the integral, the absorption coefficients are found:

$$\begin{aligned}
Q_{\text{ext}}^{||} &= \frac{C_{\text{ext}}^{||}}{2b} = \frac{4}{k(b+a)}\text{Re}\left[b_0^{||} + 2\sum_{n=1}^{\infty} b_n^{||}\right] \\
Q_{\text{sca}}^{||} &= \frac{C_{\text{sca}}^{||}}{2b} = \frac{4}{k(b+a)}\left[|b_0^{||}|^2 + 2\sum_{n=1}^{\infty}\left(|b_n^{||}|^2 + |a_n^{||}|^2\right)\right] \\
Q_{\text{ext}}^{\perp} &= \frac{C_{\text{ext}}^{\perp}}{2b} = -\frac{4}{k(b+a)}\text{Re}\left[a_0^{\perp} + 2\sum_{n=1}^{\infty} a_n^{\perp}\right] \\
Q_{\text{sca}}^{\perp} &= \frac{C_{\text{sca}}^{\perp}}{2b} = \frac{4}{k(b+a)}\left[|a_0^{\perp}|^2 + 2\sum_{n=1}^{\infty}\left(|a_n^{\perp}|^2 + |b_n^{\perp}|^2\right)\right].
\end{aligned} \tag{2.47}$$

In solving for the coefficients a_n^p and b_n^p of the scattered field we calculate the absorption from a CNT.

For a given n, there are 8 independent unknown field coefficients; the boundary conditions that the transverse components of the E and H fields are continuous across the boundary give us a system of 8 equations:

$$\begin{aligned}
(\vec{E}_i^p + \vec{E}_s^p - \vec{E}_{int}^p)|_{r=b} \times \hat{e}_r = 0 \quad (\vec{E}_{core}^p - \vec{E}_{int}^p)|_{r=a} \times \hat{e}_r = 0 \\
(\vec{H}_i^p + \vec{H}_s^p - \vec{H}_{int}^p)|_{r=b} \times \hat{e}_r = 0 \quad (\vec{H}_{core}^p - \vec{H}_{int}^p)|_{r=a} \times \hat{e}_r = 0.
\end{aligned} \tag{2.48}$$

The coefficients a_n^p and b_n^p can be solved analytically; yet the complete solution proves too complex to be reproduced simply. However, we arrive at a tractable expression in the CNT regime of interest by considering the limit of radii $a, b \ll 1$. In terms of $\tilde{\alpha} \equiv ka$ and $\tilde{\beta} = kb$, this condition corresponds to the limits $\tilde{\alpha} \sim \tilde{\beta} \ll 1$ and $|m|\tilde{\alpha} \sim |m|\tilde{\beta} \ll 1$. We then only need to expand the coefficients for $n = 0$ and 1 to find the terms of lowest order in $\tilde{\alpha}$ and $\tilde{\beta}$. The expansions for $J_n(z)$ and $Y_n(z)$ for small z are

$$\begin{aligned}
J_0(z) &\approx 1 - \tfrac{z^2}{4} & J_0'(z) &\approx -\tfrac{z}{2} + \tfrac{z^3}{16} \\
Y_0(z) &\approx \tfrac{2}{\pi}\log\left(\tfrac{z}{2}\right) & Y_0'(z) &\approx \tfrac{2}{\pi z} \\
J_1(z) &\approx \tfrac{z}{2} - \tfrac{z^3}{16} & J_1'(z) &\approx \tfrac{1}{2} - \tfrac{3z^2}{16} \\
Y_1(z) &\approx -\tfrac{2}{\pi z} & Y_1'(z) &\approx \tfrac{2}{\pi z^2}.
\end{aligned} \tag{2.49}$$

From Eq. 2.47, the scattering order will be twice the extinction order, so in the CNT limit $Q_{\text{abs}} \approx Q_{\text{ext}}$. The coefficients of lowest order in $\tilde{\alpha}$ and $\tilde{\beta}$ are $b_0^{||}$, $b_1^{||}$, $a_0^{\perp}$, and $a_1^{\perp}$. These

take on the values

$$\begin{aligned} b_0^{||} &= \tfrac{-i\pi}{4}(\tilde{\beta}^2-\tilde{\alpha}^2)(m^2-1)\sin^2\zeta \quad b_1^{||} = \tfrac{-i\pi}{4}\tfrac{\tilde{\beta}^2(\tilde{\beta}^2-\tilde{\alpha}^2)(m^4-1)}{\tilde{\beta}^2(m^2+1)^2-\tilde{\alpha}^2(m^2-1)^2}\cos^2\zeta \\ a_0^{\perp} &= \tfrac{-i\pi}{32}(\tilde{\beta}^4-\tilde{\alpha}^4)(m^2-1)\sin^2\zeta \qquad a_1^{\perp} = \tfrac{i\pi}{4}\tfrac{\tilde{\beta}^2(\tilde{\beta}^2-\tilde{\alpha}^2)(m^4-1)}{\tilde{\beta}^2(m^2+1)^2-\tilde{\alpha}^2(m^2-1)^2}. \end{aligned} \tag{2.50}$$

Plugging these expansions into Eq. 2.47,

$$\begin{aligned} Q_{\text{abs}}^{||} &= \pi(\tilde{\beta}-\tilde{\alpha})\left[\text{Im}(\epsilon-1)\sin^2\zeta + 2\tilde{\beta}^2\text{Im}\left(\frac{\epsilon^2-1}{\tilde{\beta}^2(\epsilon+1)^2-\tilde{\alpha}^2(\epsilon-1)^2}\right)\cos^2\zeta\right] \\ Q_{\text{abs}}^{\perp} &= 2\pi(\tilde{\beta}-\tilde{\alpha})\tilde{\beta}^2\text{Im}\left(\frac{\epsilon^2-1}{\tilde{\beta}^2(\epsilon+1)^2-\tilde{\alpha}^2(\epsilon-1)^2}\right) \end{aligned} \tag{2.51}$$

where $\epsilon = m^2$ the complex dielectric constant. Several important consequences follow from these expressions. First, the efficiency in both polarizations have dimensionality $Q \sim r/\lambda$, indicating that the cross-sections then have dimensionality $C \sim V/\lambda$; as expected, the thermal radiation is not proportional to the area, but rather the volume. Second, the perpendicular absorption per unit length is independent of incident angle, as expected because the perpendicular polarization vector is also independent of ζ. Finally, the absorption is unpolarized at $\zeta = 0$ where the wave vector lays along the tube axis. In the $a \to 0$ limit, these coefficients become

$$\begin{aligned} Q_{\text{abs}}^{||} &= \pi\tilde{\beta}\left[\text{Im}(\epsilon-1)\sin^2\zeta + 2\text{Im}\left(\frac{\epsilon-1}{\epsilon+1}\right)\cos^2\zeta\right] \\ Q_{\text{abs}}^{\perp} &= 2\pi\tilde{\beta}\text{Im}\left(\frac{\epsilon-1}{\epsilon+1}\right), \end{aligned} \tag{2.52}$$

which is the result for a solid cylinder.[43]

2.3.4 The Infinite Cylinder Approximation

The electrodynamics boundary value problem that must be solved to find Q_{abs} involves solving the wave equation, which has solutions that are analytic for highly symmetric geometries; as such, we approximate our nanotubes as infinitely long cylinders. Typical MWCNT lengths range from $1-4$ μm, so $L \gg \lambda$ near the blue end of the visible, and this infinite length approximation is valid. However, in the NIR, $L \sim \lambda$ for shorter nanotubes, and thus we must consider what errors are introduced by the tube's finite length.

A finite cylinder is approximated as a prolate ellipsoid, the surface

$$\frac{x^2}{c'^2}+\frac{y^2}{b'^2}+\frac{z^2}{a'^2}=1 \tag{2.53}$$

with semiaxes $a' = L/2 > b' = c' = r$. The coefficients for an incident wave normal to a semiaxis scattering off an ellipsoid with $b \ll \lambda$ are given as

$$Q_{abs}^{z} = \frac{\pi x}{3} \mathrm{Im}\left[\frac{\epsilon - 1}{1 + L_z(\epsilon - 1)}\right] \tag{2.54}$$

with the shape factor defined by

$$L_z = \frac{a'b'c'}{2}\int_0^\infty \frac{dq}{(z^2+q)\sqrt{(a'^2+q)(b'^2+q)(c'^2+q)}}, \tag{2.55}$$

where z is any one of a',b', or c'.[46] These shape factors satisfy the condition $L_{a'} + L_{b'} + L_{c'} = 1$.

These shape factors determine at what ratio a'/b' a prolate ellipsoid approximates an infinite cylinder by comparing to the typical infinite cylinder result. It is seen that Eq. 2.54 becomes the solid cylinder result Eq. 2.52 as $L_{a'} = 0$ and $L_{b'} = L_{c'} = 1/2$, up to the geometric factor $\frac{\pi}{3} \sim 1$. The ellipsoid shape factors $L_{a'} \approx .01$ and $L_{b'} = L_{c'} \approx .495$ when $a' = 15b'$. As the radii of MWCNTs are around 10 nm, any nanotube of length $\gtrsim 300$ nm may be treated as an infinite cylinder, provided its physical length is the appropriate length to consider for scattering.

One alternative concept of length is the amount of the filament that actually contributes to radiation. For a macroscopic filament, with a constant temperature profile, this "hot length" is identical to the physical length. The amount of light the middle sL of the nanotube will generate as compared to the whole length is the ratio of factors from Eq. 2.29,

$$I(k) = \frac{\int_{-sL/2}^{sL/2} \exp\left[\frac{-C_2(T_{\max}-T_0)}{\lambda T_{\max}^2}\left(\frac{2l}{L}\right)^2\right] dl}{\int_{-L/2}^{L/2} \exp\left[\frac{-C_2(T_{\max}-T_0)}{\lambda T_{\max}^2}\left(\frac{2l}{L}\right)^2\right] dl} = \frac{\mathrm{erf}\left(s\sqrt{C_2(T_{\max}-T_0)/\lambda T_{\max}^2}\right)}{\mathrm{erf}\left(\sqrt{C_2(T_{\max}-T_0)/\lambda T_{\max}^2}\right)}. \tag{2.56}$$

We conservatively define the hot length as $L_T(\lambda) = sL$ such that $I(s) = .99$. As the error function increases monotonically with argument, and the argument decreases with increasing wavelength and temperature, the value of s at which 99% of the light is radiated increases with λ and $T_{\max}$. Therefore, a reasonable lower bound on a MWCNT's hot length is $L_{1000\ \mathrm{K}}(450\ \mathrm{nm}) \approx .38L$. Fixing $b = 10$ nm, for any $L \gtrsim 790$ nm, L_T is still large enough to approximate the filament as an infinite cylinder, with the approximation only becoming better the longer the tube.

2.3.5 The Graphene Approximation for MWCNT Absorption

To evaluate the Eqs 2.51 for a given tube material, we require the dielectric constant ϵ. In general, for a complex conductivity σ,

$$\epsilon = 1 + i\frac{4\pi\sigma}{\omega} = 1 + i\frac{\sigma Z_0}{k}, \tag{2.57}$$

and knowledge of the 3-D conductivity as a function of wavelength determines Q_{abs}. However, as a MWCNT is comprised of multiple concentric SWCNTs, which have a 2-dimensional surface, it is more appropriate to consider a 2-dimensional surface conductivity related to the 3-D conductivity by $\sigma_{2\text{D}} = \sigma/(b-a)$.

Assuming a purely real, 2-D conductivity, Eqs. 2.51 simplify to

$$\begin{aligned} Q^{||}_{\text{abs}}(\zeta) &= \pi\sigma_{2\text{D}}Z_0\left[\sin^2\zeta\right. \\ &\qquad \left. +4\beta^2\frac{(\sigma_{2\text{D}}Z_0)^2(\beta^2+\alpha^2)+4\beta^2(\beta-\alpha)^2}{(\sigma_{2\text{D}}Z_0)^4(\beta+\alpha)^2+8(\sigma_{2\text{D}}Z_0)^2\beta^2(\beta^2+\alpha^2)+16\beta^4(\beta-\alpha)^2}\cos^2\zeta\right] \\ Q^{\perp}_{\text{abs}}(\zeta) &= 4\pi\sigma_{2\text{D}}Z_0\beta^2\frac{(\sigma_{2\text{D}}Z_0)^2(\beta^2+\alpha^2)+4\beta^2(\beta-\alpha)^2}{(\sigma_{2\text{D}}Z_0)^4(\beta+\alpha)^2+8(\sigma_{2\text{D}}Z_0)^2\beta^2(\beta^2+\alpha^2)+16\beta^4(\beta-\alpha)^2}. \end{aligned} \tag{2.58}$$

In the limit of $t \to 0$ and $\alpha, \beta \to x = kr$, Eqs. 2.58 further reduce to

$$\begin{aligned} Q^{||}_{\text{abs}} &= \pi\sigma_{2\text{D}}Z_0\left[\sin^2\zeta + \frac{2x^2\cos^2\zeta}{(\sigma_{2\text{D}}Z_0)^2+4x^2}\right] \\ Q^{\perp}_{\text{abs}} &= \pi\sigma_{2\text{D}}Z_0\frac{2x^2}{(\sigma_{2\text{D}}Z_0)^2+4x^2}. \end{aligned} \tag{2.59}$$

Thermal spectra have been observed for incandescent SWCNTs[47], exhibiting strong peaks for small radii tubes in the parallel polarization due to intraband absorption and in the perpendicular polarization due to interband absorption. Our model for MWCNTs, using an isotropic two-dimensional conductivity $\sigma_{2\text{D}}$, in the zero-thickness limit, cannot account for such peaks. However, because of the efficiencies' linear dependence on conductivity, substitution of the appropriate conductivity models $\sigma^{||}$ and $\sigma^{\perp}$ from SWCNT theory will similarly result in transition peaks.

For MWCNT absorption, because the electronic bands for each tube are similar to graphene, we equally expect the 2-D conductivity to be similar to that of n-layer graphene. Tree-level electron-phonon interactions predict a temperature dependent conductivity for

undoped graphene

$$\sigma_g(T) = \frac{\alpha c}{4} \tanh\left(\frac{\hbar c k}{4 k_B T}\right) = \frac{\pi\alpha}{Z_0} \tanh\left(\frac{C_2}{4\lambda T}\right), \tag{2.60}$$

where $\alpha = 1/137$ is the fine-structure constant[33, 34]. At low temperatures and short wavelengths, the tanh factor becomes 1, and $\sigma_g \to \pi\alpha/Z_0$, corresponding to transmission of $T = 1 - \pi\alpha \approx .977$, which has been confirmed experimentally[22]. At $T \gtrsim 2000$ K, $\sigma_g(T)$ begins deviating from $\pi\alpha/Z_0$ for longer wavelengths. We estimate this effect at $T = 2200$ K, $\lambda = 1100$ nm by

$$\frac{\sigma_g(T_{\max}) \int_{-L/2}^{L/2} e^{-C_2/\lambda T(l)} dl}{\int_{-L/2}^{L/2} \sigma_g(T(l)) e^{-C_2/\lambda T(l)} dl} \approx .955, \tag{2.61}$$

so we introduce an error of $\lesssim 4.5\%$ by taking the conductivity constant based on the maximum temperature, which we do to retain an analytic form for $\dot{N}$. Thus substituting Eqs. 2.58 with $\sigma_{2D} = \sigma_g(T_{\max})$ into Eq. 2.30 provides a complete theoretical picture for thermal radiation of a MWCNT filament.

CHAPTER 3

Nanolamp Construction and Operation

3.1 Device Fabrication

3.1.1 Introduction

To study the thermal radiation of MWCNTS, we fabricate nanolamp devices on silicon microchips. The filaments are constructed by electrically connecting to a MWCNT with electron-beam lithography-defined contacts. The MWCNTs are suspended atop a membrane window, which is thinned to electron transparency such that characterization in a TEM can be performed. Contact pads allow us to connect the microchips to a power source and apply a bias, heating the filaments. The architecture of these devices is illustrated in Fig. 3.1. The fabrication process is modified from a process developed by Dr. Yuwei Fan.

3.1.2 Definition of Membrane Windows

The membrane on which the nanofilament rests consists of an oxide layer that prevents device shorting to the silicon wafer and a nitride layer acts as an etch stop during the wet processing of the window. We begin with a 100 mm diameter, 200 μm thick p-doped bare Si wafer with a pregrown SiO_2 layer of either 80 or 800 nm, polished on both sides. We find that a larger thickness improves processing at later steps, so for wafers with the pregrown 80 nm oxide, an additional wet thermal oxide growth is performed in a low pressure continuous vapor deposition (LPCVD) furnace at 1100° C by flowing H_2 and O_2 gas until the thickness is $\sim$ 800 nm. An additional growth of 10-20 nm Si_3N_4 is performed in another LPCVD furnace with a flow of ammonia (NH_3) and dichlorosilane (H_2SiCl_2). The thickness of both dielectric films are measured using a normal incidence reflectometer.

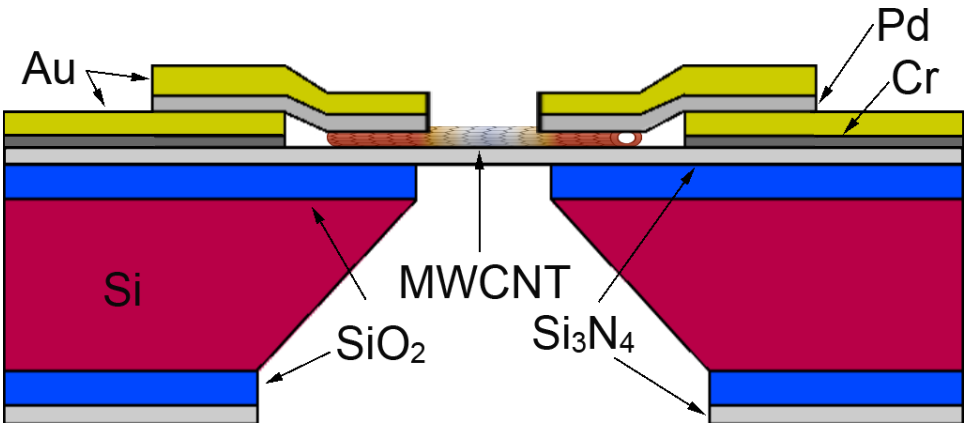

Figure 3.1: Illustration of the nanofilament device architechture. Not to scale.

To release the windows and define the cleavage planes on our wafer, we perform an etch with potassium hydroxide (KOH). KOH is an anisotropic wet etch with etch selectivities in the planes (100):(110):(111) of 100:100:1.[48] The angle between the (111) and (100) planes is $\theta_{\mathrm{KOH}} = \arctan\sqrt{2}$. Therefore, for a wafer of a thickness t and an exposed Si length of distance x_0 along the (100) plane, the corresponding dimension of the final hole on the other side of the wafer is $x_e = x_0 - 2t/\tan\theta_{\mathrm{KOH}} = x_0 - 2t/\sqrt{2}$, as shown in Fig. 3.2. Using this formula and a desired value for x_e, we define the rectangles in the optical lithography to have the required x_0 values.

In fact, the KOH etch seeks out the (111) planes, so defining an etch geometry more complex than a rectangle will not have the desired results. In general, for a non-convex pattern, the relevant x_0 values are those of the pattern's bounding rectangle. This correction applies to misalignment, as well. Because this lithography step has no predefined alignment marks, the wafer flat is aligned with the lithography mask axis only through visual alignment to the mask aligner's wafer chuck. Such alignment allows an error of $\sim 1.5°$ in how parallel the rectangles are to the true (100) crystal plane. Defining the rectangle lengths as x_0 and y_0 and the tilt as ϕ, the exposed windows in our wafers have sides of length $x'_e = (x_0\cos\phi + y_0\sin\phi) - 2t/\sqrt{2}$ and $y'_e = (-x_0\sin\phi + y_0\cos\phi) - 2t/\sqrt{2}$.

Using optical lithography, the starting rectangles for both the membranes and wafer cleavage lines are exposed in a 1.4 μm thick AZ5214 photoresist layer; development in a solution of 1:6 AZ300K:H_2O positive photoresist developer exposes these rectangles. The

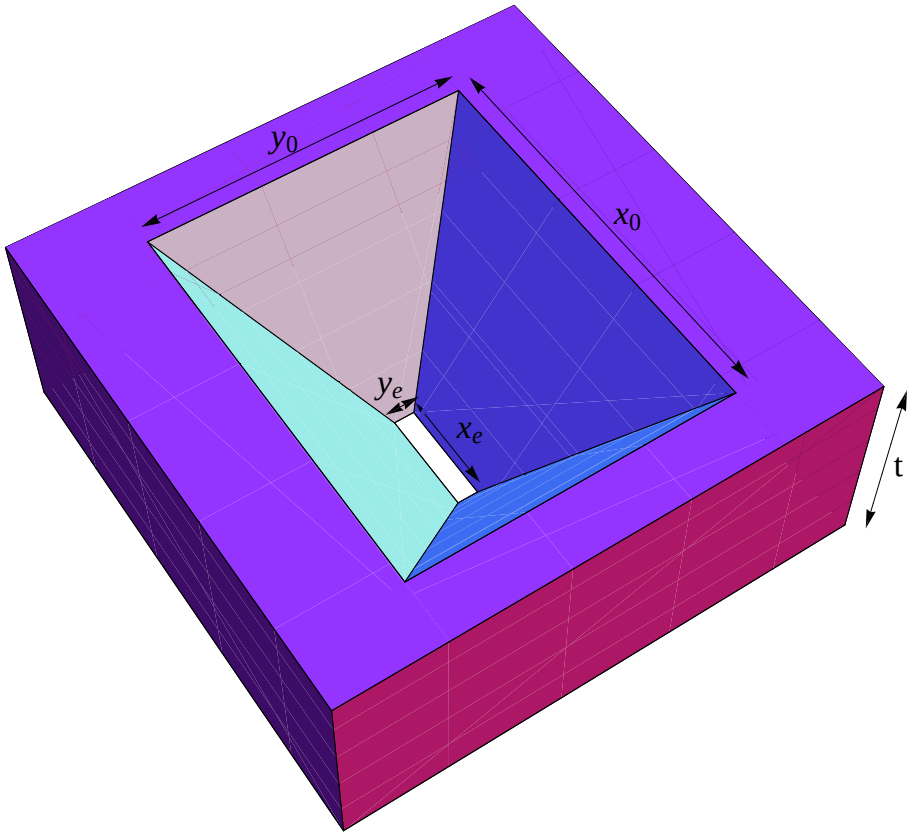

Figure 3.2: Illustration of the $x_e \times y_e$ membrane defined by KOH etching an initial area of $x_0 \times y_0$ on a silicon wafer of thickness t.

remaining photoresist serves as a hard etch mask for the dry etch step, where a CF_4/O_2 plasma removes the Si_3N_4 and SiO_2 above the Si where the KOH etch is performed. The photoresist is removed in a bath of Aleg 355 positive photoresist remover, leaving bare silicon in the desired rectangles and Si_3N_4 covering the rest of the wafer.

The wafer is designed for two different geometries of windows–a 300×10 μm rectangle and a 20×20 μm square. The errors in alignment can produce windows as different as 292×25 μm for the rectangles and 28×12 μm for the squares. We typically do not see such extreme differences in the designed geometry, but even at this limit, the windows will still function as desired. Smaller rectangles define the borders of thirty-two 12.6×12.6 mm^2 squares and sixteen 2.1×2.1 mm^2 chips within each square; the border dimensions are defined such that the etch stops before penetrating through the 200 μm wafer (equivalently, $x_e < 0$).

Once the SiO_2/Si_3N_4 windows have been exposed, delicate care is required as not to rupture the membranes. Sonication even at the lowest power available in an ultrasonic tank will destroy the windows, as will the pressure from an N_2 gun aimed normal to the wafer. For membrane thicknesses < 300 nm, the surface tension caused by water evaporation will also cause membranes to rupture, so all wet processes henceforth are aided by immersion in isopropanol or methanol prior to evaporative drying.

3.1.3 Optical Lithography of Contacts

A second optical lithography step patterns contacts, alignment marks, and chip identifier labels on the front of the wafer via backside alignment to marks formed by the KOH. Electron-beam evaporation deposits 12 nm Cr and 120 nm Au on the wafer. An acetone liftoff removes the photoresist and deposited metal films where the resist was not exposed, leaving only the desired electrode pattern. Each chip has four electrodes bordering the windows, which are connected to macroscopic contact pads of size 500×250 μm at the top of the chip, as visible in Fig. 3.3, allowing a maximum of three independent devices per chip.

Alignment marks consisting of 10 μm $\times$ 10 μm squares are patterned on every wafer square and every chip for electron-beam lithography alignment. Global alignment marks are

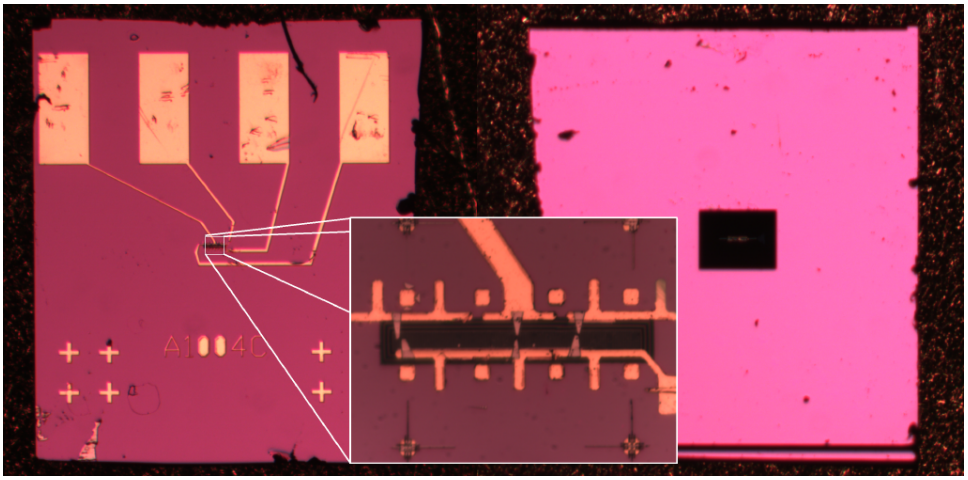

Figure 3.3: Optical images of the front and back of the chip. The backside shows the initial etch geometry for the KOH. The inset shows a zoom-in on the membrane revealed by the KOH etch.

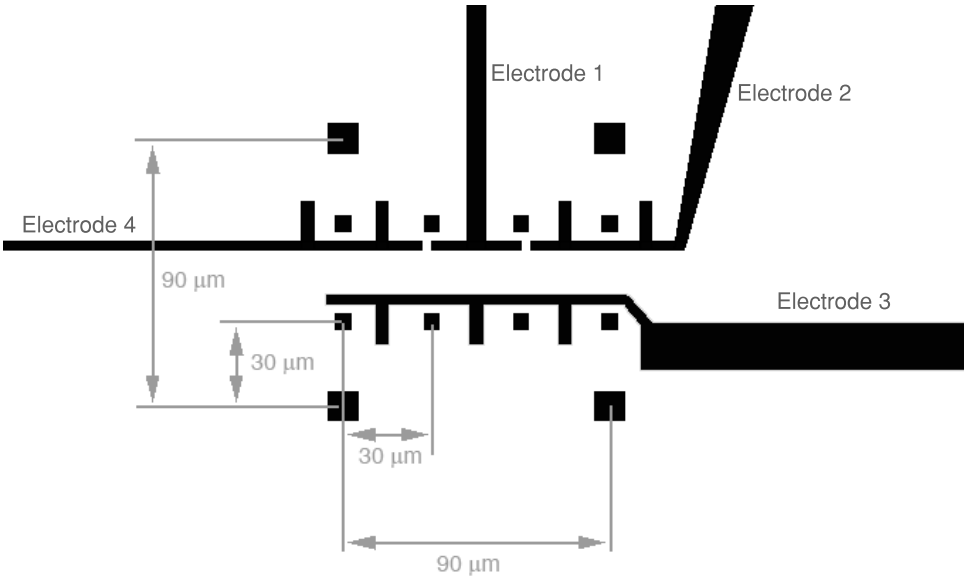

Figure 3.4: Electrode design surrounding the membrane window. Electrode 3 functions as the common ground, and a nanotube filament connects to electrode 3 and one of electrodes 1, 2, or 4. Alignment marks on a 30 μm pitch are used in mapping the desired filaments, and marks on 90 μm square are used for e-beam writer alignment.

placed on a 9.4 mm pitch centered on the wafer square, and local alignment marks are placed on a 90 μm pitch centered on the chip membrane. Additional alignment marks are placed on a 30 μm pitch grid around the membrane for nanotube mapping. Figure 3.4 shows the electrode configuration around the membrane, along with these alignment marks. Each chip is also labeled with a unique identifier. Following the optical lithography of the macroscopic contacts, the wafer is cleaved into wafer squares using a diamond scribe.

3.1.4 Contacting MWCNT Filaments

Nanotube dispersion is performed on each wafer square individually. The nanotubes which comprise the nanofilaments are purchased from the MER corporation in bulk and separated for dispersion onto microchips. The preferred recipe for nanotube dispersion is a solution of 2-3 mg of arc-discharge nanotubes in 1 mL of isopropanol. This solution is sonicated and centrifuged to suspend individual MWCNTs in solution, with all amorphous carbon residue segregated to the centrifuged pellet. We spin coat .5 mL of this solution onto a wafer square and let it air dry.

MWCNTs to be contacted are selected for cleanliness, long length, and relative isolation from other CNTs and detritus on the membrane. Mapping of the nanotubes is performed using an FEI Nova 600 Dual-beam Focused Ion Beam (FIB) as a scanning electron microscope (SEM). Images are taken at 5000x magnification where the membrane and previously mentioned alignment marks are visible in the same image. Using beam settings of 2 kV and .54 pA, the MWCNTs are visible on the membrane, and higher magnification pictures are taken as necessary to check that the above selection criteria are met.

Electron-beam lithography can achieve a resolution and accuracy of 10 nm, in contrast to 3 μm resolution provided by optical lithography, and is therefore required for defining electrical contacts to the nanotubes themselves. We have written Labview software which loads the SEM images, allows us to draw the desired contacts on the chip, and converts the pattern to a file compatible with a Vistec EBPG 5000+ES e-beam lithography system. We expose these patterns on a layer of PMMA 495 A4 e-beam resist using a beam current of 100 keV and dose of 1400 μC/cm^2. Pd has the lowest work function to nanotubes;[49]

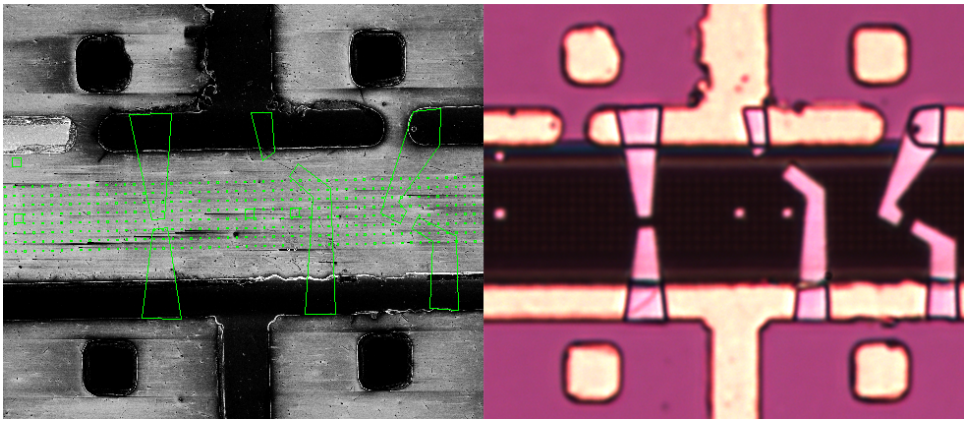

Figure 3.5: (a) SEM image of a chip membrane, with nanotubes as well as alignment marks visible. The green overlays represent proposed e-beam contacts. (b) Optical image of the same chip following e-beam lithography.

as such, we evaporate 50 nm Pd and 80 nm Au to create nanotube contacts with low contact resistance following acetone liftoff. Fig. 3.5 shows the SEM image, Labview-defined contact patterns, and resultant contacts after lithography. Successful e-beam contacting of a MWCNT results in an operational nanolamp device.

3.2 Nanotube Characterization

3.2.1 Electrical Probing of Devices

Following the e-beam lithography, we determine which nanotubes have been successfully contacted and fall within acceptable experimental criteria. The wafer squares are annealed at 300°C for a 20 min to improve device resistance. The squares are then cleaved into their respective chips, and we measure the low-bias I-V response (peak of 1 mV) on each device in a probe station. Typical filament resistances range between 10 and 30 kΩ, ideal for operation with applied voltage of 2-4 V, yet even a filament with resistance as high as 100 kΩ will acheive incandescence for biases $\lesssim$ 7 V.

The nanolamps reach incandescence in the visible with a large enough signal to saturate the CCD in $\sim$ 1 s at applied power $P \gtrsim 100$ μW. Figure 3.6 shows the I-V response of a

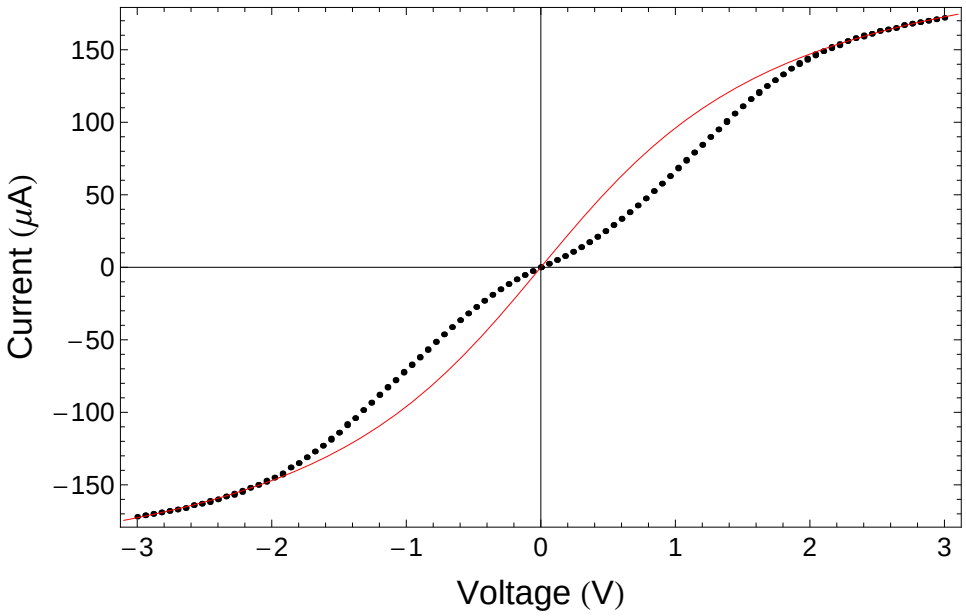

Figure 3.6: $I(V)$ up to operating voltages for a nanolamp device. The fit to an arctangent has been performed using the data points with $|V| > 2$ V. The maximum current measured is 172 μA, and the saturation current is found to be 235 μA.

representative nanolamp device with voltage up to operational bias. The I-V shows three distinct regions–low bias, intermediate bias, and high bias. At $V \lesssim .1$ V, the devices exhibit ohmic behavior. At intermediate voltages, the contacts are responsible for the majority of dissipation, and $I(V)$ roughly fits a sinh function representative of the Schottky barriers between the CNT and the contacts[50, 49]. Finally, at operational voltages, the majority of the power is lost through the nanotube, and the $I(V)$ fits an arctangent function as predicted by Eq. 2.18. The solid curve in Fig. 3.6 represents a fit of this arctangent to points with $|V| > 2$ V, well covering the range over which this device radiates significantly in the visible-NIR.

3.2.2 TEM Characterization of MWCNT Geometry

As complete knowledge of the CNT geometry is necessary for predicting the absorption, the windows are made electron transparent, such that the nanotubes can be characterized in a transmission electron microscope (TEM). We etch the membranes on the chips with active devices until they are thin enough for electron transparency. Chips are suspended about ~ 2 cm above 49% hydrofluoric acid (HF) for one minute, followed by suspension ~ 5 mm above methanol. The etch rate is ~ 120 nm SiO_2/min. The HF vapor above the solution reacts with the SiO_2 membrane to produce H_2O and SiF_4 vapors, and the methanol vapors prevents the condensation of the H_2O on the membrane, subsequent evaporation of which tends to rupture the membranes. HF etches Si_3N_4 as well, but an order of magnitude more slowly, so this etch results in MWCNT devices supported on very thin nitride membranes (< 10 nm) if not completely suspended. Once the membranes have been etched, the chips are baked and probed once more.

We measure the nanotube's geometry in a FEI Low-base Titan TEM, where high magnification images of the individual MWCNTs are taken. At TEM magnifications, we can determine whether a device consists of a single, relatively clean and defect free tube versus a double tube or bundle. Figure 3.7 shows an ideal device which is very straight and free of defects. The TEM is able to produce images with wall resolution, such as in Fig. 3.8, allowing full characterization of the inner and outer radii, length, and number of walls. Characterized nanotube devices are now ready to be loaded into the setup and biased for data collection.

3.2.3 *In situ* TEM Biasing

We have observed that in operation the current drawn by the nanolamps at constant bias does not stabilize immediately. To understand what physical changes occur in the system that alter the resistance of the filament, we observe the nanotube in the TEM while biased by loading the device in a custom Hummingbird biasing stage. Video capture by the TEM's CCD is performed in conjunction with observing the current through the nanotube.

We observe two distinct responses of the nanotube–at lower biases the current increases before stabilizing, and at higher biases the current decreases before stabilizing. Increases

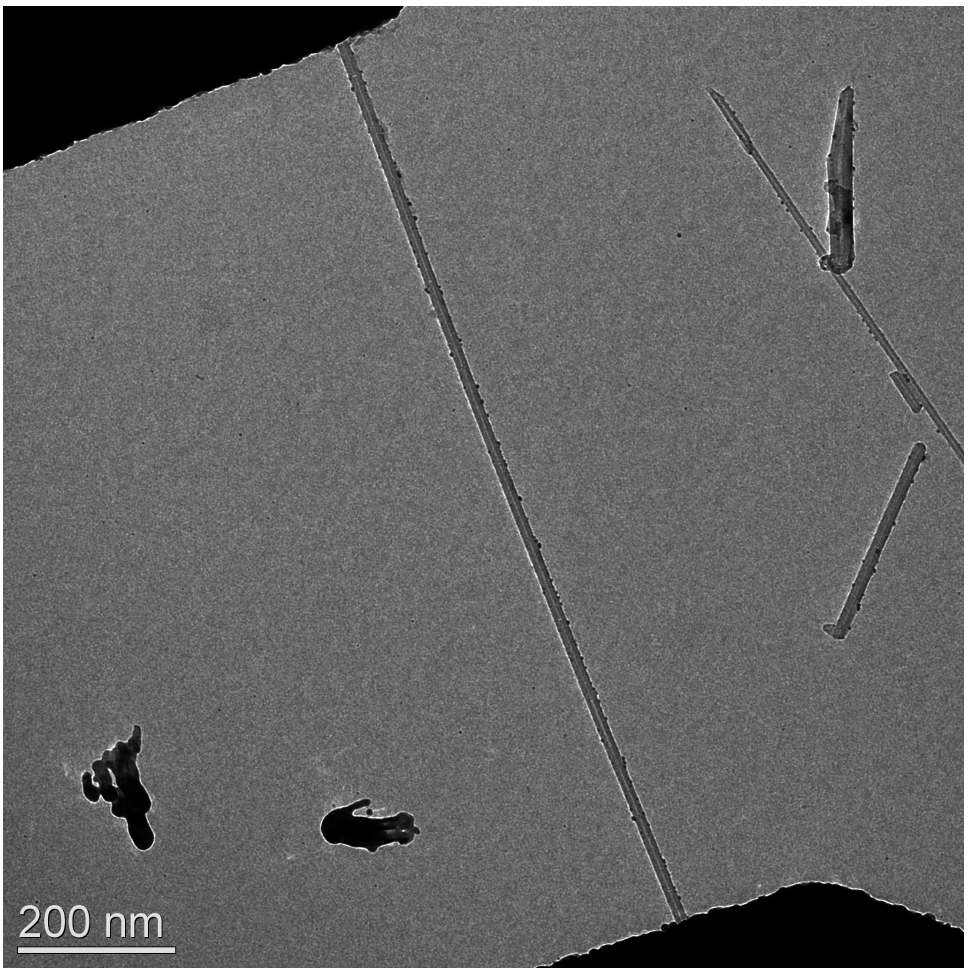

Figure 3.7: TEM image of ideal MWCNT filament. The nanotube is extremely straight and defect free. Image courtesy of Matthew Mecklenburg.

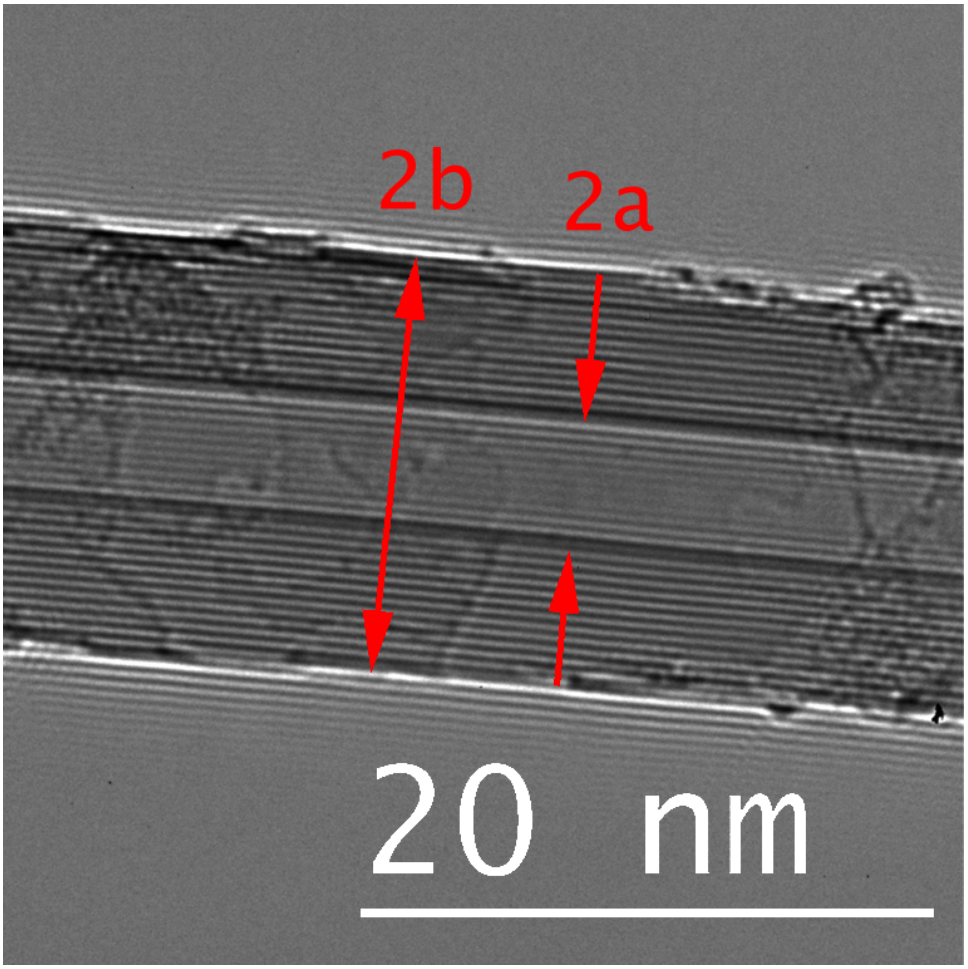

Figure 3.8: High magnification image of a MWCNT, showing resolution of walls and measurement of inner and outer radii. Image courtesy of Matthew Mecklenburg.

of the current correspond to the nanotube's self-cleaning; gold nanoparticles deposited on the MWCNT surface evaporate, and the number of bamboo defects in the core of the tube decreases. Decreases in the current, however, correspond with a more interesting physical effect. At large enough biases, the temperature of the filament becomes high enough to evaporate the surrounding membrane.

Over a period of several minutes, the membrane near the center of the tube dissociates as the current lowers. Figure 3.9 shows a series of screen captures from video taken of this effect in conjunction with $I(t)$ data. As the membrane is an insulator, we interpret this increase in resistance as resulting from an increase of the nanotube temperature. Because heat is no longer being lost to membrane, the filament has a smaller effective κ and thus reaches a higher maximum temperature. This higher temperatures increases the range of the isotherm at the membrane's evaporation temperature, and this process continues, asymptotically reaching an equilibrium state where the current stabilizes. This stabilization occurs near the saturation current, and we make note of this voltage as the maximum operational voltage, as exceeding it tends to result in failure of the device.

3.3 Vacuum System

3.3.1 Vacuum System

Once the devices have been characterized, they are loaded in a vacuum chamber for nanolamp operation. Vacuum is critical to nanotube lifetime, as they have been shown to breakdown in air at lower biases due to reacting with oxygen or water vapor.[39] In order to reach high temperatures without device failure, we minimize the amount of possible reactants. The complete vacuum system is shown in Fig. 3.10 with all additional components utilized for operation. We pump down in two stages via a turbopump and an ion pump. A residual gas analyzer (RGA) allows us to leak test the system, and gas cylinders can be connected via intake plumbing for experiments using different background gases.

A vacuum sufficiently high to prevent nanotube breakdown owing to oxidation is realized in a spherical octagon chamber from Kimball Physics. This chamber utilizes Conflat fittings

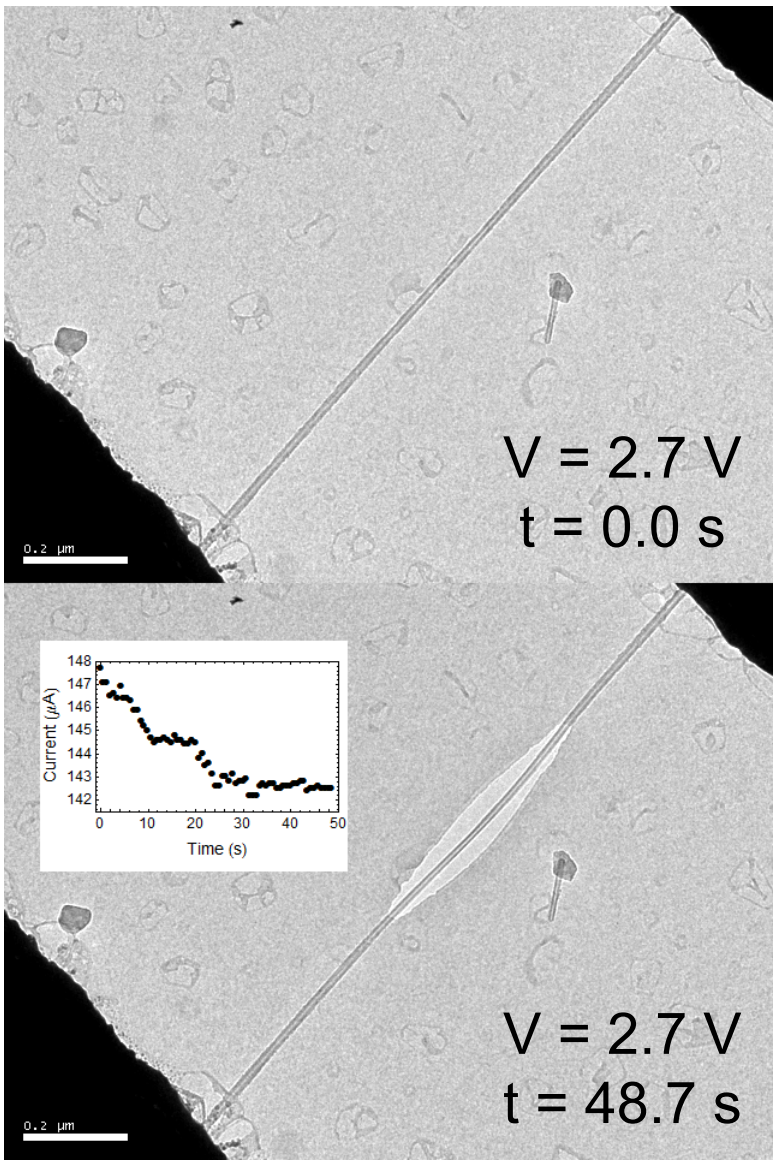

Figure 3.9: Images nanotube device A1403J and surrounding membrane before and after membrane evaporation under a constant bias of 2.7 V. The inset shows the current through the nanotube decreasing with time as the membrane disintegrates, stabilizing after $\sim$ 30 seconds. Image courtesy of Edward White.

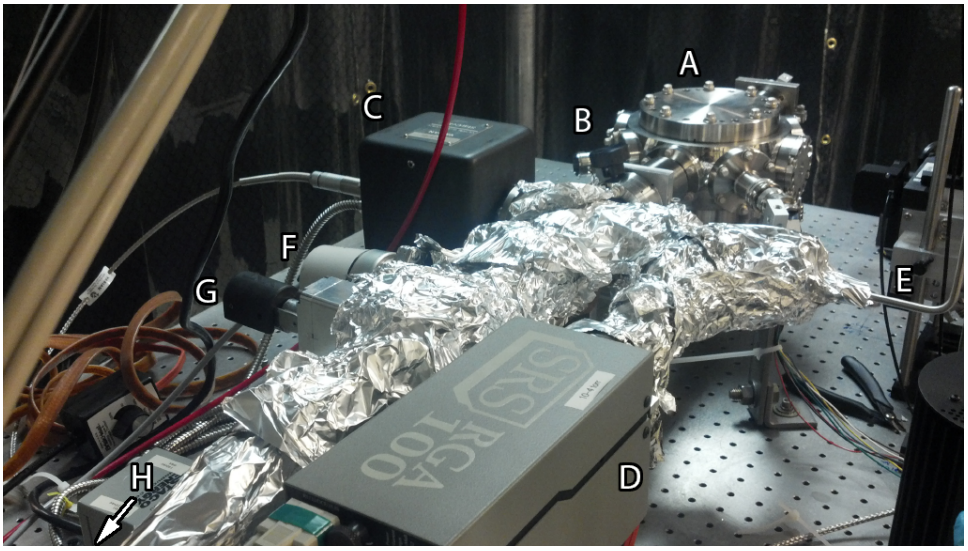

Figure 3.10: The vacuum system, comprised of vacuum chamber (A), butterfly valve (B), ion pump (C), residual gas analyzer (D), gas intake (E), roughing gauge (F), gate valve (G), and turbo pump (H, not shown).

and copper gaskets to reach ultrahigh vacuum (UHV). This vacuum system is capable of reaching pressures of $\sim 10^{-8}$ mbar, and we observe nanolamp lifetimes > 100 hours in operation. The octagonal chamber fixes the chip's position exactly and is orthogonal to the optical axis within machining tolerances.

3.3.2 Nanotube Connection and Positioning

To adjust the chip position, the vacuum chamber is clamped to a z-stage on top of an x-y stage, both capable of precise positioning on the order of ~ 10 μm using micrometers (see Fig. 3.11). The microscope optical axis is defined to be along in the y-direction; thus, adjusting the y position on the x-y stage provides the coarse focus for the microscope. The x position on the x-y stage and the z-stage control centering the chip with respect to the microscope.

An aluminum holder houses the chip, and electrical contact is made via a custom-built Delrin connector, as seen in Fig. 3.12. The contact wires simultaneously make contact to the large Au pads on the chip and secure the chip by friction. The wires pass through a

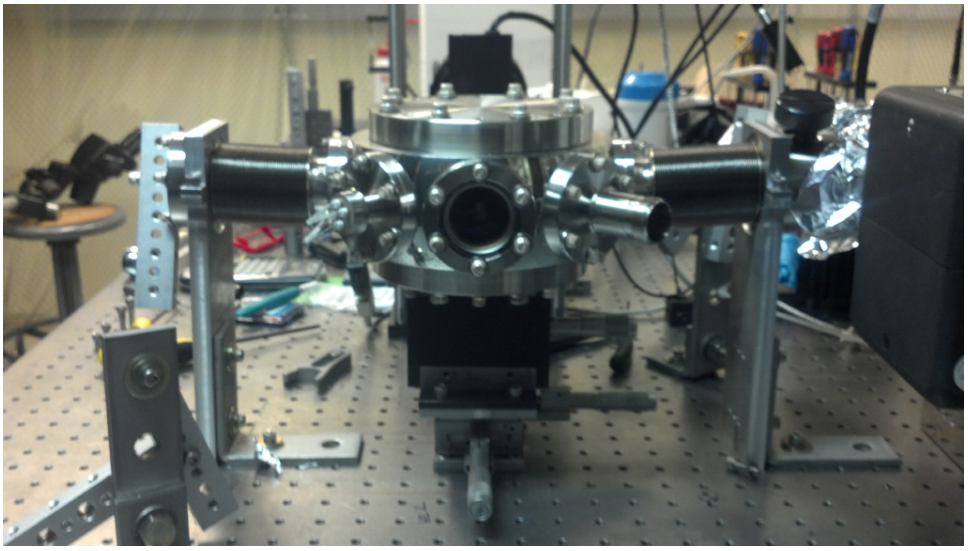

Figure 3.11: The vacuum chamber sitting on $x-y$ and z-stages is connected to the rest of the vacuum system by a flexible bellows to allow positioning and coarse focusing.

feedthrough to the outside of the vacuum system for electrical connection. A small lightbulb is placed in the backside of the aluminum holder for backlighting the chip, which sits atop a .052" hole. This backlighting allows us to focus on the chip's membrane. This holder places the chip < 2 mm from a 1.1 mm thick borosilicate crown glass (BK-7) window in the chamber, shown in Fig. 3.12.

3.3.3 UHV Pumpdown

Pumpdown is performed in two stages with the turbo and an ion pumps, transitioning between the two once the roughing gauge reads $\lesssim 10^{-5}$ mbar. Once the ion gauge reaches $\lesssim 10^{-6}$ mbar, an overnight bake at 90°C is performed to purge H_2O vapor that has adsorbed into the steel of the chamber. We wrap the system in heating tape and bring the temperature to ~ 90°C and pump out the H_2O vapor overnight. Although we flood the system with He_2 or N_2 gas when it is not in use to prevent buildup of water vapor, the chamber is open to air during loading and unloading of devices, and without the bake the ion gauge's lowest reading is $\sim 10^{-7}$ mbar. This process achieves a pressure of $\sim 10^{-8}$ mbar. Finally, before operation, we close the gate valve and turn off the turbopump, as its vibrations are detrimental to

Figure 3.12: The nanolamp microchip contacted and mounted within the vacuum chamber, as seen through the BK-7 window.

imaging.

3.4 Electronics

3.4.1 Nanolamp Circuit

The main cause of device failure is electrostatic discharge (ESD), as a voltage of only a few volts will draw enough current through the MWCNT to destroy it, so care must be taken in how we connect to the nanolamp. The electric connector which contacts the four gold pads on the chip lead outside the vacuum chamber by an electric feedthrough. Outside the vacuum, these leads connect to a breakout box. A DP6T switch selects which 2 contacts will be biased.

Protective resistors and switches allow us to connect to the power supply without destroying the filament. Figure 3.13 shows the complete nanolamp circuit. A single pole single throw (SPST) switch creates a short that bypasses the device completely, allowing a make-then-break connection and drawing the majority of current from any magnetic pickup from the vacuum pumps and components. A four pole single throw (4PST) switch creates a short that bypasses 500 kΩ resistors that are in series with every contact. This switch is open when connecting the device to the connector, connecting the device to the power supply, or switching between devices; the resistors will limit the current drawn by any voltage that had accumulated across leads. During operation, the SPST switch is open while the 4PST switch is closed.

3.4.2 Operation of Nanolamp

The MWCNT is brought to incandescence by sourcing a voltage from a Keithley 2602 power supply. The Keithley is capable of sourcing up to 40 V and measuring current with nA precision every .001 plc (power line cycle) $\approx$ 16.7 μs. We set a current limit such that the device cannot draw enough current to destroy itself via electronic pick-up. At operational voltages, the fluctuations in current are of order $\lesssim 0.1\%$. We program the Keithley to send a trigger pulse to the camera, wait 20 ms for the shutter to open, and operate the nanolamp

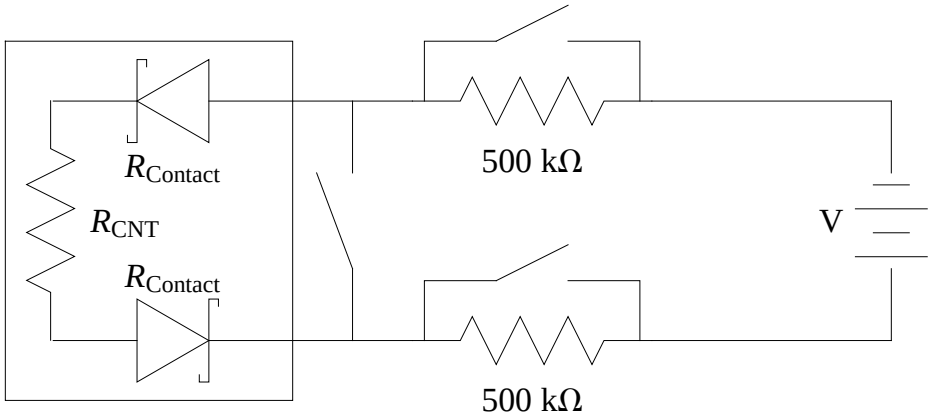

Figure 3.13: Circuit of nanolamp with expanded nanofilament. The MWCNT is a resistive element, while the metal-CNT contacts form Schottky barriers.

for a specified number of plc at a certain voltage, timed with the camera exposure, to record the radiation of the incandescent nanofilament.

CHAPTER 4

Optically Imaging a Nanofilament

4.1 Imaging the CNT

4.1.1 Introduction

To measure the light radiated from the nanotube filament, we have built an optical microscope capable of high-magnification, sub-λ resolution imaging and single photon detection. Taking an image of the incandescent nanotube filament provides a number of advantages over simply collecting the total intensity represented by Eq. 2.30. An optical image allow us to directly confirm from location and orientation that the radiation originates from the nanotube, as opposed the contacts, membrane, or nearby contaminants. Furthermore, the size of the camera's CCD combined with additional optics allows simultaneous measurement of polarization and spectrum dependence of the intensity. The discreteness of the CCD also gives many independent measurements of temperature and coherence within a single exposure. However, the limitations of optical microscopy necessitate modifications to Eq. 2.30.

4.1.2 Objective Orientation

To determine how much light is captured by our microscope objective, we must translate the coordinate system of the MWCNT Mie model into that of the microscope. The coefficients Q_{abs} of Eq. 2.58 are calculated in the coordinate system of the nanotube, where η is the angle between incidence and the nanotube axis and ϕ is the angle about the nanotube axis. The relationship between CNT coordinates and objective coordinates is illustrated in Fig. 4.1, and the required transformation is $\eta \to \pi/2 - \theta$ and $\phi \to \theta'$, where θ' is the rotation of θ by $\pi/2$ about the optic axis.

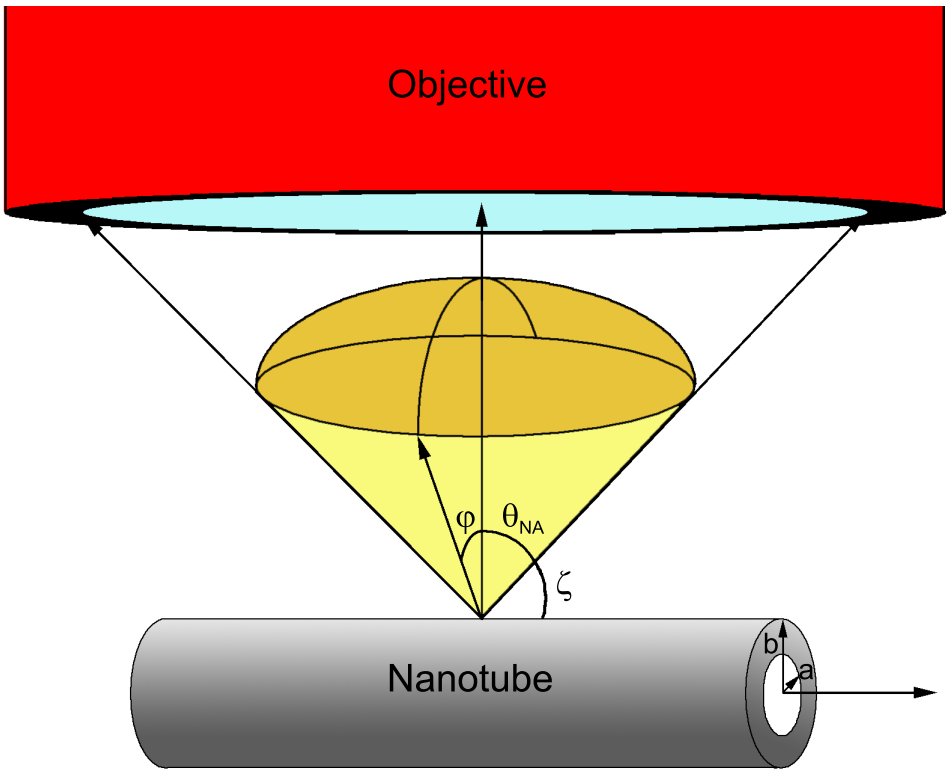

Figure 4.1: Illustration of the relative orientation of the nanotube axis to the optic axis.

For an objective having numerical aperture NA $= \sin\theta_0 = \sin\theta_0'$, simple geometry finds the nanotube angles that will enter the objective are $\eta \in [\pi/2 - \theta_0, \pi/2 + \theta_0]$ and $\phi \in [-\phi_{\max}(\eta), \phi_{\max}(\eta)]$, where

$$\phi_{\max}(\eta) = \arctan\left[\sqrt{\tan^2\theta_0 - \cot^2\eta}\right]. \tag{4.1}$$

Utilizing the symmetry of η and ϕ about the optic axis, the integral of any function $f(\eta)$ in nanotube coordinates over the objective's acceptance cone is

$$\begin{aligned} I_f &= 4\int_{\pi/2-\theta_0}^{\pi/2} f(\eta)\sin\eta d\eta \int_0^{\phi_{\max}(\eta)} d\phi \\ &= 4\int_{\pi/2-\theta_0}^{\pi/2} f(\eta)\sin\eta \arctan\left[\sqrt{\tan^2\theta_0 - \cot^2\eta}\right] d\eta. \end{aligned} \tag{4.2}$$

We use an objective that has numerical aperture NA $= .5$, or $\theta_0 = \pi/6$, and we numerically integrate for the two independent functions of η that arise in Eqs. 2.51, $f(\eta) = 1$ and $f(\eta) = \sin^2\eta$ (noting that $f(\eta) = \cos^2\eta = 1 - \sin^2\eta$),

$$\begin{aligned} I_1 &= 4\int_{\pi/2-\theta_0}^{\pi/2} \sin\eta \arctan\left[\sqrt{\tan^2\theta_0 - \cot^2\eta}\right] d\eta \approx .955, \text{ and} \\ I_{\sin^2} &= 4\int_{\pi/2-\theta_0}^{\pi/2} \sin^3\eta \arctan\left[\sqrt{\tan^2\theta_0 - \cot^2\eta}\right] d\eta \approx .896. \end{aligned} \tag{4.3}$$

Using these relations, we can integrate Eq. 2.26 over all angles that enter the objective to find the rate of light of polarization p that enters the optical system from a piece of the nanotube as

$$\int_{\text{NA}} d\dot{N}^p(l,w)d\Omega = \frac{2bc\Delta\lambda}{\lambda^4} Q^p_{\text{NA}} e^{-C_2/\lambda T(l)} H(l-L/2)H(l+L/2)H(w-b)H(w+b)dldw, \tag{4.4}$$

where the total integrated emission efficiencies are

$$\begin{aligned} Q^{||}_{\text{NA}} &\equiv \int_{\text{NA}} Q^{||} d\Omega \\ &= \pi\sigma Z_0 \left[.896 + .236\beta^2 \frac{(\sigma Z_0)^2(\beta^2+\alpha^2) + 4\beta^2(\beta-\alpha)^2}{(\sigma Z_0)^4(\beta+\alpha)^2 + 8(\sigma Z_0)^2\beta^2(\beta^2+\alpha^2) + 16\beta^4(\beta-\alpha)^2}\right], \\ Q^{\perp}_{\text{NA}} &\equiv \int_{\text{NA}} Q^{\perp} d\Omega \\ &= 3.82\pi\sigma Z_0\beta^2 \frac{(\sigma Z_0)^2(\beta^2+\alpha^2) + 4\beta^2(\beta-\alpha)^2}{(\sigma Z_0)^4(\beta+\alpha)^2 + 8(\sigma Z_0)^2\beta^2(\beta^2+\alpha^2) + 16\beta^4(\beta-\alpha)^2}. \end{aligned} \tag{4.5}$$

4.1.3 Point Spread Function

As our microscope has limited resolution, the image of the nanotube will be effectively blurred and spread over a larger area in comparison to the true object. This effect is described by the point-spread function, or PSF, which transorms a point-source of unit intensity located at $(0,0)$ in the object plane into its corresponding image under a particular optical system. For a system limited by a circular aperture, such as our microscope, the PSF is the Airy function

$$PSF(x,y) = \frac{\mathrm{NA}^2\pi}{\lambda^2}\left(\frac{2J_1((2\pi\mathrm{NA}\sqrt{x^2+y^2})/\lambda)}{(2\pi\mathrm{NA}\sqrt{x^2+y^2})/\lambda}\right)^2 \tag{4.6}$$

where J_1 is the cylindrical Bessel function of the first kind, and the normalization is such that the intensity integrated over the image plane is 1.[51]

The Airy function can be approximated by a gaussian with width $s = .21\lambda/\mathrm{NA}$,[51] with the same normalization as above,

$$PSF(x,y) \approx I_0 \frac{\mathrm{NA}^2\pi}{\lambda^2} e^{-(x^2+y^2)/2s^2}. \tag{4.7}$$

This gaussian approximation is shown alongside the original Airy function in Fig. 4.2. Although this approximation only captures 87% of the intensity on the image plane, errors are $\lesssim 6\%$ within $2s$, deviating the most from center where we expect the effect to be smallest.

Furthermore, the image plane is not actually continuous, but is divided on the CCD into discrete pixels with linear dimension β. We take the mean value as the center of the pixel (i,j),

$$\iint_{-\beta/2}^{\beta/2} e^{-[(i\beta-x)^2+(j\beta-y)^2]/2s^2} dxdy \approx \beta^2 e^{-[(i\beta)^2+(j\beta)^2]/2s^2}. \tag{4.8}$$

The errors this approximation are also small within a radius of $2s$, on the order of 1% at 1100 nm where the gaussian varies more slowly and 6% at 450 nm. While the approximation of the Airy as a gaussian underestimates the count at the furthest pixels, the averaging over a pixel overestimates, and the errors partially cancel, giving at most a $\sim 3\%$ miscount where the signal gets weak, and $\sim 1\%$ at the center. The final PSF for our system becomes, with $\mathrm{NA} = .5$,

$$PSF(i,j) = \frac{\beta^2\pi}{4\lambda^2} e^{-[(i\beta)^2+(j\beta)^2]/2(.42\lambda)^2}. \tag{4.9}$$

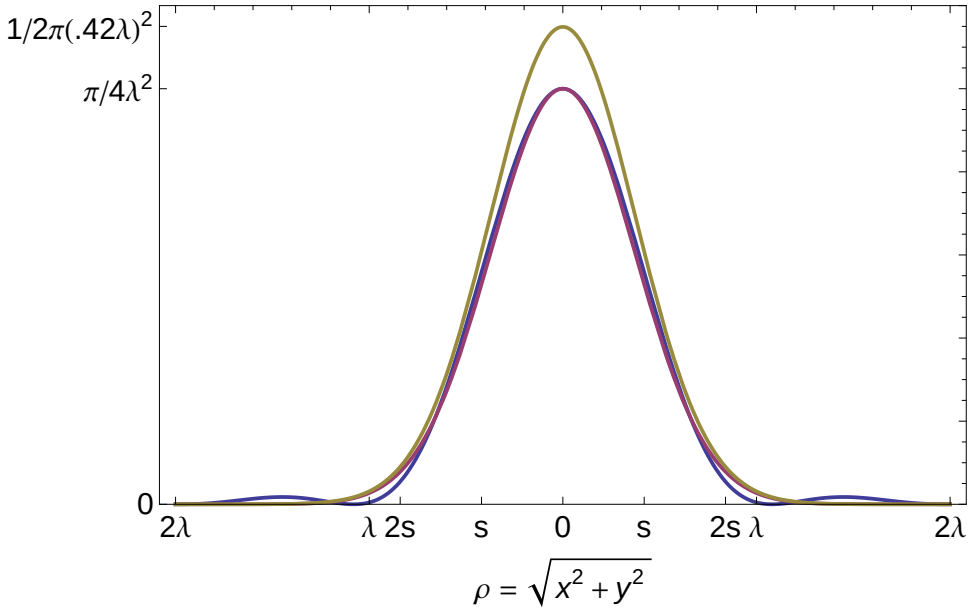

Figure 4.2: Plots of an Airy function normalized to have unit intensity over the plane (blue curve), gaussian with width $s = .42\lambda$ and same normalization as the Airy function (red curve), and gaussian with width $s = .42\lambda$ normalized to have unit intensity over the plane (yellow curve), all as functions of $\rho = \sqrt{x^2 + y^2}$. The gaussian with unit normalization overestimates the signal near $\rho = 0$ by a factor of $\sim 87\%$, but the Airy-normalized gaussian approximates the Airy function very well out to $\rho = 2s$.

4.1.4 Nanotube Image

To determine the final image we expect from the object plane intensity distribution described by Eq. 4.4, we define (x, y) as the coordinate system in the object plane oriented with the CCD. For a nanotube centered at (x_0, y_0), the parameterization of the tube is $x_t = l\cos\phi + x_0$, $y_t = l\sin\phi + y_0$, where ϕ is the angle the nanotube makes with the CCD axes.

The image of the nanotube on the CCD is the convolution of Eq. 4.4 with the PSF over the entire object plane:

$$\begin{aligned}\dot{S}^p(i,j) &= \Theta_\lambda \iint_\infty^\infty dxdyd\dot{N}^p(x,y)PSF(i\beta - x_t, j\beta - y_t) \\ &= \Theta_\lambda \iint_\infty^\infty d\dot{N}^p(l,w)PSF(i\beta - l\cos\phi - x_0, j\beta - l\sin\phi - y_0)dldw,\end{aligned} \tag{4.10}$$

rotating to tube coordinates, and where Θ_λ is the transmission efficiency of the optics at wavelength λ. Because $b \ll \beta$, in the w direction we take $H(b-w)H(b+w) \approx 2b\delta(w)$, and the integral reduces to one along the length of the tube and find

$$\begin{aligned}\dot{S}^p(i,j) &\approx 2b\int_{-L/2}^{L/2} d\dot{N}^p(l,w)PSF(i\beta - x_t, j\beta - y_t)dl \\ &= \frac{2bc\Delta\lambda}{\lambda^4}\Theta_\lambda Q^p_{\mathrm{NA}}\frac{\beta^2\pi}{4\lambda^2}\int_{-L/2}^{L/2} e^{-C_2/\lambda T(l)} \\ &\quad\times e^{-[(i\beta - l\cos\phi - x_0)^2 + (j\beta - l\sin\phi - y_0)^2]/2s^2}dl.\end{aligned} \tag{4.11}$$

The integral above can be evaluated by once again expanding $1/T(l)$ as in Eq. 2.28. The exponential now is a quadratic in l, and completing the square yields

$$\begin{aligned}\dot{S}^p(i,j) &= \frac{2bc\Delta\lambda}{\lambda^4}\Theta_\lambda Q^p_{\mathrm{NA}}\frac{\beta^2\pi}{4\lambda^2}e^{-C_2/\lambda T_{\max}} \\ &\quad\times e^{-[(i\beta - x_0)^2(1-\eta^2\cos^2\phi) + (j\beta - y_0)^2(1-\eta^2\sin^2\phi) - 2\eta^2\cos\phi\sin\phi(i\beta - x_0)(j\beta - y_0)]/2s^2} \\ &\quad\times \int_{-L/2}^{L/2} e^{-(l/\eta + [(i\beta - x_0)\cos\phi + (j\beta - y_0)\sin\phi]\eta)^2/2s^2}dl, \\ \eta &\equiv 1/\sqrt{1 + 8s^2C_2(T_{\max} - T_0)/\lambda T^2_{\max}L^2}.\end{aligned} \tag{4.12}$$

Finally, again because the largest contributions come from the center of the tube, we can extend the integral limits to $\pm\infty$ with negligible error, and the integrand becomes a gaussian whose integral evaluates to $\eta s\sqrt{2\pi}$. We define the geometric factor describing the shape and orientation of this 2-d gaussian as

$$\Phi_{ij} \equiv e^{-[(i\beta - x_0)^2(1-\eta^2\cos^2\phi) + (j\beta - y_0)^2(1-\eta^2\sin^2\phi) - 2\eta^2\cos\phi\sin\phi(i\beta - x_0)(j\beta - y_0)]/2s^2}, \tag{4.13}$$

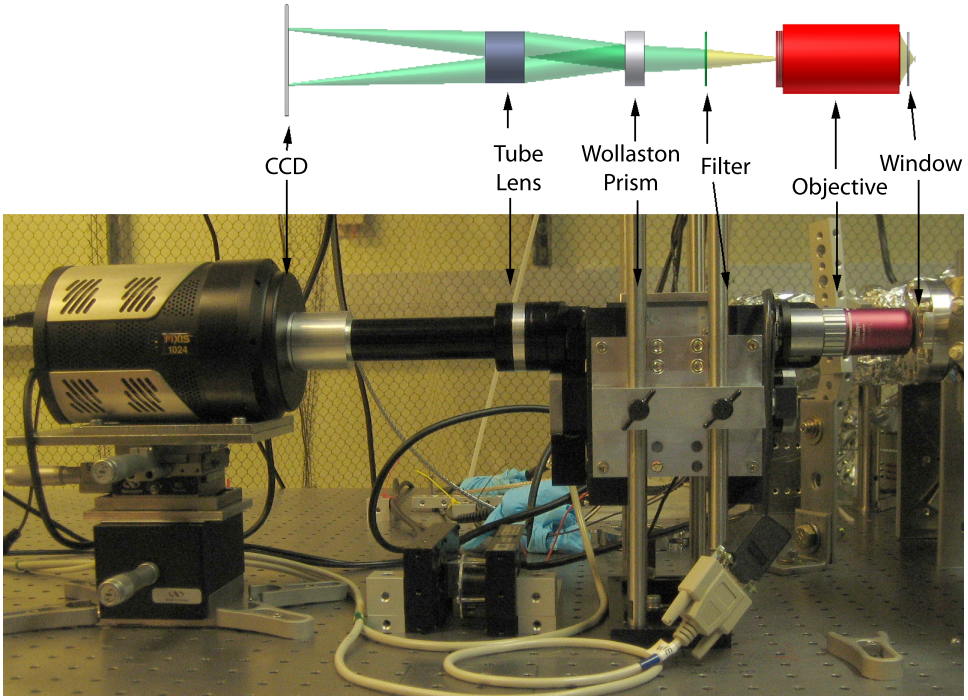

Figure 4.3: The optical microscope used to collect data from incandescent MWCNTs. An illustration of major components of the optics is shown for comparison.

whose eccentricity is given by η. The final expression for the count rate detected at pixel (i, j) becomes

$$\dot{S}^p(i,j) = \Theta_\lambda Q^p_{\mathrm{NA}} \Phi_{ij} \eta \frac{\Delta\lambda}{\lambda} \frac{2bcs}{\lambda^3} \frac{\beta^2 \pi \sqrt{2\pi}}{4\lambda^2} e^{-C_2/\lambda T_{\max}}. \tag{4.14}$$

4.2 Microscope

4.2.1 Microscope Construction

The construction of our microscope is shown in Fig. 4.3. An infinity-corrected objective collects the light, a tube lens focuses light exiting the objective, and a CCD camera records the focused image. The entire optic path is enclosed via anodized aluminum c-mount fittings to minimize noise in the image due to external light sources.

We have several infinity-corrected objectives that can be installed in the microscope, ranging from 2x magnification to 100x magnification, but the data collection is performed

using a Mitutoyo 100x NIR Apochromat objective. This objective is aberration corrected for 1.1 mm of BK7 glass–here, the window to the vacuum chamber. It has numerical aperture NA = .5 (or equivalently an acceptance angle of 30° in air), working distance $d_w = 12.13$ mm, focal length $f = 2$ mm, and depth of focus DOF = 1.1 μm. The objective is mounted on a piezo z-stage for fine focusing of the objective. The piezo can be precisely controlled to shift the objective up to 250 μm, with a precision of 10 nm. This precision is well within the objective's DOF, and allows us to focus on the nanotube with great accuracy.

Diffraction off the exit pupil of the objective, the limiting aperture in our system, determines the resolution. The exit pupil diameter is related to the numerical aperture and focal length by $\phi_{\text{exit}} = 2f\text{NA} = 2$ mm. The ratio $\phi_{\text{exit}}/2f$ thus determines the NA and the resolution $s = .21\lambda/\text{NA} = .42\lambda$ of the PSF.

The objective is infinity-corrected, *i.e.* all rays originating from the same point in the object plane converge at infinity; to form an image, therefore, it is necessary to incorporate a tube lens to focus the light emerging from the exit pupil. We use a Mitutoyo MT-L tube lens, which is aberration corrected for wavelengths ranging from 355 to 1064 nm. It has diameter $\phi_{\text{tube}} = 22$ mm on which light is incident and focal length $f_T = 200$ mm, which produces an image field up to diameter $\phi_{\text{im}} = 24$ mm.

A Pixis 1024BR camera with its CCD coincident with the image plane of the tube lens records the image. The CCD consists of a 1024×1024 array of pixels each measuring $13\ \mu\text{m} \times 13\ \mu\text{m}$, resulting in an image field of $13.3\text{ mm} \times 13.3$ mm, circumscribed by a circle of diameter $\phi_{\text{CCD}} = 18.8$ mm. Each pixel can bin $2^{16}\ e^-$, and read noise nominally ranges from 3.6 to 5 e^- rms at a readout rate of 100 kHz.

The camera is cooled to -70°C to be single-photon sensitive, and the cooling fan produces vibrations. To dampen these vibrations, once the camera is aligned with the optics, a 2-piece c-mount sleeve connecting it to the tube lens is decoupled, such that any remaining vibrations do not propagate to the objective.

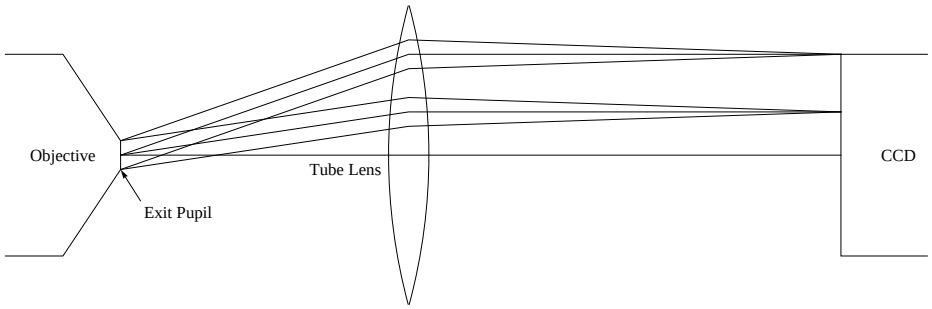

Figure 4.4: Illustration of how sets of parallel rays propagating in the infinity space with the same angle with respect to the optic axis are coincident at the same position in the image plane.

4.2.2 Infinity Space

The region between the objective's exit pupil and the tube lens is known as the infinity space. The infinity space is the Fourier transform of real space; light originating from the same point in the object plane that propagates at different angles instead propagate in the infinity space at the same angle but with a spatial offset, as illustrated in Fig. 4.4. The wavefront corresponding to the center of the object plane propagates parallel to the optical axis, whereas the edge of the image field deviates the most.

Because of this angular spread and the finite size of the tube lens, if the infinity space is too long, the signal will be vignetted. In the thin lens approximation, a paraxial ray incident an angle ξ on a lens of focal length f at a distance y from the optical axis will exit at an angle

$$\xi' = \xi - \frac{y}{f}. \tag{4.15}$$

Placing the tube lens a distance D_i behind the objective, we solve for the maximum value for D_i that forms a complete image on the CCD without vignetting.

The maximal spread originates from the edge of the exit pupil, which at the limit of visibility will be incident at the edge of the CCD, as shown in Fig. 4.5. Simple trigonometry gives this maximum angle as $\xi_{\max} = (\phi_{\text{tube}} - \phi_{\text{exit}})/2D_i$ and $-\xi' = (\phi_{\text{tube}} - \phi_{\text{CCD}})/2f_T$. Using

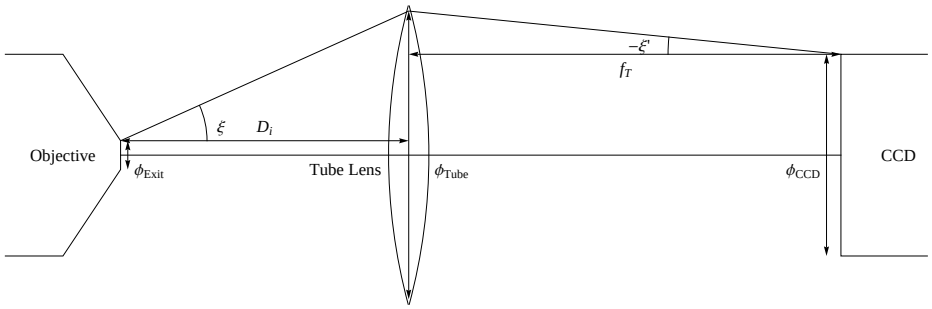

Figure 4.5: Illustration of the geometry used in the derivation of Eqs. 4.16 and 4.17. The ray shown is the extremal one that will not be vignetted by the optics.

Eq. 4.15, the maximum distance we can place the tube lens without inducing vignetting is

$$D_i = \frac{(\phi_{\text{tube}} - \phi_{\text{exit}}) f_T}{\phi_{\text{CCD}}}, \tag{4.16}$$

corresponding to a maximum angular spread of

$$\xi_{\text{max}} = \frac{\phi_{\text{CCD}}}{2 f_T}. \tag{4.17}$$

For our microscope, we will not experience vignetting for $D_i \leq 212$ mm. The maximum infinity space angle the CCD captures is $\xi_{\text{max}} = 2.7°$, corresponding to imaging at the corner of the CCD. The paraxial approximation in our infinity space is thus validated, as all pertinent angles are small. Equation 4.17 yields the relation between angular spread and CCD shift, as 512 pixels corresponds to an angle of 1.9°, and

$$\frac{\Delta \vec{x}_i}{\Delta \xi} \approx 269.5 \ \frac{\text{pixels}}{\text{deg}}. \tag{4.18}$$

This relation determines the angular deflection optimal for simultaneously imaging orthogonal polarizations or a diffracted spectrum of an object.

4.2.3 Measurement of the Magnification

We determine the true magnification of the optics by imaging a Ronchi ruling, shown in Fig. 4.6. Our CCD consists of an array of 13 μm $\times$ 13 μm pixels, so at 100$\times$ magnification we expect the effective pixel linear dimension to be $\beta = 130$ nm. The Ronchi ruling utilized

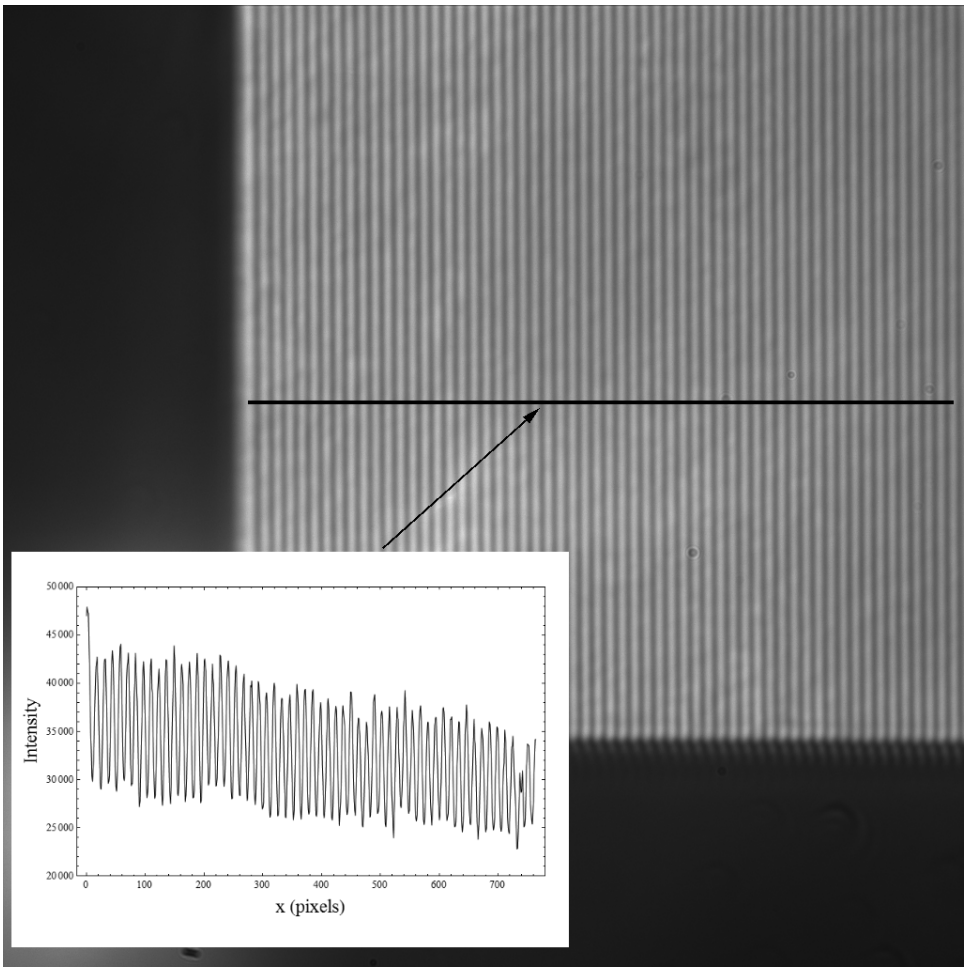

Figure 4.6: Front-illuminated Ronchi ruling as imaged using our microscope with NIR 100× objective. The inset shows a line profile, indicated on the image, used in determining the apparent spacing of line pairs and thus the magnification.

has a spacing of 600 line pairs/mm, so we expect each line pair to span about 12.82 pixels. Instead we measure 13.09 pixels/line pair, corresponding to a magnification of $M' = 102.1\times$. This magnification differs significantly from the nominal objective magnification. Mitutoyo confirms that the objective is calibrated for an accurate d_w, such that the nominal value of M is approximate. Therefore, the true magnification of the microscope is 102.1×, and $\beta = 127$ nm is the effective pixel linear dimension.

4.2.4 Spherical Aberration Correction

Aberrations introduced into imaging by the optics will distort the image from that predicted by Eq. 4.14. The objective is corrected for spherical aberration induced by the flat BK-7 vacuum window of 1.1 mm thickness. However, strains from the pressure differential of the vacuum system will distort the window profile, introducing spherical aberrations that are not corrected. To quantify the amount present in our imaging it is necessary to calculate the amount for which the objective corrects.

Using geometric optics, a light ray emanating at an angle θ passing through a window of thickness t and index of refraction n tilted at an angle ϕ_w from the optical axis will appear to be originating from a position on the axis shifted by

$$Sph_L(t,n,\theta,\phi_w) = \frac{t}{\cos\phi_w}\left[1 - \frac{\cos\phi_w \sin(\theta+\phi_w) - \sin\phi_w\sqrt{n^2-\sin^2(\theta+\phi_w)}}{\tan\theta(\sqrt{n^2-\sin^2(\theta+\phi_w)} + \tan\theta\sin(\theta+\phi_w))}\right]. \quad (4.19)$$

This equation represents the longitudinal spherical aberration, a shift in the apparent position of an image as illustrated in Fig. 4.7. Because the shift is a function of θ, the object's position as integrated over the range of θ collected the objective leads to an apparent defocus.

Because the window and chip holder are bolted to be normal to the optical axis, we can take $\phi_w \to 0$ and expect a spherical abberation of

$$Sph_L(t,n,\theta) = t\left(1 - \frac{\cos\theta}{\sqrt{n^2-\sin^2\theta}}\right). \quad (4.20)$$

BK7's index of refraction is well known and can be described by the Sellmeier equation,[1]

$$\begin{aligned} n^2(\lambda) = 1 &+ \frac{1.03961212\lambda^2}{\lambda^2 - 6.00069867\times10^3\ \text{nm}^2} + \frac{0.231792344\lambda^2}{\lambda^2 - 2.00179144\times10^4\ \text{nm}^2} \\ &+ \frac{1.01046945\lambda^2}{\lambda^2 - 1.03560653\times10^8\ \text{nm}^2}, \end{aligned} \quad (4.21)$$

plotted in Fig. 4.8. Thus the index of refraction at the extreme values of our wavelength range of interest are $n(450\text{ nm}) = 1.52532$ and $n(1100\text{ nm}) = 1.50617$. Our window's thickness is $t = 1.1$ mm, and the maximum angle accepted by our 100x objective is $\theta = 30°$. This gives a maximum aberration that is corrected by the objective of $Sph_L(30°) \approx .43983$ mm at $\lambda = 450$ nm and $\approx .42949$ mm at $\lambda = 1100$ nm. The spherical aberration by a window is thus two orders of magnitude larger than the DOF, and the correction the objective provides is essential to imaging.

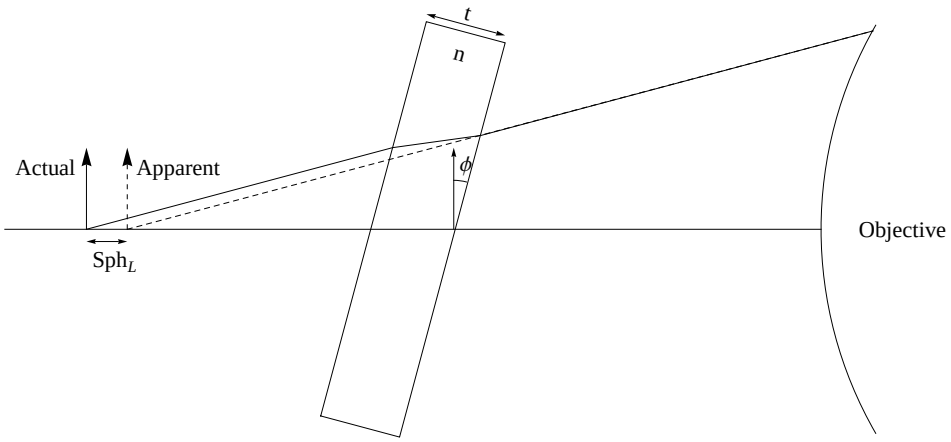

Figure 4.7: Illustration of the longitudinal spherical aberration induced by a planar window. The apparent position of the object shifts by a quantity Sph_L along the optical axis.

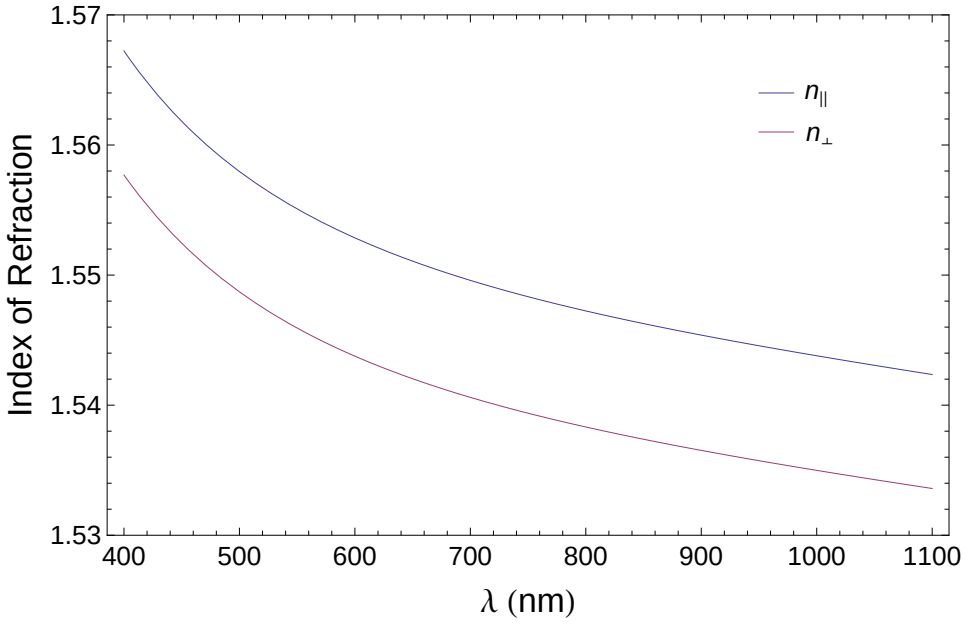

Figure 4.8: The two independent indices of refraction of quartz in the visible and NIR, as generated from the Sellmeier coefficients from Ref. [1].

4.2.5 Aberration From Window Bending

The vacuum window is under a pressure differential, distorting the window away from the ideal planar geometry and introducing aberration for which the objective does not correct. This displacement from equilibrium w due to the pressure differential p follows the plate equation

$$\nabla^2 \left(\frac{Et^3}{12(1-\nu^2)} \nabla^2 w \right) = p \tag{4.22}$$

where E is the Young's modulus, ν the Poisson's ratio, and t the thickness of the window.[35] The quantities E and ν are constant throughout the window, and with the boundary equations that the window is circularly clamped at radius r_0, the displacement a radius r from the origin is

$$w(r) = \frac{3pr_0^4(1-\nu^2)}{16Et^3} \left[1 - \left(\frac{r}{r_0} \right)^2 \right]^2 . \tag{4.23}$$

Figure 4.9 shows the profile of a window undergoing such a bend. We calculate the spherical aberration numerically using the values $E = 8.2 \times 10^4$ N/mm^2 and $\nu = 0.206$ for BK-7.[1] A numerical calculation of the apparent image shift as a function of angle incident on this window profile by repeated application of Snell's law. The maximum spherical aberration, given by subtracting the objective correction from the calculated aberration, is ~ 80 nm over the wavelength range. The uncorrected aberration is over an order of magnitude smaller than the depth of focus; therefore, all spherical aberrations induced by the bending of the BK-7 window will not affect a focused image.

4.3 Infinity Space Optics

4.3.1 Filters

With the use of one of 14 small bandpass color filters, light of a particular wavelength is singled out and analyzed. Directly behind the objective and piezo focuser are two 10 position high-speed filter wheels. We have a set of filters from Chroma which transmit wavelengths from 450 to 1100 nm in 50 nm increments. The bandpass of these filters is $\Delta\lambda = 10 \pm 1$ nm, and the central wavelengths differ from nominal by $\lambda = \lambda_0 \pm 2$ nm, an error on the order of

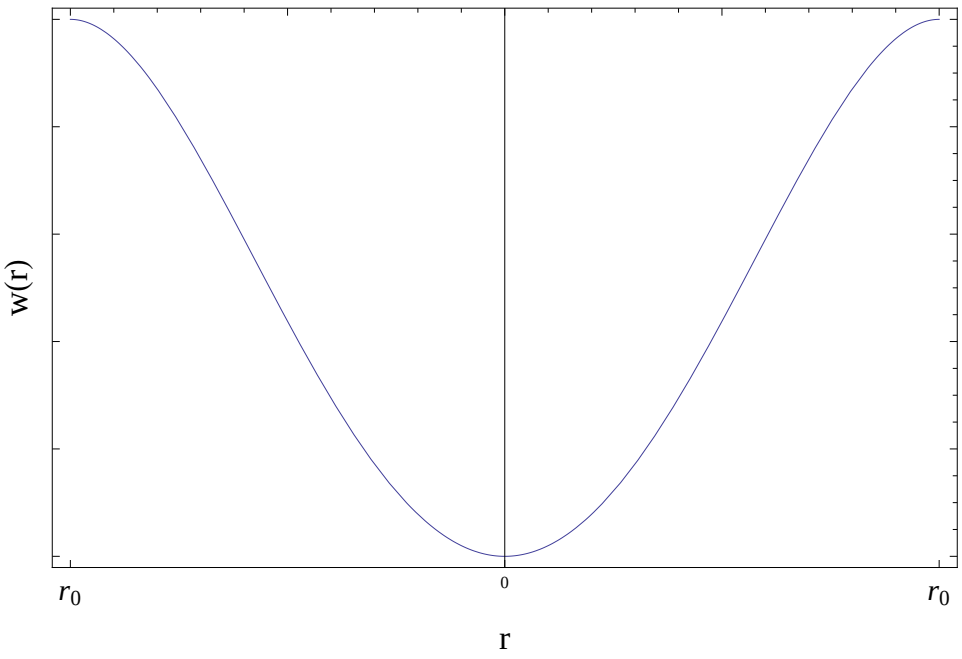

Figure 4.9: Profile of the displacement as a function of radius of a window clamped at r_0 under a pressure differential p from above.

$\sim 0.1\%$. Half of these filters are placed in each wheel, with one position per wheel kept open for total transmission and one blocked for dark current measurements.

4.3.2 Diffraction Grating

A diffraction grating placed in the infinity space produces finer spectral measurement than provided by the filters. We mount a diffraction grating with line spacing $d^{-1} = 35$ grooves/mm on a rotation stage such that we can orient the diffracted image on the CCD normal to the tube axis. By Eq. 4.18 and the first-order diffraction condition

$$d \sin \theta = \lambda, \tag{4.24}$$

this grating produces a wavelength-dependent shift relative to the 0th order maxima of

$$\frac{\Delta x}{\Delta \lambda} = .5376 \text{ pixels/nm}. \tag{4.25}$$

The diameter of the grating is 20 mm; thus the resolvance at first-order is

$$\frac{\lambda}{\Delta \lambda} = 700, \tag{4.26}$$

implying that at wavelengths below 1300 nm, pixel size limits resolution of wavelength. The PSF spreading of the image is the dominant limitation of resolution of the diffracted spot; perpendicular to the tube axis, the number of unresolved pixels is $\Delta x = s/2\beta$. The experimental resolvance is thus

$$\frac{\lambda}{\Delta \lambda} = \frac{.5376\beta}{.21} \approx 325. \tag{4.27}$$

Below 650 nm, the resolution is limited by 1 pixel, corresponding to $\Delta\lambda \approx 2$ nm; at 975 nm the resolution is limited by 3 pixels and $\Delta\lambda \approx 6$ nm. Therefore, although the range of wavelengths that can be captured in one exposure is limited by the sensitivity of the optics, the diffraction grating allows a greater spectral sensitivity over a continuum of wavelengths compared to the discrete values selected by the filters.

4.3.3 Polarizer

Simultaneous imaging of two independent polarizations of light with our optics is achieved by the introduction of a Wollaston prism. A Wollaston prism is comprised of two wedges of

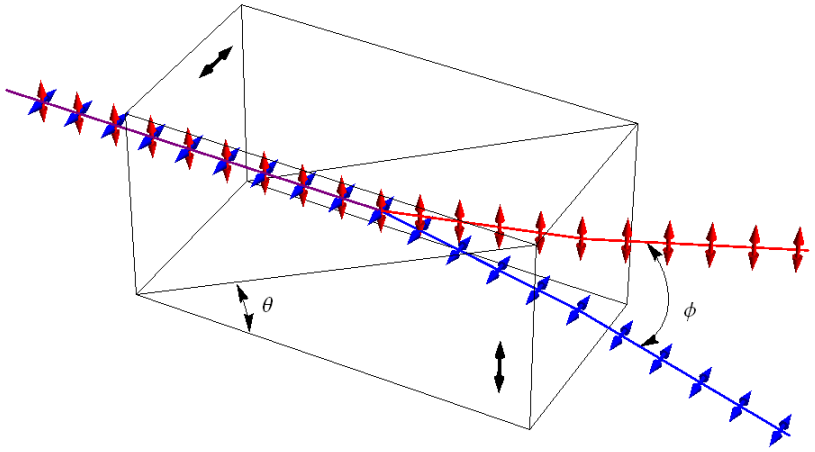

Figure 4.10: Illustration of a Wollaston prism. It is comprised of two wedges of quartz cut and glued together such that the fast axes are perpendicular. Refraction at the interface between the wedges separates the two linear polarizations of incident light by an angle ϕ.

a birefringent material combined such that the orientation of the fast and slow axes in the first wedge is orthogonal to that in the second wedge. Due to the angle θ of the wedge, the mismatch of the two indices of refraction $n_{||}$ and $n_{\perp}$, and Snell's law, the two orthogonal polarizations of normally incident light split by an angle ϕ, shown in Fig. 4.10.

Our prism, built by Red Optronics, is made of quartz. Using the indices of refraction of quartz plotted in Fig. 4.8 and the nominal prism separation $\phi(1064\text{ nm}) = 2°$, we calculate $\theta = 28.14°$. This value then allows us to calculate $\phi(\lambda)$, and applying Eq. 4.18, the corresponding separation on the CCD, plotted in Fig. 4.11. Images belonging to two orthogonal polarizations appear roughly 550 pixels apart, about half the size of the CCD, easily allowing simultaneous capture of data of orthogonal polarizations.

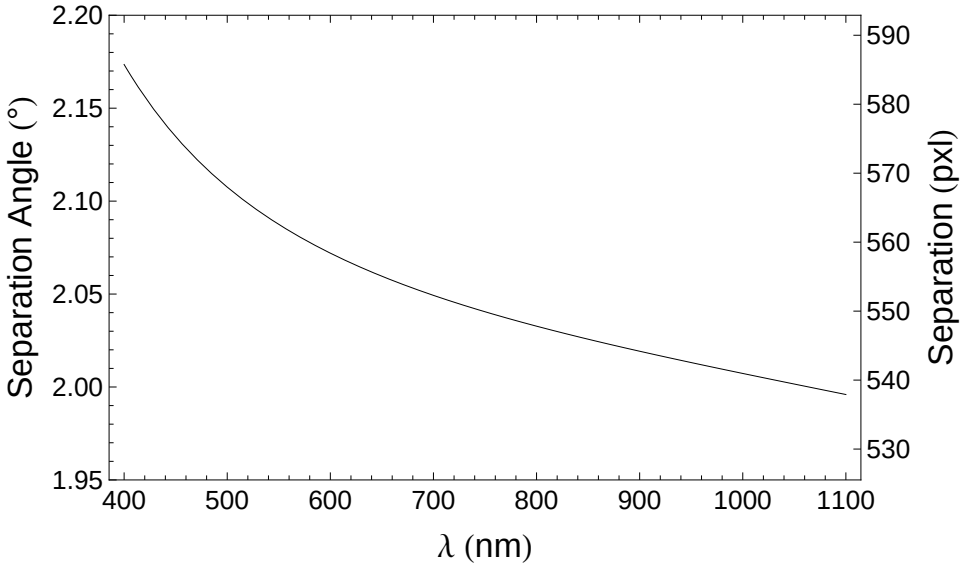

Figure 4.11: Separation angle ϕ and corresponding CCD pixel separation of two orthogonal polarizations due to the Wollaston prism as a function of wavelength.

4.4 Calibration

4.4.1 Wavelength-dependent Quantum Efficiency of Microscope

Because the optics reflect and absorb some of the light being collected, not every photon emitted by the CNT will be recorded by the CCD. To translate between the absolute emission of the MWCNT and the signal measured on the CCD we must measure the total transmission of the optics, Θ_λ, that arises in Eq. 4.14. The microscope and camera's combined quantum efficiency is measured using a 45 W tungsten lamp from Newport, for which the spectral flux at a radial distance of 50 cm has been NIST calibrated. Placing a 100 μm sized pinhole this distance from the lamp and focusing on the pinhole with the microscope through a glass window identical to the one in the vacuum chamber allows us to determine the number of photons entering the optics; the setup is illustrated in Fig. 4.12. All collected photons enter the system essentially parallel to the optical axis, as the pinhole subtends a very small solid angle with respect to the tungsten lamp.

The irradiance at a distance of 50 cm from the NIST-calibrated lamp is given as

$$V(\lambda) = \lambda^{-5} e^{-(A+B/\lambda)} \left(C + \frac{D}{\lambda} + \frac{E}{\lambda^2} + \frac{F}{\lambda^3} + \frac{G}{\lambda^4} + \frac{H}{\lambda^5} \right) \tag{4.28}$$

in units of mW/m^{2}nm, with coefficients given in Table 4.1. This irradiance has a fractional uncertainty in quadrature sum of 2.8% in the wavelength range from 350 to 1300 nm. The irradiance can be converted to a photon flux per second by dividing by the energy per photon, and the CCD will see

$$\dot{N}_{45W,theo} = \frac{\beta^2 \lambda \Delta\lambda}{hc} V(\lambda), \tag{4.29}$$

photons per pixel per second. The ratio of the measured count rates to the expected photon rates gives the efficiency of the combined window, objective, filter, tube lens, and CCD system,

$$\Theta_0(\lambda) = \frac{\dot{S}_{45W,meas}(\lambda)}{\dot{N}_{45W,theo}(\lambda)}, \tag{4.30}$$

which has units of counts/γ. The subscript indicates that this quantum efficiency is measured for light entering along the optical axis.

An image of the pinhole at 550 nm is shown in Fig. 4.13. The pinhole fills most of the field of view, and its diameter of 100 μm is large compared to the thickness, minimizing

A	41.7133782879188	E	-157161.599513603
B	-4746.26164221276	F	20868242.470864
C	0.874214800828613	G	-297635686.081756
D	271.591151286481	H	0

Table 4.1: Calibration parameters of Eq. 4.28 given for the NIST calibrated tungsten standard lamp (values from lamp calibration literature).

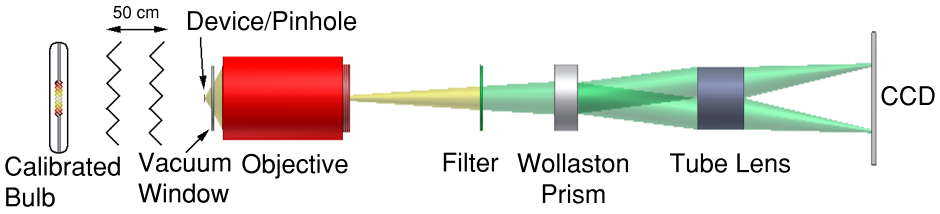

Figure 4.12: Cartoon of calibration setup, with 45 W standard lamp placed 50 cm behind pinhole.

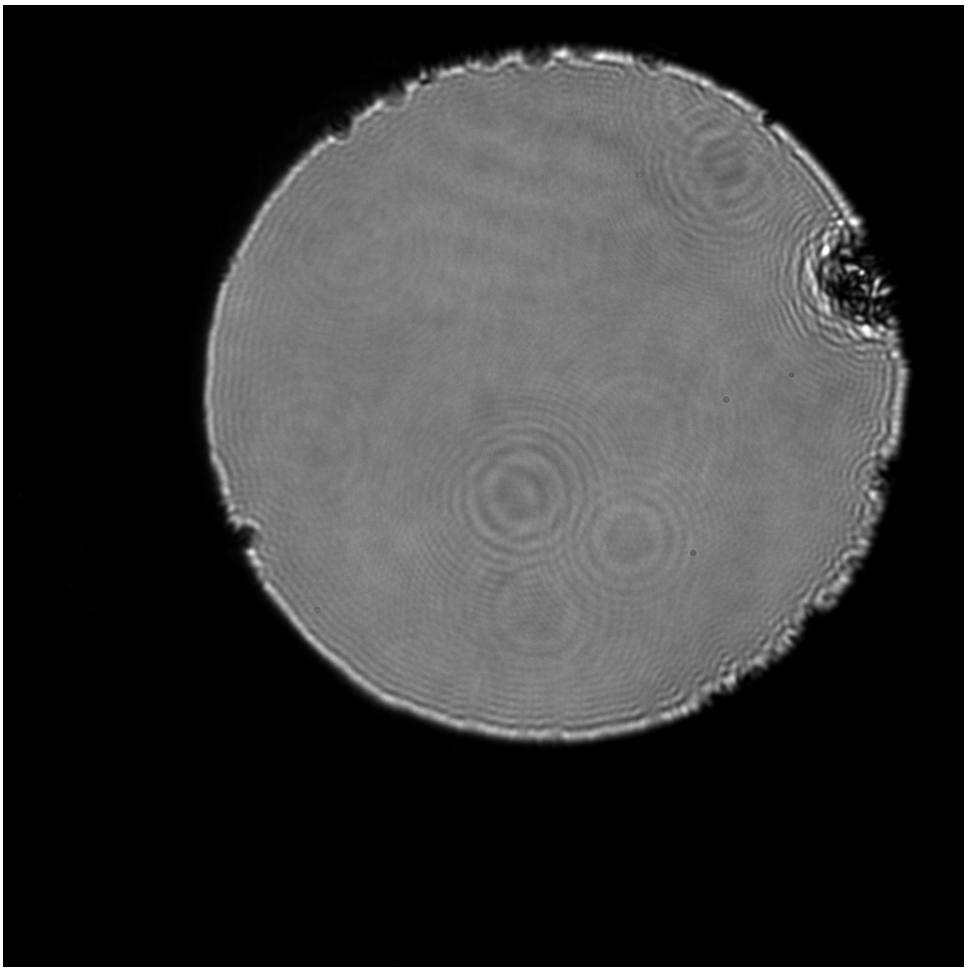

Figure 4.13: Calibration image of pinhole using the 550 nm filter.

diffraction and reflection effects, which are only observed at the very edge of the pinhole. The calibration images show Airy distortions, which are unique to images taken with a particular filter. These distortions also increase in size with wavelength, indicating that they are projections of point defects in the filters themselves. To account for the fluctuations caused by these defects, we average $\dot{N}_{45W,theo}$ over a large ROI of $\sim 10^5$ pixels to obtain the total quantum efficiency at normal incidence Θ_0.

This calibration method yields only the quantum efficiency at normal incidence, yet the nanotubes studied emit into all solid angles collected by the objective. As has been previously shown, the paraxial approximation is valid in the infinity space; therefore, any deviations expected between the quantum efficiencies of off-axis photons and on-axis photons depend only on the transmission efficiencies of the glass window and the front of the objective,

assuming losses within the objective itself are independent of entry angle. Designating the indices of refraction of the imagining medium as n_0, the window as n_1, and the objective as n_2, the angle-dependent transmission coefficients of the window and objective entrance are

$$T_\perp(\theta) = \frac{8n_0^2\cos\theta\cos(\theta+\kappa)\sqrt{n_1^2-n_0^2\sin^2\theta}}{[n_0\cos\theta+\sqrt{n_1^2-n_0^2\sin^2\theta}]^2[n_0\cos(\theta+\kappa)+\sqrt{n_2^2-n_0^2\sin^2(\theta+\kappa)}]} \tag{4.31a}$$

$$T_{||}(\theta) = \frac{8n_0^2n_1^2n_2\cos\theta\cos(\theta+\kappa)\sqrt{n_1^2-n_0^2\sin^2\theta}}{[n_1^2\cos\theta+n_0\sqrt{n_1^2-n_0^2\sin^2\theta}]^2[n_2^2\cos(\theta+\kappa)+n_0\sqrt{n_2^2-n_0^2\sin^2(\theta+\kappa)}]} \tag{4.31b}$$

for electric field perpendicular and parallel to the plane of the window, respectively, and where θ is the angle of incidence on the objective as measured from the optic axis and κ is related to the radius of curvature R of the objective lens, window thickness t, and objective working distance L by

$$\kappa = \sin^{-1}\left(\frac{\left[L+t\left(\frac{n_0\cos\theta}{\sqrt{n_1^2-n_0^2\sin^2\theta}}-1\right)\right]\tan\theta}{R}\right). \tag{4.32}$$

With $n_1 = n_2 \approx 1.5$ for BK-7, $n_0 = 1$, $t = 1.1$ mm, and $L = 11.76$ mm, we integrate over all solid angles accepted by the objective, normalized by the corresponding calculation in the approximation that $\Theta(\lambda) = \Theta_0(\lambda)$. We take two limits of the objective entrance lens's shape to bound the error on this approximation: for a planar geometry, $R = \infty$ and

$$\frac{\int_0^\pi d\theta\sin\theta(T_\perp^2(\theta)+T_{||}^2(\theta))}{\int_0^\pi d\theta\sin\theta(T_\perp^2(0)+T_{||}^2(0))} \approx .942, \tag{4.33}$$

and for a plano-convex geometry, $R = 10.8$ mm and

$$\frac{\int_0^\pi d\theta\sin\theta(T_\perp^2(\theta)+T_{||}^2(\theta))}{\int_0^\pi d\theta\sin\theta(T_\perp^2(0)+T_{||}^2(0))} \approx .879. \tag{4.34}$$

Although the objective lens's exact shape is not known, these two bounds allow us to approximate the error in setting $\Theta(\lambda) = \Theta_0(\lambda)$ at $\sim 10\%$, overshadowing the error caused by the lamp fluctuations.

4.4.2 Polarization-dependent Transmission of Wollaston Prism

Placing the Wollaston prism in the calibration setup as described previously, a filter stack is taken with the prism separation aligned parallel to the optical table (horizontal splitting on

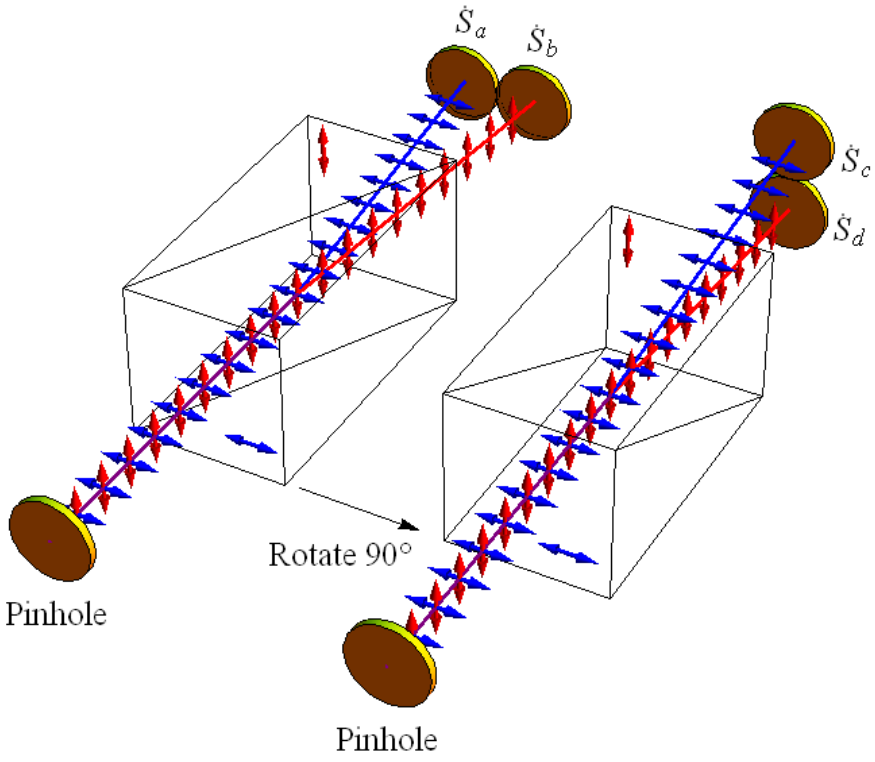

Figure 4.14: The polarizer splits the image of the pinhole into two images, with each polarization aligned with the fast axis of one of the prism halfs. A rotation of 90° inverts the fast axes.

the CCD) and a second one with the prism perpendicular (vertical splitting on the CCD). We define $\Theta_{||}(\Theta_{\perp})$ as the quantum efficiency of all the optics for incident light aligned parallel (perpenicular) to the fast axis of the initial half of the prism.

The standard lamp emits light which may be slightly polarized, so the total rate of photons emitted is equal to the sum of these two polarizations: $\dot{N}_{\rm tot} = \dot{N}_{||} + \dot{N}_{\perp}$. The detected photons are then

$$\begin{aligned} \dot{S}_a &= \Theta_{||}\dot{N}_{||}, & \dot{S}_b &= \Theta_{\perp}\dot{N}_{\perp} \\ \dot{S}_c &= \Theta_{\perp}\dot{N}_{||}, \quad \text{and} & \dot{S}_d &= \Theta_{||}\dot{N}_{\perp}, \end{aligned} \tag{4.35}$$

where $\dot{S}_a$ ($\dot{S}_c$) and $\dot{S}_b$ ($\dot{S}_d$) are the detection rates for the splitting parallel (perpendicular)

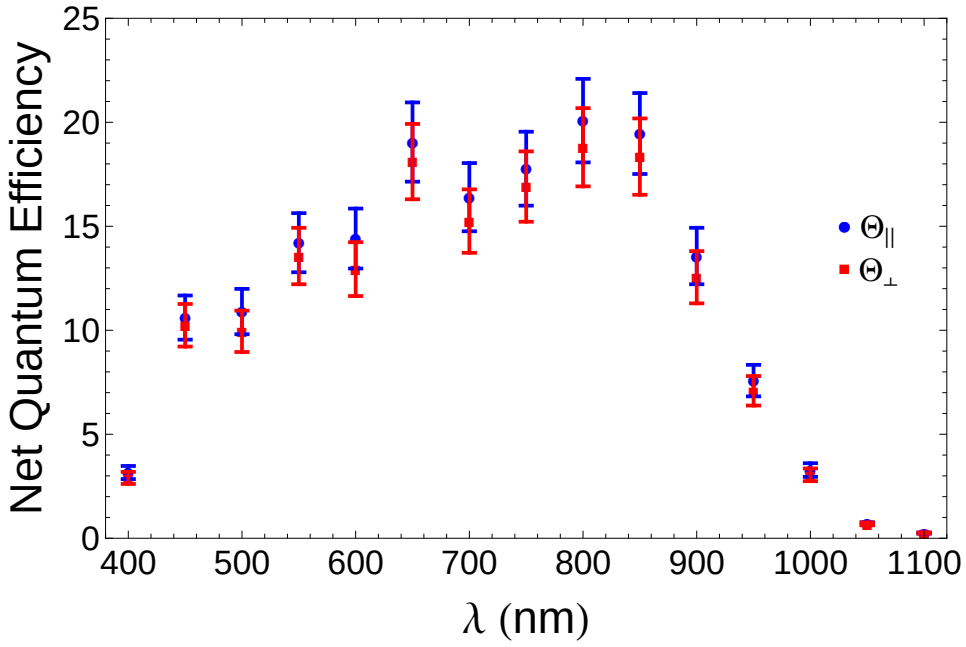

Figure 4.15: Net quantum efficiencies of the microscope, camera, and wollaston prism at each filter for "parallel" (aligned along fast axis of prism wedge towards objective) and "perpendicular" (aligned along fast axis of prism wedge towards CCD) polarizations of light.

to the optical table, illustrated in Fig. 4.14. Solving for $\Theta_{||}$ and $\Theta_{\perp}$,

$$\Theta_{||} = \frac{\dot{S}_a + \dot{S}_d}{\dot{N}_{\rm tot}} \quad \text{and} \quad \Theta_{\perp} = \frac{\dot{S}_b + \dot{S}_c}{\dot{N}_{\rm tot}}. \tag{4.36}$$

Figure 4.15 plots the measured values of $\Theta_{||}$ and $\Theta_{\perp}$ used in the analysis of polarized MWCNT data. The quantum efficiency is highest in the 700-900 nm range, dropping off both at long wavelengths due to the bandgap of the Si comprising the CCD and at short wavelengths due to the objective's sensitivity's being optimized in the NIR.

4.4.3 Tests of Calibration

To test the calibration, we examine the spectra of macroscopic radiators, which have linear size $r \gg \lambda > \beta$. In this dimension limit, the PSF integrates out of the image, and the pixel count rate is

$$\frac{\dot{S}(i,j)}{\Theta_\lambda} = \pi(\mathrm{NA})^2 \epsilon \frac{2c\beta^2\Delta\lambda}{\lambda^4} e^{-C_2/\lambda T}, \tag{4.37}$$

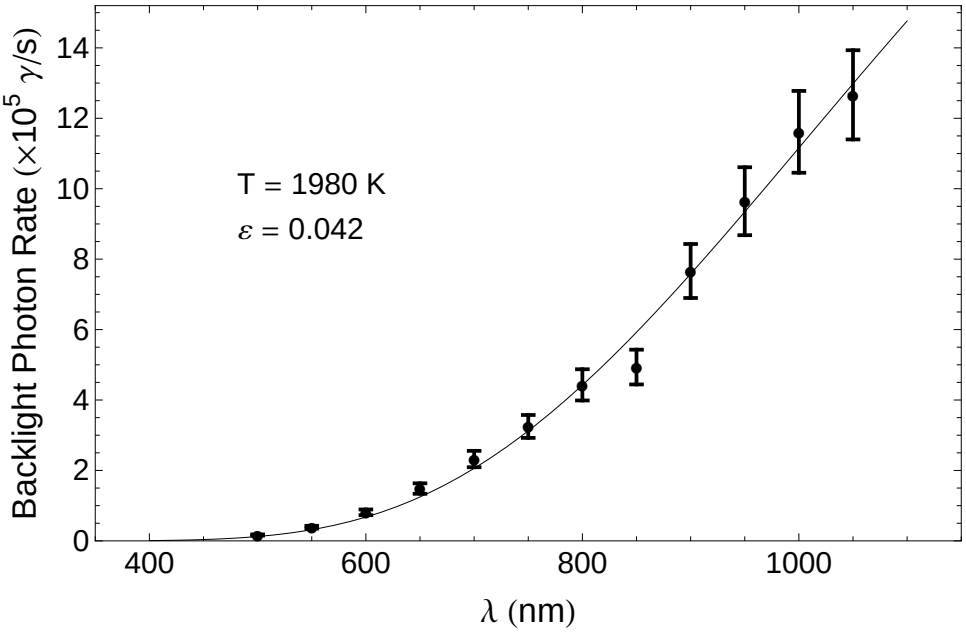

Figure 4.16: Spectrum and graybody fit to backlight data.

having assumed a Lambertian radiation profile. The intensity is uniform over the image.

The backlight which sits behind the microchip within an aluminum cavity mimics a blackbody cavity to lowest order. Taking a set of images without a device in the vacuum chamber produces images with uniformity varying by $\lesssim 1\%$ over the entire CCD at $100\times$ magnification. Optimizing the images to average $\geq 2 \times 10^4$ counts above background, the error in the quantity $\dot{N} = \dot{S}/\Theta\lambda$ is

$$\delta\dot{N} = \dot{N}\sqrt{\left(\frac{\delta S}{S}\right)^2 + \left(\frac{\delta\Theta_\lambda}{\Theta_\lambda}\right)^2} = \dot{N}\sqrt{\left(\frac{\sqrt{S}}{S}\right)^2 + \left(\frac{\delta\Theta_\lambda}{\Theta_\lambda}\right)^2} = \dot{N}\sqrt{\frac{1}{S} + \left(\frac{\delta\Theta_\lambda}{\Theta_\lambda}\right)^2} \tag{4.38}$$
$$\approx \dot{N}\sqrt{5\times 10^{-5} + .01} \approx .1\dot{N},$$

with the calibration error completely overshadowing the shot noise contribution. The spectrum of the backlight, shown in Fig. 4.16, fits the graybody spectrum given by the right hand side of Eq. 4.37 very well with a temperature of 1930 ± 40 K.

In addition to the blackbody approximated by the backlight, we construct a radiating tungsten filament by biasing a length of 10 μm diameter tungsten wire, allowing us to test

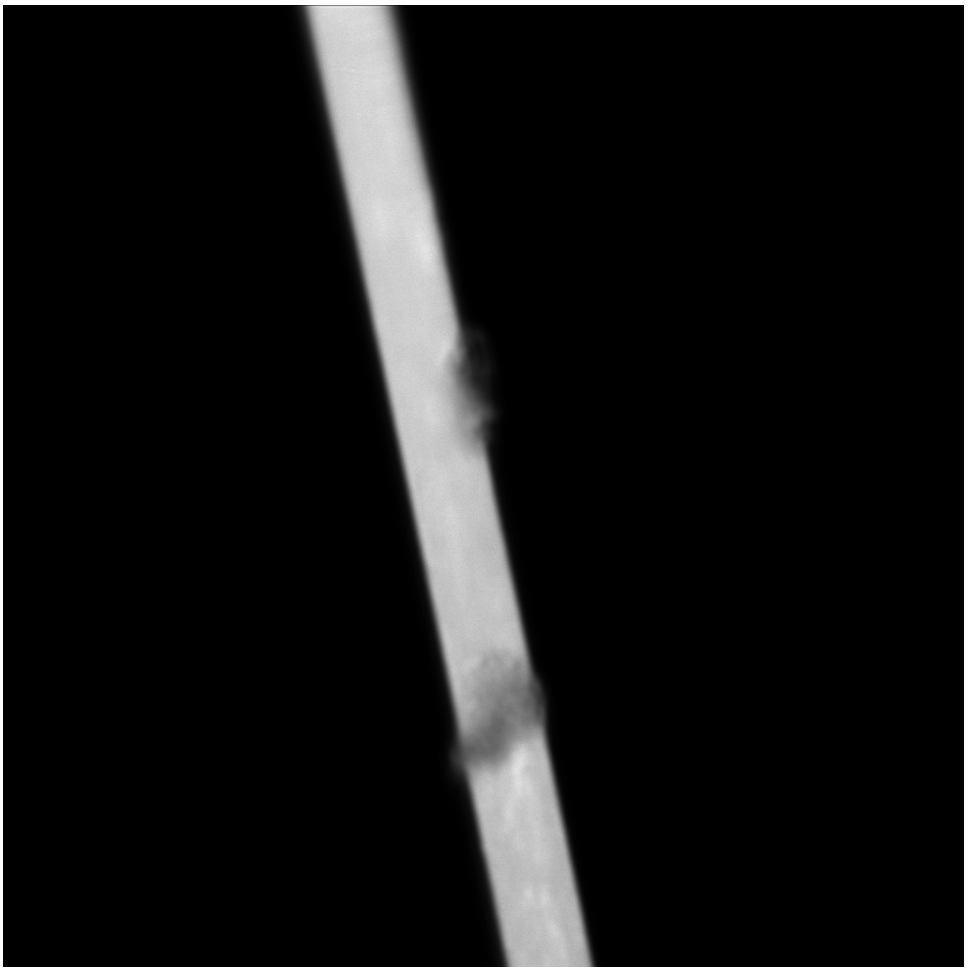

Figure 4.17: Image of incandescent tungsten filament.

Eq. 4.37 for a directly imaged radiator in the object plane. Figure 4.17 shows a representative image of this tungsten filament. Applying voltages ranging from 0.90 V to 1.10 V produce the spectra of Fig. 4.18, and the graybody fits indicate that the temperature of the filament varies by 150 K over this biasing range. Thus, the calibration allows us to measure the temperature of gray objects over the accessible wavelength range, and we can confidently apply Θ_λ to data from MWCNT filaments.

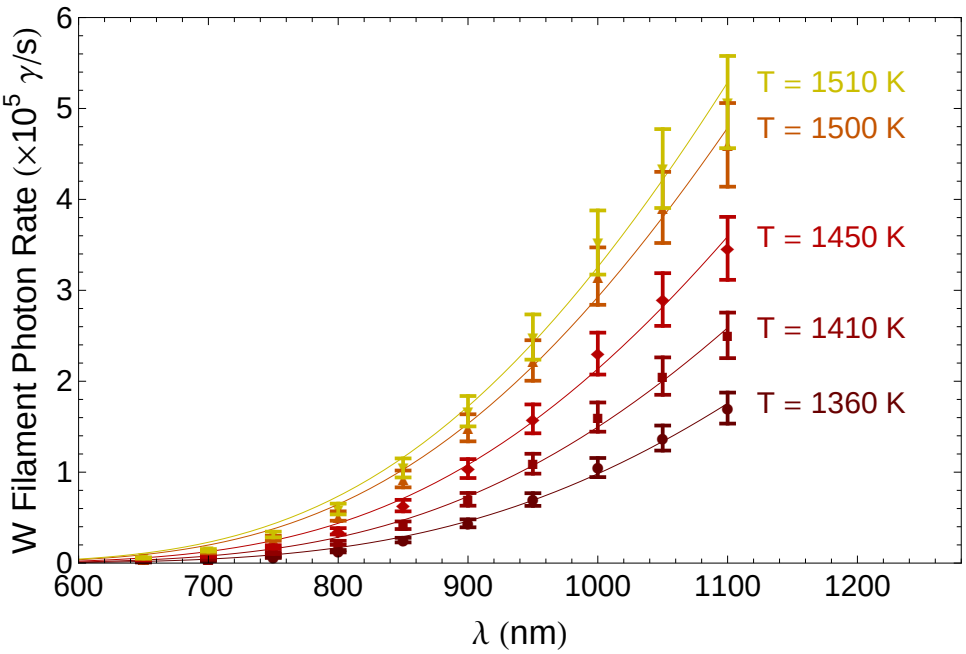

Figure 4.18: Spectra and graybody fits to tungsten filament at varying powers.

CHAPTER 5

Pyrometry of MWCNTs

5.1 Optical Data

5.1.1 Gaussian Bright Spot

With the optics constructed and characterized, we take images of incandescent nanotubes varying over applied power, filter, and polarization. Figure 5.1 shows a representative image of a nanolamp captured by the full CCD. The nanotube's bright spot occupies only a few pixels at 102.1× magnification. The CCD is 16-bit, but we adjust for the noise present in the least-significant bit, such that a given image saturates at $2^{15} = 32768$ counts. We adjust the exposure time such that the brightest pixel has between 2×10^4 and 3×10^4 counts, provided that the exposure is under 2 minutes. Dark current generates a background noise of ~ 300 counts, measurable on each picture by averaging a region far away from the nanotube's bright spot. As the counting error due to shot noise $\sigma_S = \sqrt{S}$, pixels with $S_{ij} > 10^4$ counts are accurate to $< 1\%$. A 2-dimensional gaussian fit to this data gives the angle ϕ and center (x_0, y_0) of the nanotube to an accuracy of .1° and .01 pixels, respectively. Although the first Airy bump is visible in a typical exposure, the fit to a gaussian has $\chi^2 \approx 1$, and therefore supports our model in Eq. 4.14.

5.1.2 Nanotube Location

Operating the backlight in conjunction with the nanolamp, we can determine visually that the bright spot in Fig. 5.1 originates from the MWCNT, as opposed to a contact or debris on the membrane heating up. Figure 5.2 shows this backlit membrane with the nanolamp both off and on. Comparison of the two pictures indicates that the origin of the bright spot

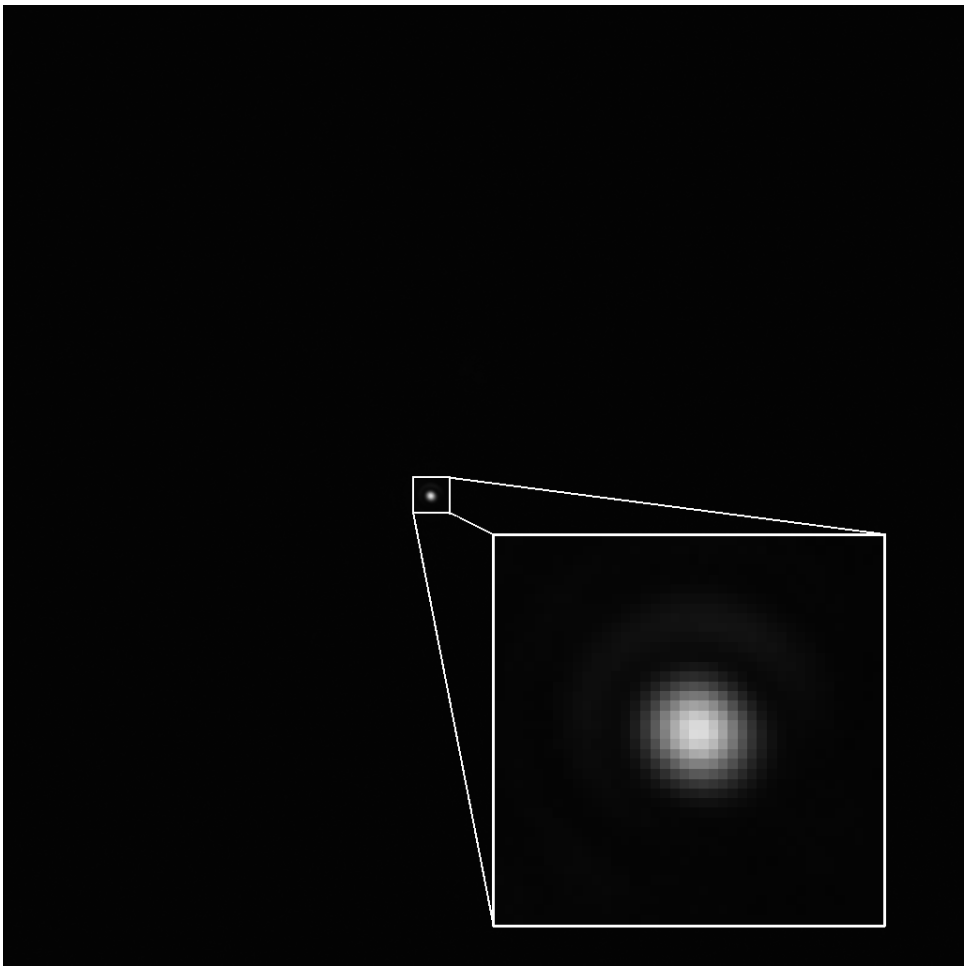

Figure 5.1: A representative nanolamp exposure taken by the CCD. As most of the CCD captures no signal other than dark current, a zoomed view of the bright spot is also shown. The first Airy minimum is visible, but the image very closely approximates the gaussian predicted by Eq. 4.14.

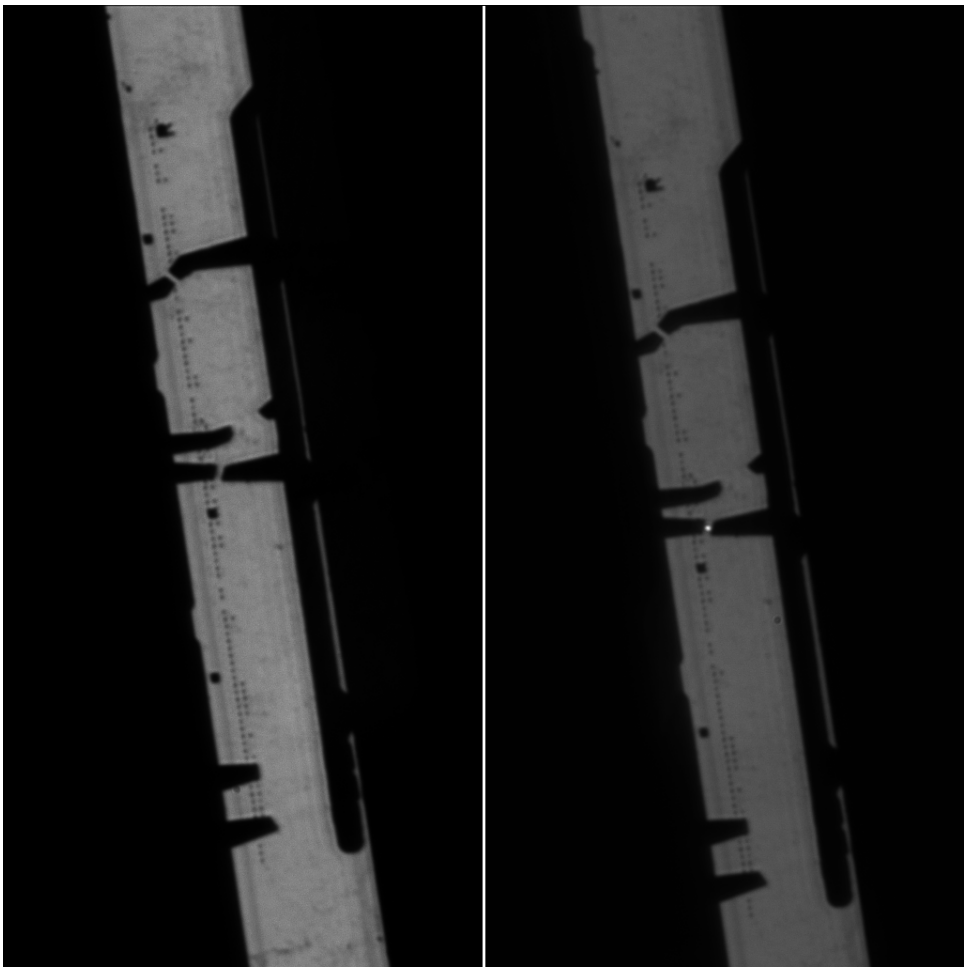

Figure 5.2: Images of a chip's membrane backlit by lightbulb using 500 nm filter. In the left image the nanolamp is off; in the right image the nanolamp is on. The bright spot is clearly between the contacts, identifying it with the nanotube.

is directly between the two contacts.

These backlit shots, combined with TEM images, allow us to pinpoint the location where the nanotube is at $T_{\max}$ to an accuracy of ~ 40 nm. Pairwise optimization of the scale, offset, and rotation between the "nanolamp only", "nanolamp with backlight", "backlight only", "low magnification TEM", and "high magnification TEM" images gives the overall transformation parameters to map the optical data onto the high magnification image. Results of such a mapping with the nanotube whose TEM image is shown in Fig. 3.7 and optical data in Fig. 5.1 are shown in Figure 5.3, with the nanotube's midpoint passing through the brightest pixel.

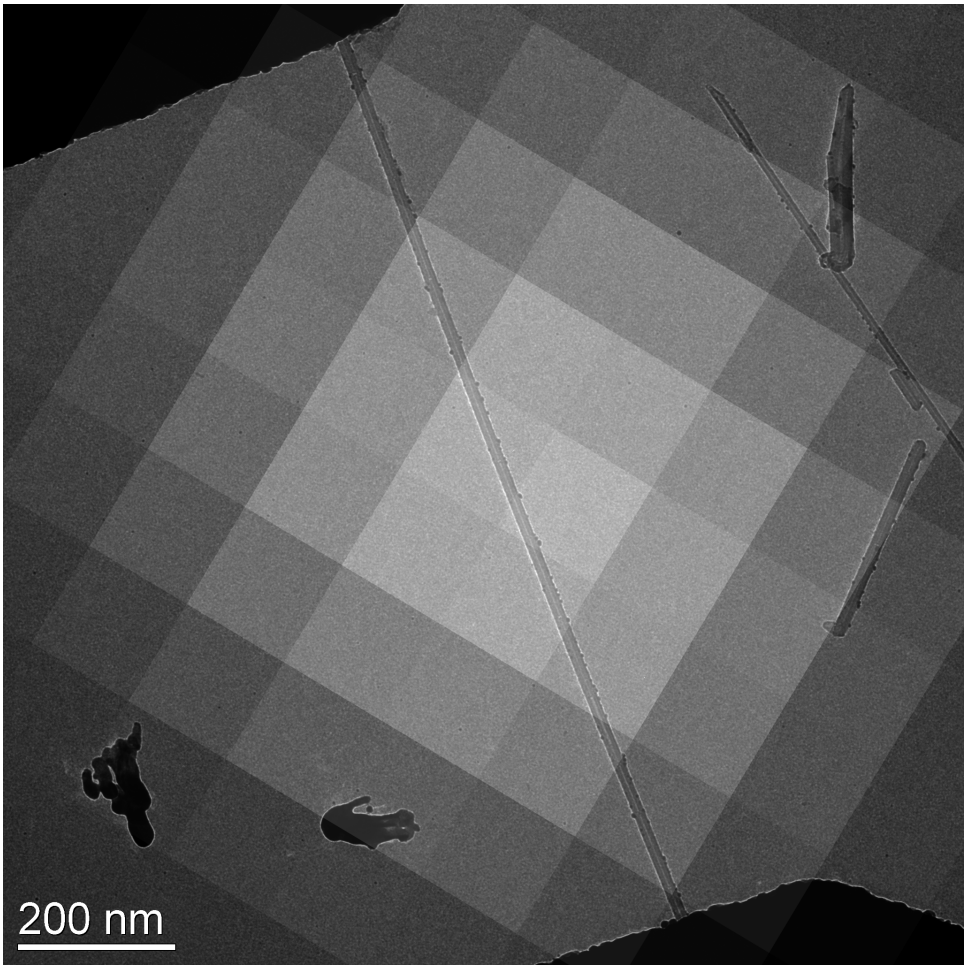

Figure 5.3: Merge of optical data in Fig. 5.1 and high magnification TEM image of Fig. 3.7. The actual CNT midpoint is indicated, as well as the midpoint as determined by the gaussian fit.

Figure 5.4: Portion of image showing parallel and perpendicular polarizations captured simultaneously.

5.1.3 Polarized Spot

As the majority of the image shown in Fig. 5.1 contains no information aside from background noise, the images belonging to the two orthogonal polarizations can be captured in a single exposure without overlap. Such an exposure with the majority of background cut out is shown in Fig. 5.4. The two polarizations seen are defined relative to the Wollaston prism's orientation, and care must be taken in identifying this orientation with the nanotube axis.

5.1.4 Diffraction Grating Profile

With both the diffraction grating and wollaston prism installed, a single exposure yields spectral data for both polarizations. We orient the grating's axis orthogonal to the polarizer's splitting direction, resulting in data such as in Fig. 5.5. The separation of the 1st maxima of both polarizations changes as a function of wavelength and corresponds to the expected separation plotted in Fig. 4.11. The peak data is extracted by taking slices perpendicular to the diffraction grating direction and fitting to a gaussian; the gaussian peaks give $S^p(0,0)$ as a function of wavelength and are plotted in Fig. 5.6. The parallel polarization's distribution peaks redder than the perpendicular distribution, but both distributions are smooth. Thus, we confirm that narrow band molecular transition peaks are absent in MWCNT emission.

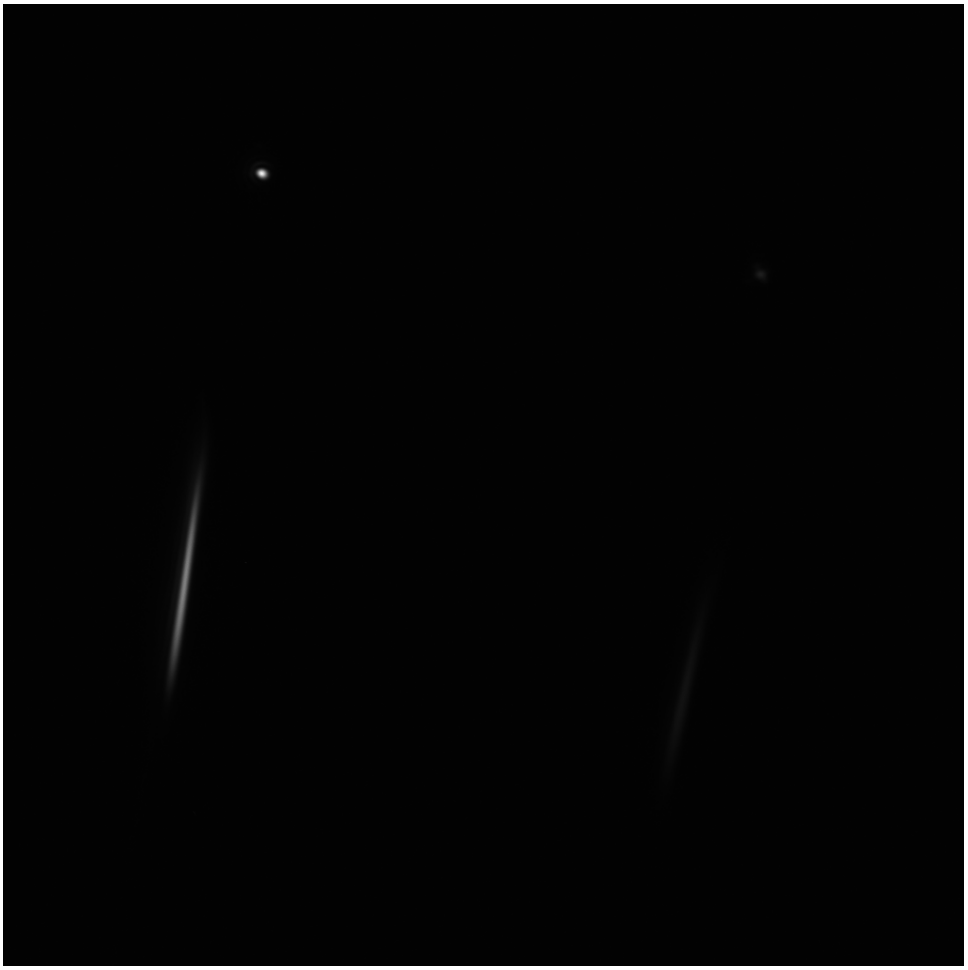

Figure 5.5: Image taken of nanolamp using wollaston polarizer and diffraction grating, showing 0th maxima and 1st maxima for each polarization.

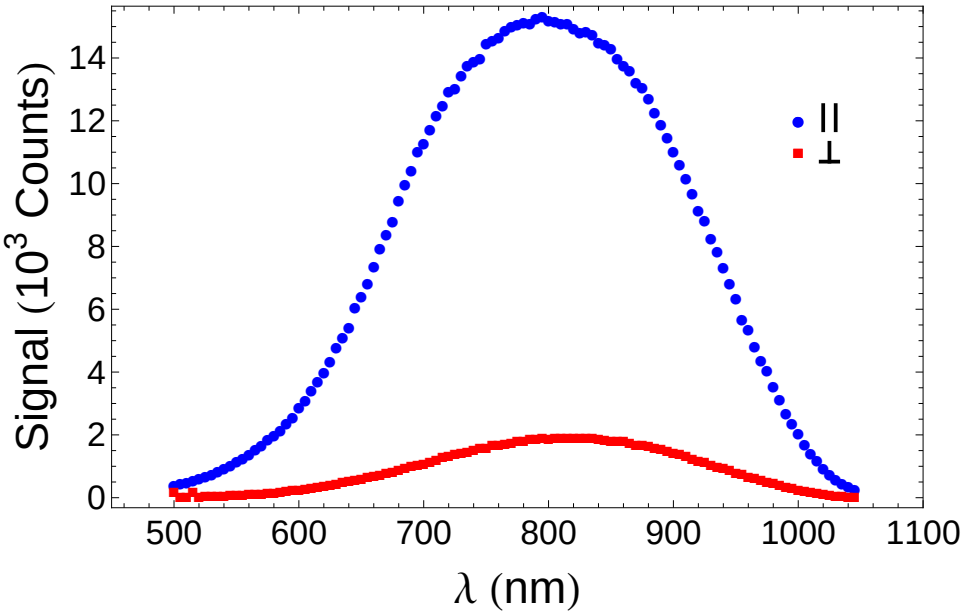

Figure 5.6: Plot of the peak counts in the first diffracted maxima as a function of wavelength. Cuts are taken every 5 nm.

5.2 Degree of Nanotube Polarization

Polarization-dependent absorption, emission, or reflection has been reported from macroscopic carbon nanotube aggregates such as films,[52, 53] fibers,[54] bundles,[55] and arrays.[56, 57] Individual SWCNTs have shown polarization dependent emission,[58, 59, 60, 61] scattering,[62, 63, 64] and absorption,[59, 65] peaking for the parallel (perpendicular) polarization at intraband (interband) transition energies. On the other hand, MWCNTs are in the classical limit; yet broadband, highly polarization-dependent emission is predicted by the Mie theory[66] or Rytov formalism[67] for cylinders, with this dependence increasing as the ratio r/λ decreases. We measure the degree of polarization (DoP) of the light emitted by a MWCNT nanofilament, a quantity which is independent of our setup and thus provides a useful measure of the accuracy of our Mie model.

5.2.1 Theory

We define the DoP for a MWCNT by

$$\mathrm{DoP} \equiv \frac{\dot{N}^{||} - \dot{N}^{\perp}}{\dot{N}^{||} + \dot{N}^{\perp}} = \frac{\dot{S}^{||}(0,0) - \dot{S}^{\perp}(0,0)}{\dot{S}^{||}(0,0) + \dot{S}^{\perp}(0,0)}, \tag{5.1}$$

which takes on values between 1 (completely polarized along the tube axis) and -1 (completely polarized perpendicular to the tube axis). Upon substitution of Eqs. 4.14, the explicit wavelength and temperature dependences of the Planck distribution and calibration factors cancel, leaving an expression that depends only on the integrated emission efficiencies,

$$\mathrm{DoP} = \frac{Q^{||}_{\mathrm{NA}} - Q^{\perp}_{\mathrm{NA}}}{Q^{||}_{\mathrm{NA}} + Q^{\perp}_{\mathrm{NA}}}. \tag{5.2}$$

Utilizing the Mie model developed in Sec. 2.3, the DoP is a quantity with a spectrum determined by the geometry and conductivity of the MWCNTs. We substitute the integrated emission efficiencies of Eq. 4.5 to find

$$\mathrm{DoP} = \frac{.896(\sigma Z_0)^4(\beta+\alpha)^2 + 3.584(\sigma Z_0)^2\beta^2(\beta^2+\alpha^2) - 14.336\beta^4(\beta^2-\alpha^2)}{.896(\sigma Z_0)^4(\beta+\alpha)^2 + 11.224(\sigma Z_0)^2\beta^2(\beta^2+\alpha^2) + 46.784\beta^4(\beta^2-\alpha^2)}. \tag{5.3}$$

Again taking the sheet conductivity to be the theoretical conductivity of graphene, $\sigma = \sigma_g$,

the degree of polarization becomes

$$\mathrm{DoP}(\lambda, T) = \frac{\lambda^4(b+a)^2 \tanh^4\left(\frac{C_2}{4\lambda T}\right) + A_1\lambda^2 b^2(b^2+a^2)\tanh^2\left(\frac{C_2}{4\lambda T}\right) - A_2 b^4(b^2-a^2)}{\lambda^4(b+a)^2 \tanh^4\left(\frac{C_2}{4\lambda T}\right) + A_3\lambda^2 b^2(b^2+a^2)\tanh^2\left(\frac{C_2}{4\lambda T}\right) - A_4 b^4(b^2-a^2)}, \tag{5.4}$$

with the coefficients $A_1 = 3.002 \times 10^5$, $A_2 = 9.018 \times 10^{10}$, $A_3 = 9.405 \times 10^5$, and $A_4 = 2.943 \times 10^{11}$.

5.2.2 DoP Fitting

To measure the DoP, the nanotube axis must be determined relative to the rotation stage's internal coordinate. A rotation stack of images is recorded at each wavelength, rotating the Wollaston prism through its 360° range in 10° increments. The intensity of one of the two spots is tracked over these stacks, and the results for device A1321F are plotted radially in Fig. 5.7. The data have been normalized such that the minima are equal across wavelengths for display purposes.

We fit each polarization curve to the function $A\cos(\theta - \theta_0) + B$ where θ is the rotation of the Wollaston prism. The offset θ_0 varies by $\pm 1°$ across all wavelengths, and coincides with the nanotube axis determined by the gaussian fit and transformed to prism coordinates, shown as a black line in Fig. 5.7. At θ_0, the DoP is a maximum, which can be expressed in terms of the fit parameters A and B by

$$\mathrm{DoP} = \frac{(A+B) - B}{(A+B) + B} = \frac{A}{A+2B}. \tag{5.5}$$

We fix the rotation stage at θ_0 to maximize the DoP and proceed to measure the polarization over a range of powers.

The DoPs as a function of wavelength for several tubes at their highest operating powers are shown in Fig. 5.8. The average DoP across all tubes is around 75%, indicating that MWCNTs are indeed quite polarized. For device A1001F, data taken at a significantly lower power are also displayed. The solid and open curves correspond to applied powers of 451 and 362 μW, respectively, from which it is evident that the radiation is more polarized at the lower temperature. This polarization increase with decreasing temperature becomes more

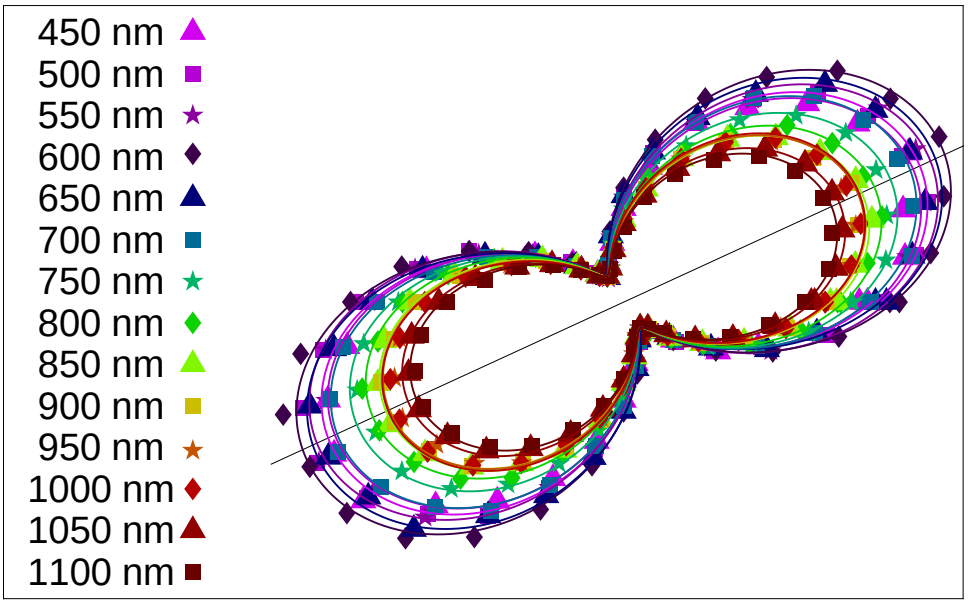

Figure 5.7: Radial plots of the nanotube's maximum intensity as a function of polarizer orientation θ at each of the filter wavelengths. Solid curves are fits to the function $A\cos(\theta+\theta_0)+B$. The black line represents the orientation of the nanotube as determined by comparing optical and TEM images.

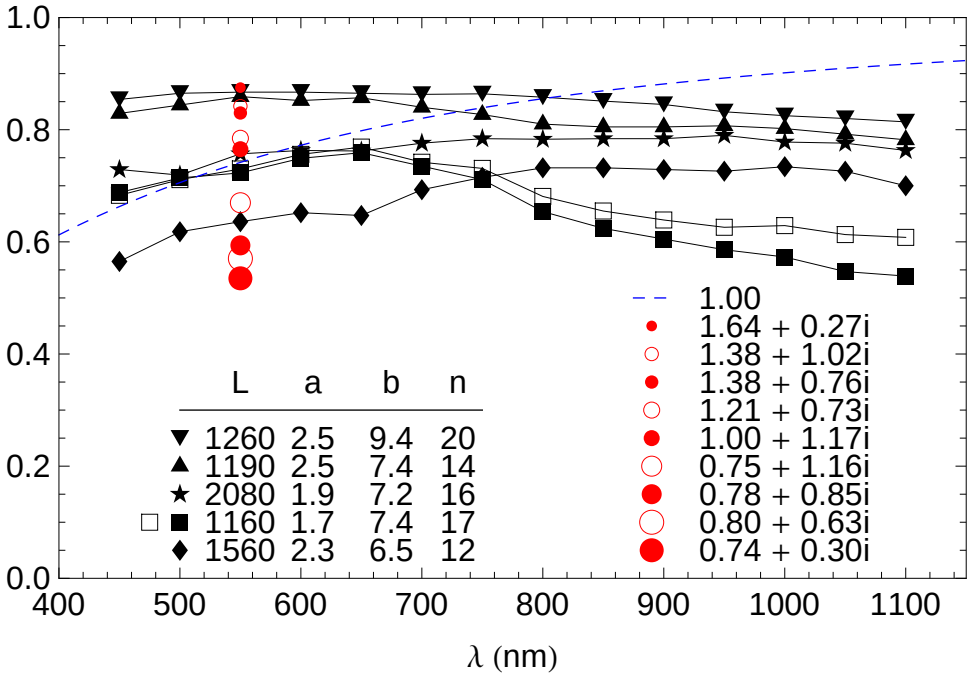

Figure 5.8: The maximum degree of polarization plotted as a function of wavelength for 5 nanotube devices. The curves with closed (open) squares was acquired from one device at input powers of 451 (362) μW. The dashed blue curve is the theoretical DoP expected for a tube with graphene's conductivity σ_g and the geometry of the 1190 nm long device. The red circles are the theoretical DoP for a tube with the same geometry but values for the conductivity of graphene given at $\lambda = 550$ nm as summarized in Ref. [2].

drastic at higher wavelengths, the DoP ranging from being only 0.5% higher at $\lambda = 450$ nm to 7% higher at $\lambda = 1100$ nm. This effect is larger than that predicted by the temperature dependence of σ_g.

The theoretical DoP as predicted by Eq. 5.3 with $\sigma = \sigma_g$ is also shown in Fig. 5.8 as a blue, dashed curve. Upon initial inspection, while the average DoP agrees with the experimental data, the values do not agree very well outside of small wavelengths for a couple of devices. However, the exact value of σ_g ranges in the literature, and the DoP at $\lambda = 550$ nm as predicted by the differing σ_g values summarized in Ref. [2]. The conductivity of multilayered graphene is uncertain up to a factor of two, which can account for the entire quantitative range of values seen from our devices.

The predicted DoP also is monotonically increasing, a feature that the DoPs of our nanotube devices do not share. Our measured DoPs tend to decrease at long wavelengths, behavior that, while not universal, is seen in a majority of devices. We attribute such behavior to the excitation of optical phonons at high temperatures, which have much shorter wavelengths and thus are more likely to produce unpolarized light than scattering of acoustic phonons[40], and will consider the origins of this effect when the discussion turns to graphene emission. Yet while the subtleties of the spectrum are not predicted by the Mie theory of our nanotubes, the magnitude of the polarization is indeed predicted by the experimental optical conductivity of graphene to within a factor of 2. Multiwalled carbon nanotubes thus produce highly polarized light on the order of $\sim 75\%$ on average, large compared to the typical unpolarized blackbody.

5.3 Pyrometry of Nanofilament

5.3.1 Single Color Pyrometry

With the Mie theory predicting the emission efficiencies of our nanotubes to a factor of 2, the temperature of the nanolamps can be determined from Eq. 4.14. Since the geometry of the nanotube and the transmission of the optics are completely determined, the only free parameter in Eq. 4.14 is T. For each nanotube, images are collected over a range of applied powers P at the wavelengths accessible using our small-bandpass filters. With the addition of the Wollaston prism, the light intensity is measured as a function of polarization p as well. Numerically solving Eq. 4.14 at each pixel (i, j) results in an array of temperatures $T_{\max}(i, j, \lambda, P, p)$.

Our nanotubes radiate in the steady-state during each exposure, with the applied power fluctuating $< 0.1\%$ across images taken at the same bias. It is thus reasonable to combine the values of $T_{\max}$ across pixels, polarizations, and wavelengths to obtain the maximum temperature each nanotube reaches given an applied power, $T_{\max}(P)$.

In particular, in a single image, each pixel (i, j) individually represents a measurement of the same light emission. The corresponding values $T_{\max}(i, j)$ are shown on one such image

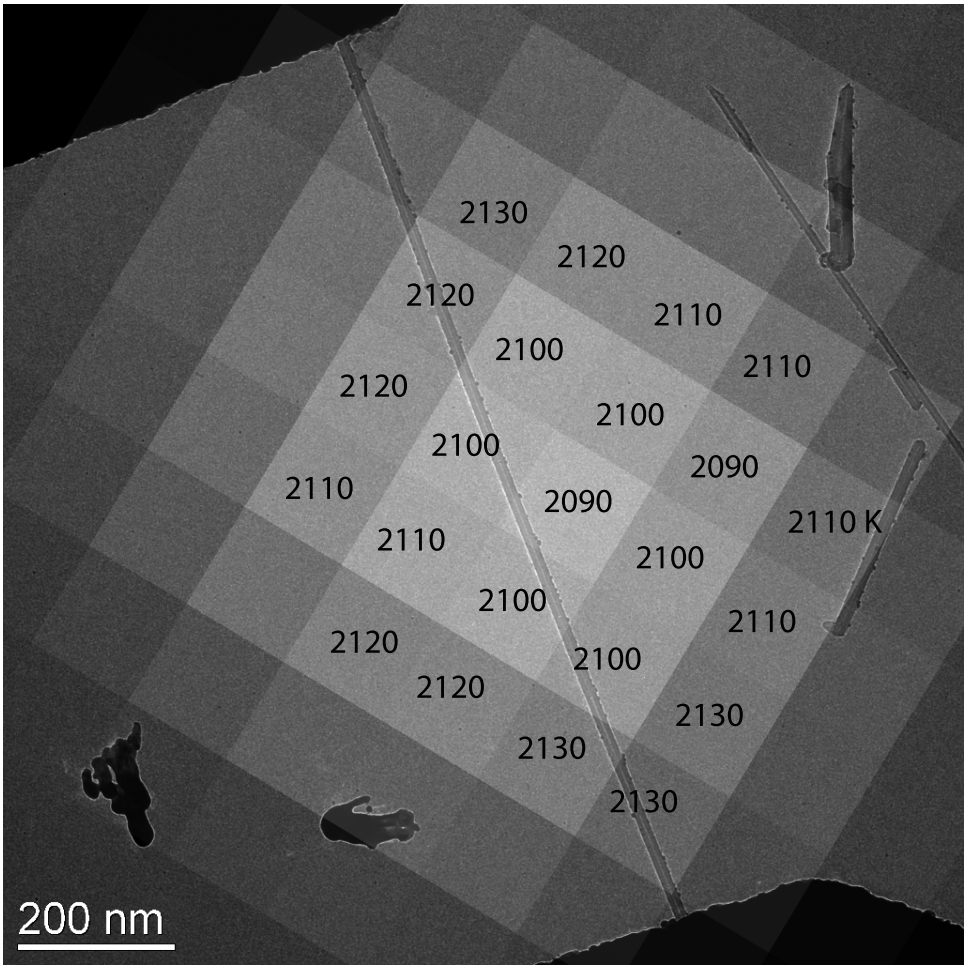

Figure 5.9: Pixel-by-pixel temperature analysis of Fig. 5.3. Each pixel (i, j) is labeled with the nanotube's central temperature $T_{\max}(i, j)$ as determined from that pixel.

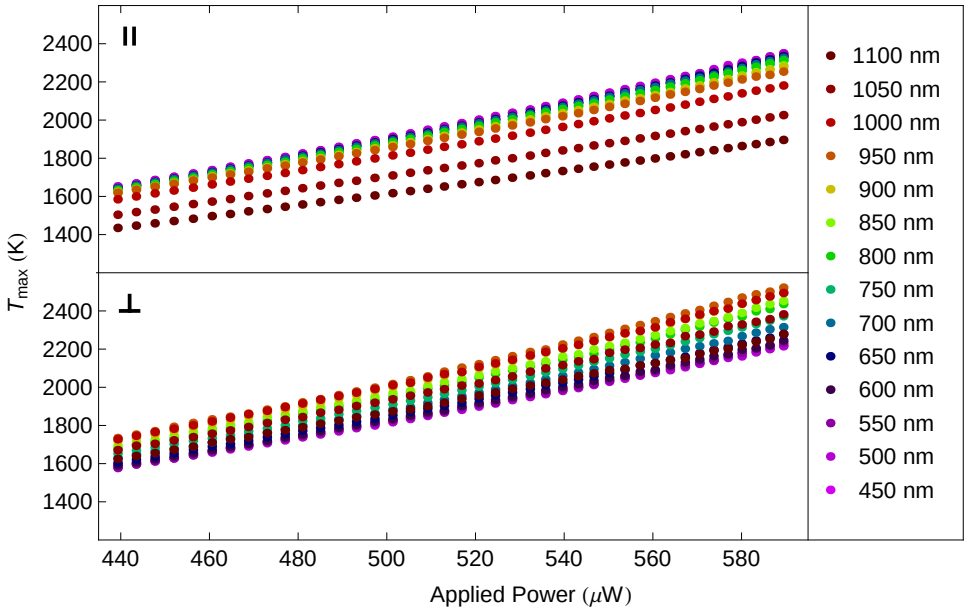

Figure 5.10: $T_{\max}(\lambda, P, p)$ graphed as a function of applied power P for each wavelength λ and polarization p.

in Fig. 5.9. Since all other factors are equal, the relative weight of each pixel's value of $T_{\max}$ arises solely from the intensity of that pixel. Given a shot noise error of $\sigma_{ij} = \sqrt{S_{ij}}$, the associated weight is $w_{ij} = 1/S_{ij}$. The signal drops off from the nanotube center according to Φ_{ij}; within a radius of $\lambda/2$ this decrease corresponds to a factor of 4-10. Within a square of size λ, $T_{\max}(\lambda, P, p)$ varies on the order of $\sim 1\%$, as can be seen in Fig. 5.9, and the weighted average gives $T_{\max}(\lambda, P, p)$ for each exposure.

With the proper weighting, we also combine $T_{\max}(\lambda, P, p)$ values across wavelengths for a device operated at constant power. One device's temperatures $T_{\max}(\lambda, P, p)$ are plotted as a function of P for each λ in Fig. 5.10. For every wavelength, $T_{\max}$ is linear in P, self-consistently supporting the assumption made in approximating the temperature profile as a quadratic. In fact, most of the curves represent temperatures within a range of ~ 200 K, with the exception of the longest wavelengths. For $\lambda > 1000$ nm, the lower temperatures represent that the signal is lower than expected for our model. The parallel polarization should show essentially a graybody distribution, and such an infrared cutoff has been observed for

macroscopic fibers comprised of CNTs as well[68].

Because the Planck factor dominates over the other $T_{\max}$ dependent quantities–the eccentricity and the gaussian factor–the error in $T_{\max}$ is

$$\sigma_{T_{\max}} = \frac{T_{\max}^2 \lambda}{C_2} \sqrt{1/S_{ij} + \left(\frac{\sigma_\Theta}{\Theta}\right)^2 + \left(\frac{\sigma_Q}{Q}\right)^2 + 5\left(\frac{\sigma_\lambda}{\lambda}\right)^2}. \tag{5.6}$$

Because we determine the exposure times such that the maximum counts are on the order of $2-3\times10^4$ counts, $\sigma_\lambda/\lambda \sim .001$. We take $\sigma_\Theta/\Theta \approx .1$, constant with respect to wavelength, as is the error inherent in the emissivity model σ_Q. This assumption results in $\sigma_{T_{\max}} \sim \lambda$–reflecting that the largest errors occur at the longest wavelengths–and allows us to weight $T_{\max}$ across wavelengths by $w_\lambda = \lambda^{-2}$. The weighted averages are shown for both polarizations of six nanolamp devices in Fig. 5.11. The weighted standard deviations are about ~ 100 K, which we take as the error in $T_{\max}(P,p)$. Across the devices studied, the values of $\Delta T_{\max}^p(P) = |T_{\max}(P,||) - T_{\max}(P,\perp)$ have an mean of ~ 70 K, with a maximum discrepancy of 160 K, consistent with an error of 100 K.

Because polarization data is taken during a single exposure, we expect $\Delta T_{\max}^p = 0$. The discrepancy between the temperatures between the two polarizations can be reduced to 0 by treating the conductivity as a free parameter as well instead of assuming $\sigma = \sigma_g$. The dependence of the emission coefficients on the conductivity approximately follow

$$\begin{aligned} Q^{|}|(\sigma) &\approx n\pi\sigma Z_0 \sim \sigma \\ Q^{\perp}(\sigma) &\approx \frac{16\pi^3 n\delta^2}{\sigma Z_0 \lambda^2} \sim \frac{1}{\sigma}; \end{aligned} \tag{5.7}$$

thus the emission coefficients have opposite behavior with adjustments to σ. Keeping the total emission rate constant, an increase in emissivity corresponds to a decrease in temperature, and vice versa; as such, we find σ such that $\Delta T_{\max}^p$ reduces to 0.

The adjustment is performed by setting the weighted temperatures equal to each other, which takes the form of the equation

$$\sum_\lambda \frac{1}{\lambda^2}\left(\frac{1}{\log\Gamma^{||}(\lambda) + \log Q^{||}(\sigma)} - \frac{1}{\log\Gamma^{\perp}(\lambda) + \log Q^{\perp}(\sigma)}\right) = 0, \tag{5.8}$$

where $\Gamma^p(\lambda)$ represents the collection of all quantities other than the efficiency in Eq. 4.14. This equation is solved numerically for σ; the values of σ in units of σ_g for the six nanotube

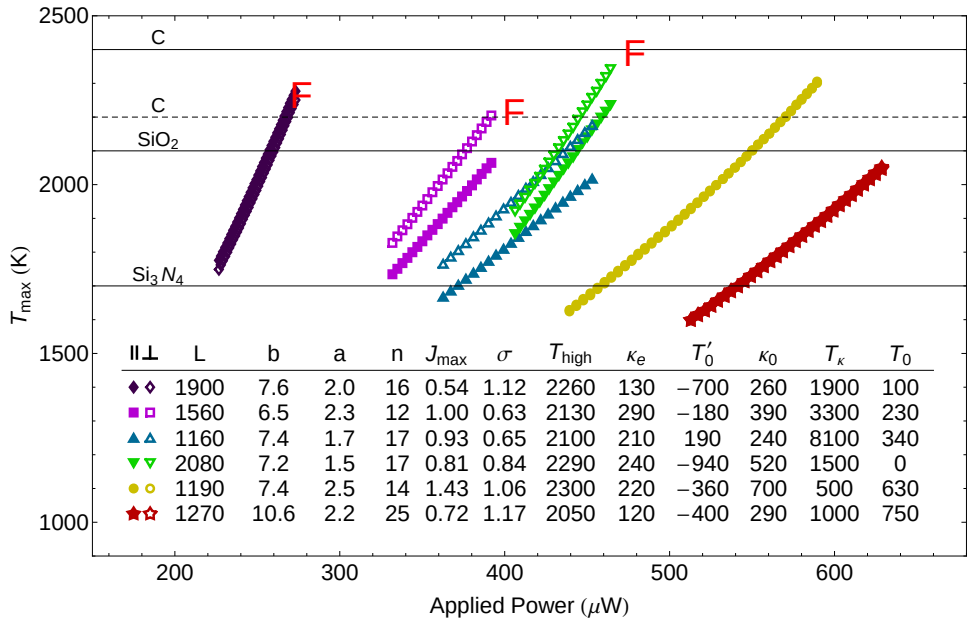

Figure 5.11: $T_{\max}(P,p)$ shown for six devices. The legend lists each device's length and radii in nm; number of walls; maximum current density reached in μA/nm^2; optical conductivity in units of σ_g; highest temperature reached in K; effective thermal conductivity in W/K·m and extrapolated room temperature in K from fitting to Eq. 2.10; and room-temperature thermal conductivity W/K·m, thermal conductivity temperature coefficient in K, and extrapolated room temperature in K from fitting to Eq. 2.22. Solid horizontal lines indicate temperatures where the evaporation rates of graphite, SiO_2, and Si_3N_4 equal 1 nm/s. The dashed line indicates the temperature where the evaporation rate of graphite equals 1 monolayer/s = .34 nm/s.

devices is shown in the table of Fig. 5.11. Therefore, the equivalent conductivities of our nanotubes vary from the theoretical value by no more than $\sim 40\%$, consistent with our assessment from the DoP analysis that $Q(\sigma = \sigma_g)$ is accurate to within a factor of 2.

With this adjustment to σ, we obtain $T_{\max}(P)$ for our nanolamps. The plots of temperature as a function of power in Fig. 5.11 are mostly linear, but display a slight curvature. We fit $T_{\max}(P)$ to Eq. 2.10 with free parameters κ_e and T_0', and to 2.22 with free parameters κ_0, T_κ, and T_0; the fit values are summarized in the table of Fig. 5.11. The room temperatures extracted from the linear fit T_0' are highly negative, indicating that this fit cannot be extrapolated to zero power. Because at low power the contacts dissipate the majority of the power, such a consequence is to be expected. However, the room temperatures from the Umklapp fit T_0 average ~ 340 K, close to actual room temperature. Therefore, the exponential fit of $T_{\max}(P)$ is superior to the linear fit, and we expect the values it returns to propagate to the low temperature limit in a well-defined way.

The room temperature thermal conductivities κ_0 range from $240 - 700 \pm 10$ W/K·m; these values are consistent with other thermal conductivity measurements ranging between $50 - 600$ W/K·m [39, 41, 8]. For the given values of T_κ, we find that $\kappa_0/\kappa(T_{\max} = 2000 \text{ K}) \sim 2$. The κ_e values from the linear fit represent an effective thermal conductivity at high temperature, and the range from $120 - 290 \pm 10$ W/K·m is consistent with the parameters from the Umklapp scattering model. Therefore, modeling the radiating nanotube as an infinite Mie cylinder allows us to measure not only the temperature of the nanotubes, but the optical and thermal conductivities as well.

5.3.2 Comparison to Multicolor Pyrometry

Our single-color pyrometry technique can determine a nanotube's temperature to an accuracy of $\sim 5\%$, yet it is instructive to compare results to the multiwavelength techniques often used to analyze carbon nanotubes. In these analyses, the total emission of photons from an individual CNT,[69, 47] bundle,[55, 70] or film[71, 72, 73, 74, 75, 76] is captured with a photodiode or similar detector, and a graybody fit is peformed to the intensity spectrum.

By integrating Eq. 2.30 over solid angle or Eq. 4.14 over the CCD, the total rate of

Nanotube	Single-λ $T_{\max}(\|\|)$	Single-λ $T_{\max}(\perp)$	Multi-λ $T_{\max}(\|\|)$	Multi-λ $T_{\max}(\perp)$
A1001C	2020	2180	2690	2360
A1003H	2240	2240	2950	2980
A1008I	2060	2200	2550	2680
A1308G	2050	2050	2510	2340
A1321F	2280	2250	2800	2560
A1321J	2300	2310	2800	2530

Table 5.1: Comparison of the temperatures determined for both polarizations using the single-color method and $\sigma = \sigma_g$ and using the multi-color method treating the nanotube as a graybody.

photons emitted into the NA is

$$\dot{N}(\lambda, P, p) = Q^p_{\mathrm{NA}} \frac{2bc\Delta\lambda}{\lambda^3} \frac{L}{\lambda} \sqrt{\frac{\lambda T_{\max}}{C_2} \frac{\pi T_{\max}}{4(T_{\max} - T_0)}} e^{-C2/\lambda T_{\max}}. \tag{5.9}$$

The emission rate $\dot{N}$ is measured by summing over every pixel and taking the transmission into account:

$$\dot{N}(\lambda, P, p) = \frac{\sum_{ij} \dot{S}_{ij}}{\Theta_\lambda}. \tag{5.10}$$

These values of $\dot{N}$ are then fit to Eq. 5.9 with Q^p_{NA} and $T_{\max}$ as free parameters; by assuming no explicit wavelength dependence for the efficiency, we are treating the CNT as a graybody.

Performing the multiwavelength fit to the 7 nanotubes gives emission coefficients an order of magnitude smaller than those predicted by Mie theory and temperatures roughly 300-700 K larger than from the single-color method; these results are summarized in Tables 5.1 and 5.2. Furthermore, whereas the polarization difference $\Delta T^p_{\max}$ has a mean 70 K for single-color with a standard deviation of 70 K and a maximum of 160 K, the multicolor fit shows an average differnece of 190 K with standard deviation 110 K and maximum of 330 K. Therefore, our single-color method shows more consistency within the data than the multicolor fit does.

Nanotube	Single-λ $Q^{\parallel}$	Single-λ $Q^{\perp}(0)$	Multi-λ $Q^{\parallel}(0)$	Multi-λ $Q^{\perp}(0)$
A1001C	1.208	0.165	.045	.029
A1003H	1.204	0.162	.060	.008
A1008I	0.885	0.142	.078	.010
A1308G	1.769	0.238	.149	.027
A1321F	1.178	0.168	.117	.023
A1321J	1.038	0.162	.111	.029

Table 5.2: Comparison of the normal emission coefficient determined for both polarizations using the single-color method and $\sigma = \sigma_g$ and using the multi-color method treating the nanotube as a graybody. The values for the single-color method perpendicular emission have been evaluated at $\lambda = 500$ nm.

5.3.3 Evaporation of Membrane

While the single-color method is more consistent internally than the multi-color method, we must turn to more physical benchmarks to determine the relative accuracy of these approaches. Our nanotubes in general sit atop a membrane comprised of SiO_2 and Si_3N_4, which begins to disintegrate at increasing distance from the center of the tube as the temperature increases, as seen in Fig. 3.9. This disintegration takes place on the order of seconds to a minute.

The mass loss of a solid as a function of temperature is given by

$$\frac{\Delta z}{\Delta t} = \frac{\alpha P_g}{\rho}\sqrt{\frac{m}{2\pi RT}}, \tag{5.11}$$

where z is the thickness of the solid, α is the activity, ρ the density, P_g the vapor pressure of the gas phase, m the molar mass of the gas phase, and $R = k_B N_A$ is the molar gas constant. Empirically, the logarithm of the vapor pressure is linear in $1/T$, or $P_g = 10^5 \exp[-(A + B/T)]$ Pa for constants A, B; for Si_3N_4, $A = 20.45$ and $B = 4.58 \times 10^4$ K.[77] With the activity as $\alpha = 4.3 \times 10^{-5}$,[77] a Si_3N_4 membrane in vacuum at a temperature of ~ 1700 K will lose 1 nm/s. A similar analysis for SiO_2 using data from Ref. [78] gives the corresponding 1 nm/s loss temperature of 2100 K.

Our membranes have a thickness on the order of 10-20 nm, and the membranes disinte-

grate in $\lesssim 1$ minute, so these temperatures give a reasonable lower bound and benchmark for $T_{\max}$. The biases at which this disintegration begins is usually 0.1-0.2 V below the highest bias applied to a nanotube. The temperature analyses give $\Delta T/\Delta V \sim 175$ K/.1 V, indicating that the best estimates of the maximum nanotube temperature based on the nitride and oxide evaporation lie between 2000 and 2300 K, consistent with our single-color analysis, but not with the multi-color analysis.

5.3.4 Nanotube Failure

A similar analysis to the membrane evaporation can be performed on the failure points of the nanotubes using graphite as a model. For graphite, the activity is $\alpha = 1$, $A = 18.3$, and $B = 8.723 \times 10^4$ K.[79] The loss of 1 nm/s occurs at 2400 K, and a monolayer will evaporate every second (.34 nm/s) at 2200 K. Of the nanotubes studied above, only 3 failed during biasing: A1003H, A1008I, and A1321F; the others failed due to ESD, TEM electron damage, or other external stimuli. Using the single-color model, the temperatures at which these nanotubes failed were 2390, 2210, and 2260 K, respectively, as opposed to the multi-color failure temperatures of 3100, 2700, and 2700 K, respectively. Because these nanotubes all failed within 5 power line cycles, the lower temperatures specified by the single-color analysis are much more reasonable with a failure mode of carbon evaporation.

CHAPTER 6

Pyrometry of Graphene

6.1 Graphene versus CNTs

Having characterized the MWCNT temperature, emission, polarization, and optical and thermal conductivites with single-color pyrometry, we apply similar techniques to its parent allotrope, graphene. Compared to CNTs, graphene sheets can be fabricated in the classical thermodynamic limit, with area dimensions $\gg \lambda$. It is expected to behave as a classical graybody, having a theoretical optical conductivity independent of wavelength in the visible and NIR. The thermal emission of graphene has been studied at low temperature and in the infrared[17, 19, 20, 21], yet our technique enables us to study graphene at extreme temperatures throughout the visible-NIR.

6.2 Graphene Nanosheet Characterization

6.2.1 Fabrication of Graphene Filaments

To make incandescent graphene sheets, graphene is first produced from graphite flakes by the mechanical exfoliation method[16]. Then it is deposited onto silicon that has a layer of LPCVD grown 300 nm SiO_2. Single and few-layer graphene samples are idenfied on the oxide substrate by visual inspection, as can be seen in Fig. 6.1(a1) and (b1). A thin layer of PMMA is spun on top of the graphene and soft baked at 100° C. The graphene/PMMA film is lifted off of the substrate by immersion in a 1 M solution of NaOH, and subsequently cleaned in water.

are fabricated on the same chips used for the MWCNT devices, which have been processed through the optical lithography definition of contacts step.

The graphene is transferred to one of the previously described device chips, which has been processed through electrode deposition. The PMMA layer, acting as the handle for the graphene, is positioned over the chip while immersed in water in a probe station. The previously identified graphene is aligned to the electrodes by positioning the film with the probes; contact is made after alignment by applying downward force with the probes as the water evaporates. Finally, the PMMA is removed with acetone and isopropanol, resulting in the final graphene filament such as those visible in Fig. 6.1 (a2) and (a3). The length of the active sheet is defined by the electrode spacing, $L = 15$ μm. The graphene devices are electrically probed, with active devices having typical resistances of $\sim$ 1-15 kΩ. As with the MWCNT devices, we thin the membranes using HF vapor, perform a 300° C anneal, and subsequently image the devices in the TEM.

6.2.2 TEM Characterization of Graphene

Because graphene is only a few-to-one atoms thick, imaging the graphene directly on a substrate with bright field mode, as seen in Fig. 6.2(a), does not provide sufficient contrast to fully characterize the sheet's structure. Instead, we employ dark field imaging methods to characterize the graphene sheets. A diffraction image of a graphene device is shown in Fig. 6.2(b). The diffraction peaks correspond to the reciprocal vectors $\vec{G}(v_1, v_2) = v_1\vec{b}_1 + v_2\vec{b}_2$ for integers v_1 and v_2, and $\vec{b}_1$ and $\vec{b}_2$ given by Eq. 1.9. The smallest vector $\vec{G}$ has six-fold degeneracy, with v_1, $v_2 = 0, \pm 1$, which represent the three smallest reciprocal lattice points of the inner ring seen at radius $4\pi/\sqrt{3}a_g$.

The diffraction pattern in Fig. 6.2(b) has two independent sets of reciprocal vectors; thus this graphene device has two different grains, rotated an angle with respect to each other as the two diffraction patterns. By placing an aperture about one of the peaks, we select out only the electrons diffracted by the grain belonging to that peak when imaging. The two grains of this device are easily seen in Fig. 6.2(c) and (d) using this dark field method.

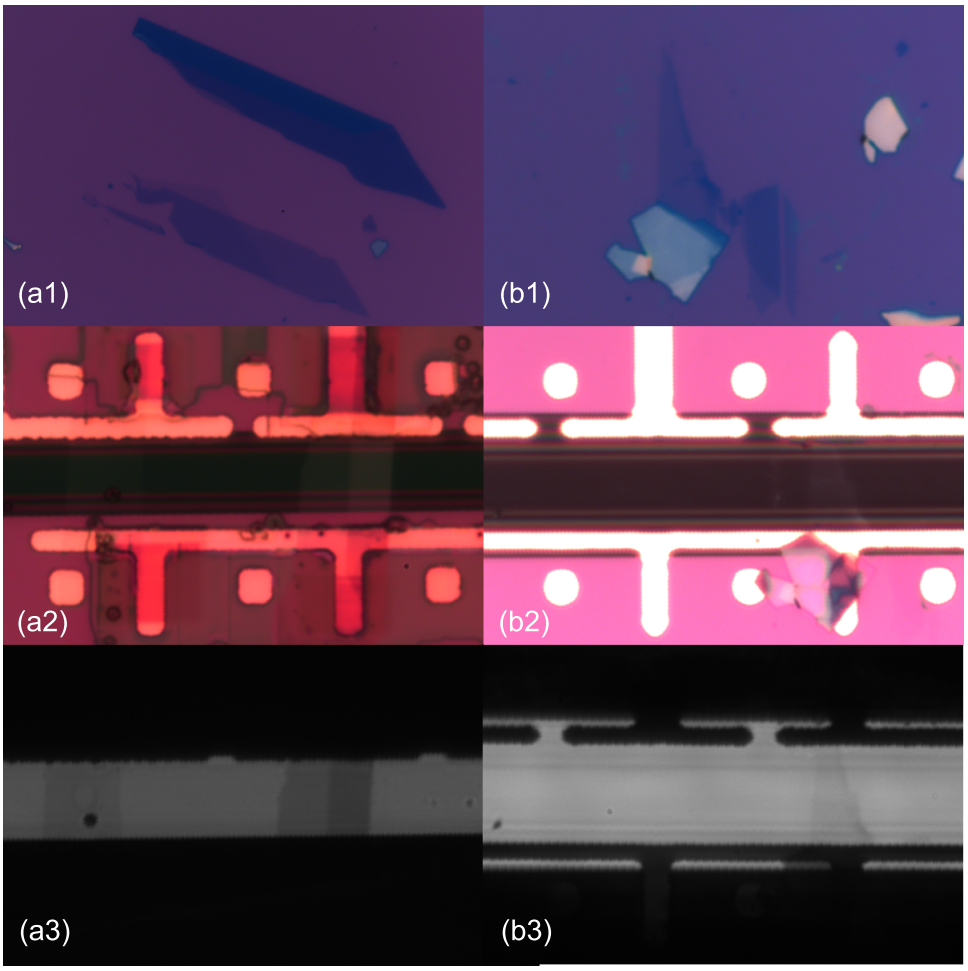

Figure 6.1: Optical images of graphene devices (a1-a3) N2 and (b1-b3) N6 throughout fabrication. (a1,b1) Graphene mechanically exfoliated onto 300 nm thick SiO_2 on Si; (a2,b2) graphene transferred to electrode devices; (a3,b3) backlit microscope images of same graphene sheets. Images courtesy of William Hubbard.

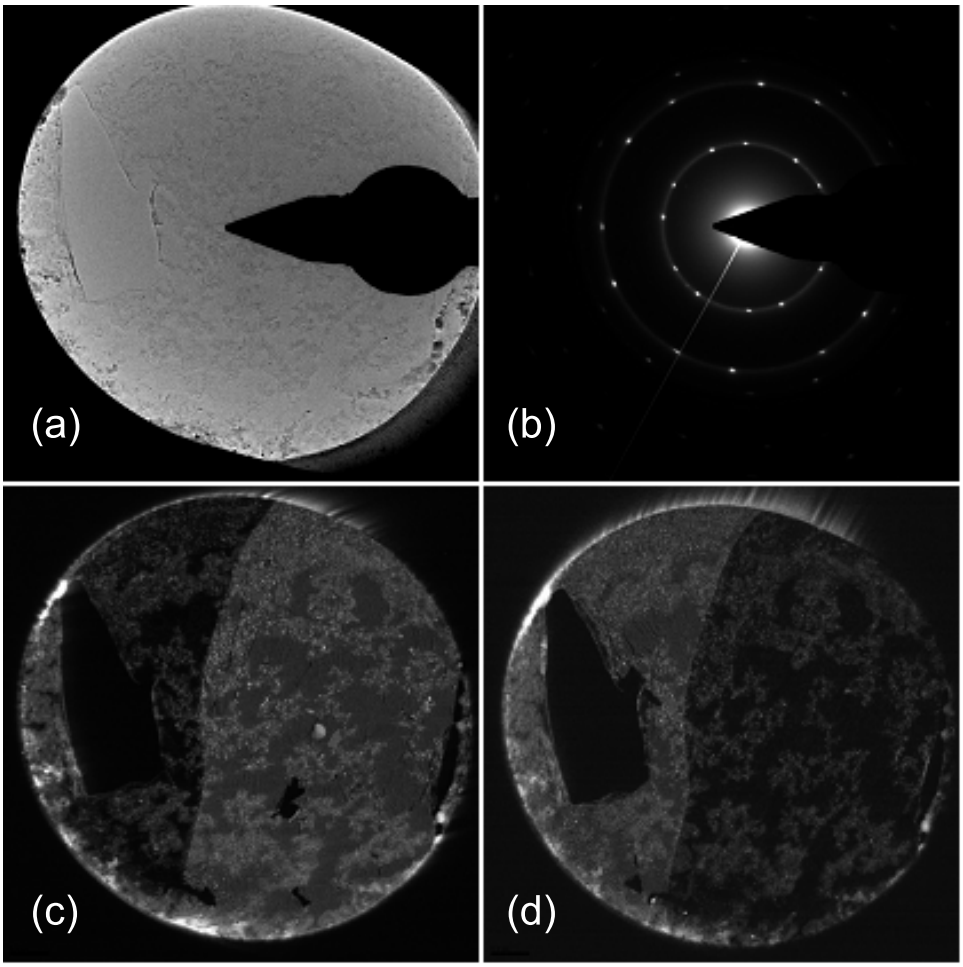

Figure 6.2: (a) Bright field TEM image of a graphene sheet (b) Diffraction pattern taken from the same device (c, d) Dark field images taken by selecting only electrons diffracted into the two independent peaks; the graphene grain corresponding to that peak appears bright in the image. Images courtesy of Brian Shevitzky.

6.3 Graphene Polarization

6.3.1 Polarization

We have observed large polarization effects in MWCNTs, owing to their geometric asymmetry; on the other hand, graphene has a highly symmetric geometry. For an infinite plane of graphene, symmetry indicates that we expect graphene to behave like a typical blackbody, emitting completely unpolarized light. However, the finite size of the graphene sheets we bring to incandescence applies an additional constraint on the electric field; here we consider the effects finite size might have on polarization.

The finite width of the graphene sheets imposes a Dirichlet boundary condition on the wavefunction, similar to the periodic boundary condition of SWCNTs. This restriction again divides the BZ into accessible subbands with splitting along the direction of the width $\hat{w}$. Incident light with "parallel" polarization ($\vec{E}$ along the sheet's length $\hat{l}$) will preferentially induce intrasubband transitions, and "perpendicular" polarization will induce intersubband transitions[80]. Therefore, for graphene nanoribbons (GNRs), whose widths are $\lesssim 1$ μm, we would expect to see strong polarization effects in the spectrum.

Our graphene sheets, however, are wide enough that the entire BZ is accessible, and the polarization dependence from allowed transitions disappears. Within the bulk of the sheet, we treat the problem of absorption as one of an infinitely thin conducting sheet, and referring to Appendix A find the absorption coefficients

$$\begin{aligned} A^s(\theta) &= \frac{4\cos\theta\sigma_{2D}Z}{(2\cos\theta+\sigma_{2D}Z)^2} \\ A^p(\theta) &= \frac{4\cos\theta\sigma_{2D}Z}{(2+\sigma_{2D}Z\cos\theta)^2} \end{aligned} \tag{6.1}$$

for electric field polarized along the plane and perpendicular to the plane, respectively. The absorption along a fixed direction on the sheet, which we designate as "parallel", is

$$A^{||}(\theta,\phi) = A^s(\theta)\cos\phi + A^p(\theta)\sin\phi. \tag{6.2}$$

Rotation by $\pi/2$ along ϕ gives the similar expression for the "perpendicular" absorption.

Since our optics integrate over all ϕ, the total absorption for both polarizations will be equal, and we expect to measure unpolarized light being emitted from the graphene.

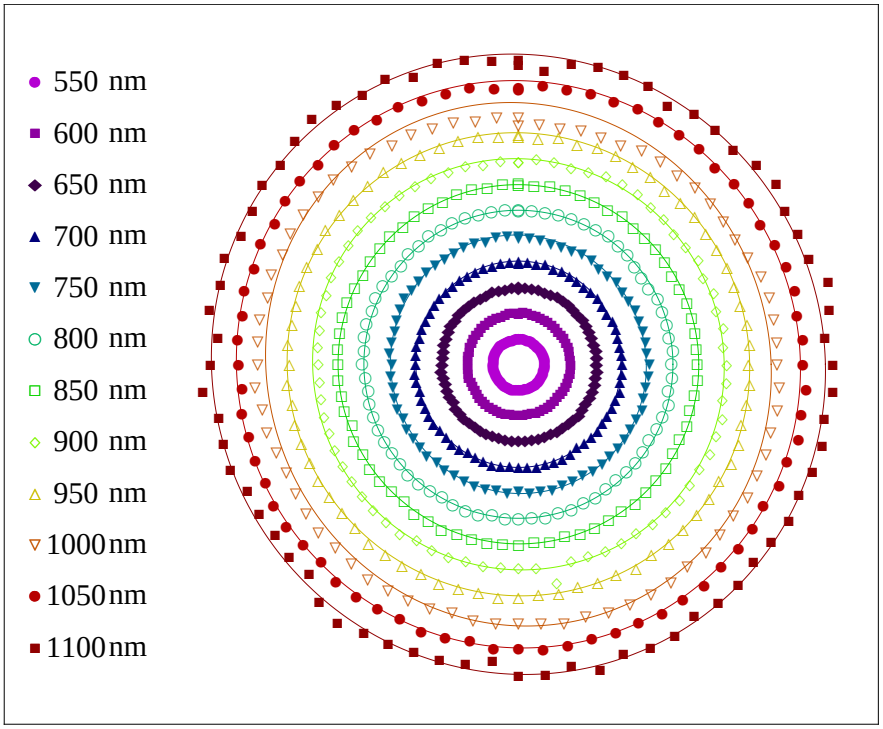

Figure 6.3: Polar plot of image intensity as a function of polarizer angle θ. No net polarization is observed, and fits are to the mean intensity.

We have measured the DoP as a function of wavelength for our sheets, shown in Fig. 6.3. The polarization is $\lesssim 1.0\%$ over the 360° range, consistent with the slight difference in transmission of the two halves of the Wollaston prism. Therefore, wide graphene sheets radiate unpolarized light, as expected for a classical blackbody.

6.3.2 Edge Polarization

The result that graphene should emit unpolarized light stems from the assumption that we can treat the sheet as infinite in extent. This assumption breaks down near the edge; in the absorption picture, diffraction must be considered in addition to reflection and transmission. The problem of diffraction of a plane wave obliquely incident on an infinitely thin resistive sheet has been considered,[81, 82, 83] and for a qualitative understanding we rewrite the expression of the diffracted field E_d for a H-polarized (our "perpendicular") plane wave

derived as Eq. 33 in [82],

$$E_d^{\perp}(r,\theta) \sim u\left[F(k,\theta)\frac{e^{-ikr}}{\sqrt{kr}} + G(k,\theta)e^{-ku|y|}e^{ik\sqrt{1+u^2}}\right], \qquad u \equiv \frac{c^2k}{2}\mu(\epsilon-1). \tag{6.3}$$

The first term represents the scattered cylindrical wave, and the second term is a surface wave; however, both are proportional to the quantity $\mu(\epsilon - 1)$.

For a non-magnetic resistive sheet, $\mu = 1$ and $\epsilon = 1 + i\sigma/\omega$, and $u = i\sigma Z_0/2$. By the duality property of electromagnetic waves, we can find the diffracted field for an E-polarized (our "parallel") plane wave by $E \to H$, $H \to E$, $\epsilon \leftrightarrow \mu$. From the definition of u, we see that in this case, $u \to 0$. Because both terms in Eq. 6.3 are proportional to 0, the diffraction term disappears in this case. Thus, we can write the absorption near the edge of graphene as

$$\begin{aligned} A_{\text{edge}}^{||} &= 1 - R_{\text{bulk}}^{||} - T_{\text{bulk}}^{||} = A_{\text{bulk}}^{||} \\ A_{\text{edge}}^{\perp} &= 1 - R_{\text{bulk}}^{\perp} - T_{\text{bulk}}^{\perp} - D_{\text{edge}}^{\perp} = A_{\text{bulk}}^{||} - D_{\text{edge}}^{\perp} \end{aligned} \tag{6.4}$$

where the diffraction coefficient in the far field

$$D^{\perp} = \frac{1}{2\pi}\int_0^{2\pi}\frac{1}{2}\text{Re}\left[F \cdot F^*\right] d\theta \tag{6.5}$$

will be non-zero. Therefore, the graphene sheet will be polarized along the length near its edge.

Figure 6.4 shows a map of the polarization along the graphene sheet. We record images over the 360° range of our polarizer in 5° intervals and pattern match to the graphene sheet. Extracting a region of interest (ROI) centered around the graphene at each angle allows us to fit the intensity of each pixel to $S_{ij} = A_{ij}\cos[2(\theta - \theta_0)] + B_{ij}$. We then find the degree of polarization at each pixel $DoP(i,j) = A_{ij}/(A_{ij} + 2B_{ij})$. While the center of the graphene sheet is indeed unpolarized, the edges exhibit polarizations as high as 18%. The maximum edge polarization as a function of wavelength is shown in Fig. 6.5.

However, we observe that the sheet is polarized about 5% along the sheet's width away from the bright spot; we expect the image to be unpolarized here as it is away from an edge. We attribute this anomalous effect to the fact that the temperature is changing rapidly over a length scale $\lesssim \lambda$ along the length, but not the width, leading to decreased parallel emission.

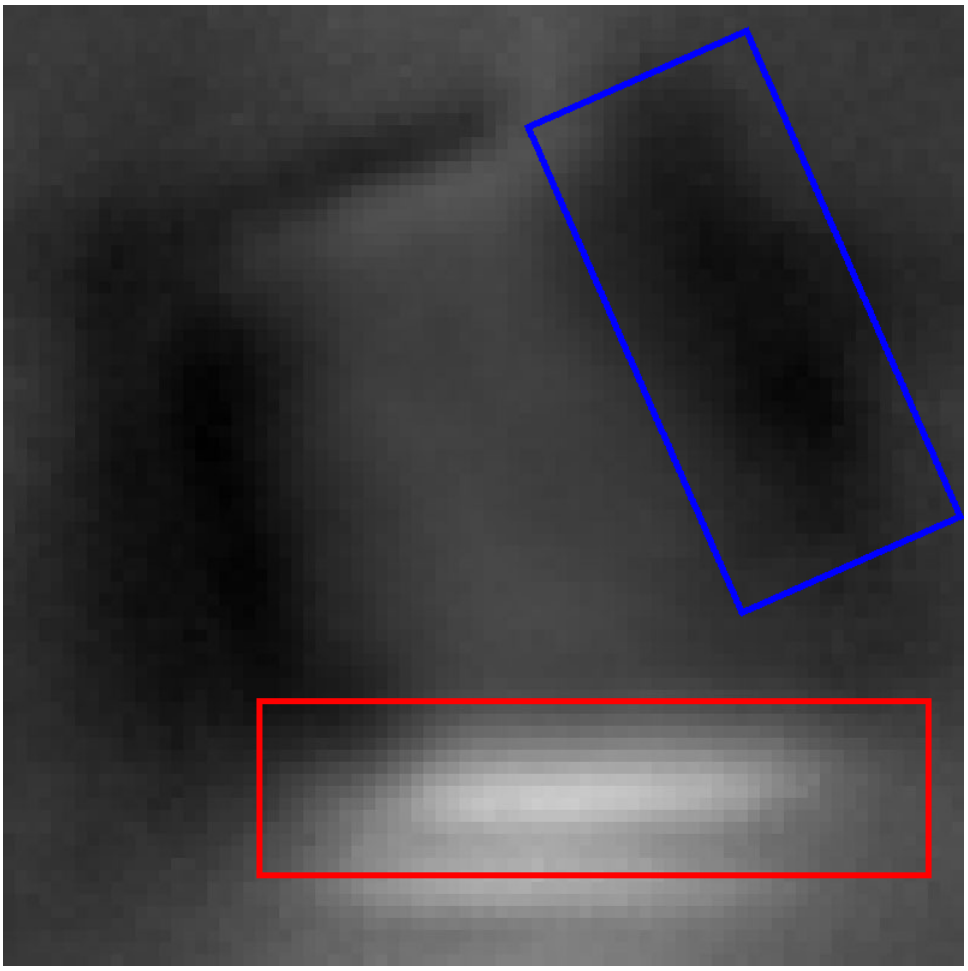

Figure 6.4: DoP map showing relative polarization from device N6 at every pixel in a 100×100 pixel^2 region of interest centered on the graphene sheet. The red ROI shows net polarization along the sheet length at the edge, whereas the blue ROI shows the net polarization along the sheet width away from the hot spot.

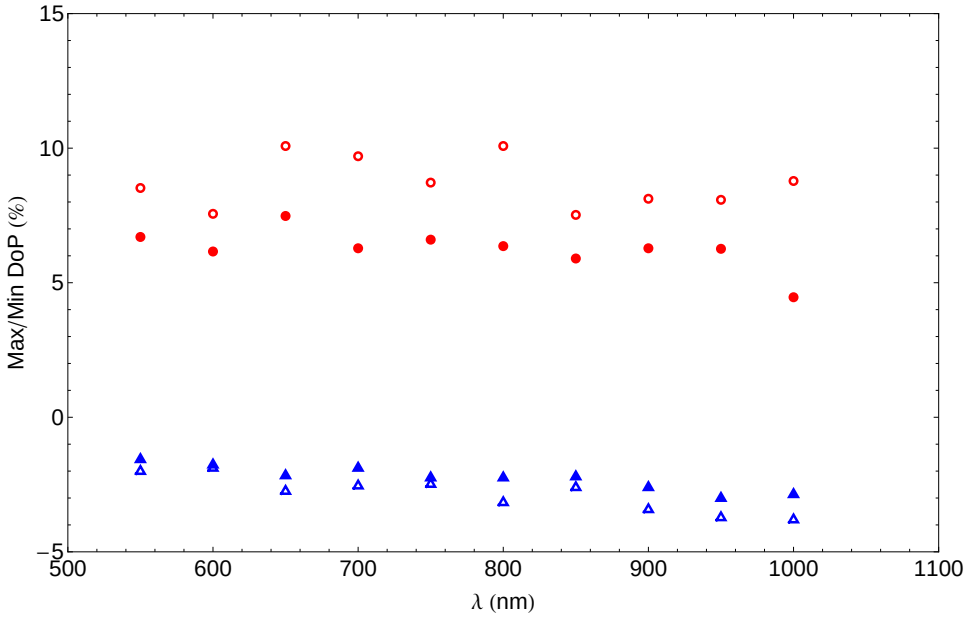

Figure 6.5: Maximum polarization on the edge of graphene device N2 and minimum polarization in its bulk taken from the ROIs of Fig. 6.4 as a function of wavelength.

6.4 Graphene Pyrometry

6.4.1 Thermal Profile

By the Stefan-Boltzmann law and assuming the standard emissivity $\pi\alpha$, a 15 μm $\times$ 15 μm graphene sheet at 2000 K dissipates roughly 4.7 μW of power by radiation. This power loss is much smaller than the electrical power applied to a sheet, which we measure to be on the order of mW. With this result and the fact that current in graphene flows isotropically along its length, we apply the same 1-D heat equation treatment to graphene as in the MWCNT case. The temperature distribution and maximum temperature are described by Eqs. 2.9 and 2.22 with the substitution $\pi(b^2 - a^2) \to L \cdot W$, where W is the sheet width.

Because the graphene length 15 μm $> L_{\text{MWCNT}}$, the temperature varies more slowly with length along the graphene as compared to the that for the nanotubes. Assuming graybody, Lambertian emission, the count rate is given by

$$\dot{S}^p(i,j) = \epsilon\Theta_\lambda \left(\int_{\text{NA}} \cos\theta d\Omega\right) \frac{c\Delta\lambda}{\lambda^4}\frac{\beta^2\pi}{4\lambda^2} \iint e^{-C_2/\lambda T(l,w)} e^{-[(l-i\beta)^2+(w-j\beta)^2]/2(.42\lambda)^2} dldw, \quad (6.6)$$

using the PSF of Eq. 4.9. Expanding the temperature profile by Eq. 2.28 and making use of the fact that the $W \gg \beta$, the integral over the w coordinate is performed from $-\infty$ to ∞, finding

$$\begin{aligned}\dot{S}^p(i,j) = \epsilon\Theta_\lambda \frac{\pi}{4}\frac{\beta^2 c\Delta\lambda}{\lambda^4}\frac{.42\pi\sqrt{2\pi}}{4\lambda} e^{-C_2/\lambda T_m} \\ \times \int_{-L/2}^{L/2} \exp\left[-\left(\frac{4C_2(T_m - T_0)}{\lambda L^2 T_m^2}\right) l^2 - \frac{(l-i\beta)^2}{2(.42\lambda)^2}\right] dl.\end{aligned} \quad (6.7)$$

As with the MWCNT, completing the square and taking the limit $L \to \infty$ allows the integral over l to be performed, finding the image of the graphene sheet away from the edges to be

$$\dot{S}^p(i,j) = \epsilon\frac{(.42)^2\pi^2\eta}{2}\Theta_\lambda\frac{\pi}{4}\frac{\beta^2 c\Delta\lambda}{\lambda^4} e^{-C_2/\lambda T_m} e^{-(i\beta)^2(1-\eta^2)/2s^2}, \quad (6.8)$$

with η as previously defined in Eq. 4.14. Because $L = 15$ μm, $\eta \approx .98$, and the gaussian profile is roughly constant on the scale of a pixel; the peak intensity given by

$$\dot{S}^p_{\max} = \epsilon\frac{(.42)^2\pi^2\eta}{2}\Theta_\lambda\frac{\pi}{4}\frac{\beta^2 c\Delta\lambda}{\lambda^4} e^{-C_2/\lambda T_m} \quad (6.9)$$

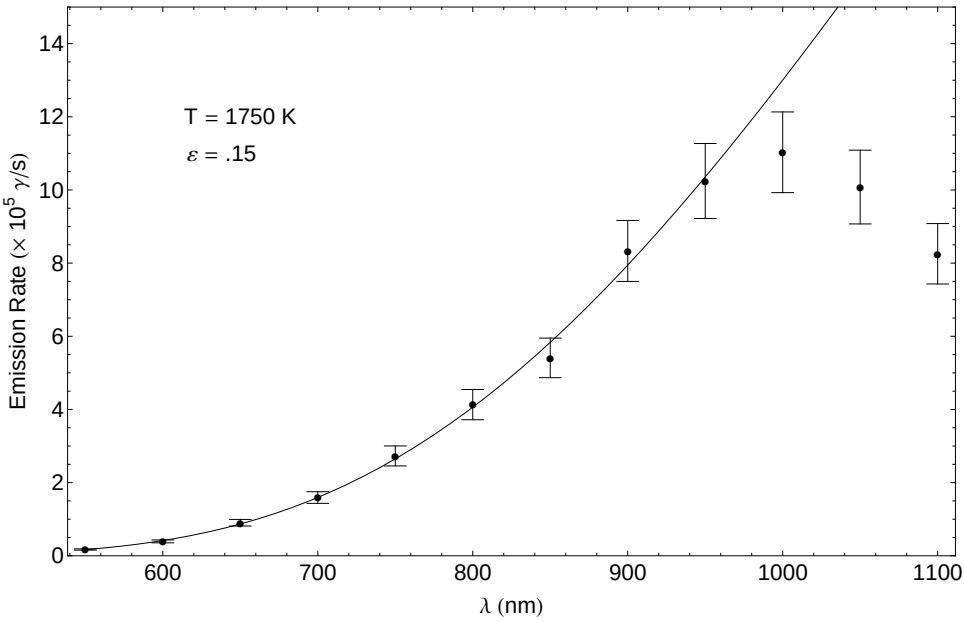

Figure 6.6: Absolute spectrum as measured from device N2 at maximum operating power, along with associated graybody fit. An infrared suppression is seen in the signal above 1000 nm that is unseen in the monotonically increasing graybody function.

will be roughly constant over a length $\sim \lambda/2$. The prefactor of $(.42)^2\pi^2\eta/2 \approx .85 < 1$ iindicates that the radius of the circle of constant intensity is less than the first minimum in the Airy function. We can therefore average over $\sim 5 - 25$ pixels for pyrometry analysis.

6.4.2 Multiwavelength Pyrometry

As with the MWCNT filaments, we measure spectra of graphene over a range of filters, powers, and polarization. Graphene is expected to be gray in the visible-NIR; thus, we perform multiwavelength pyrometry to extract the emissivity and temperature. We observe a suppression in signal at long wavelengths, consistent with MWCNT spectra, that has a magnitude far larger than the effect predicted by the temperature-dependent term of Eq. 1.16. As such, we perform our multiwavelength fits to the data representing $\lambda \leq 1000$ nm; Fig. 6.6 shows one such spectrum and the associated fit.

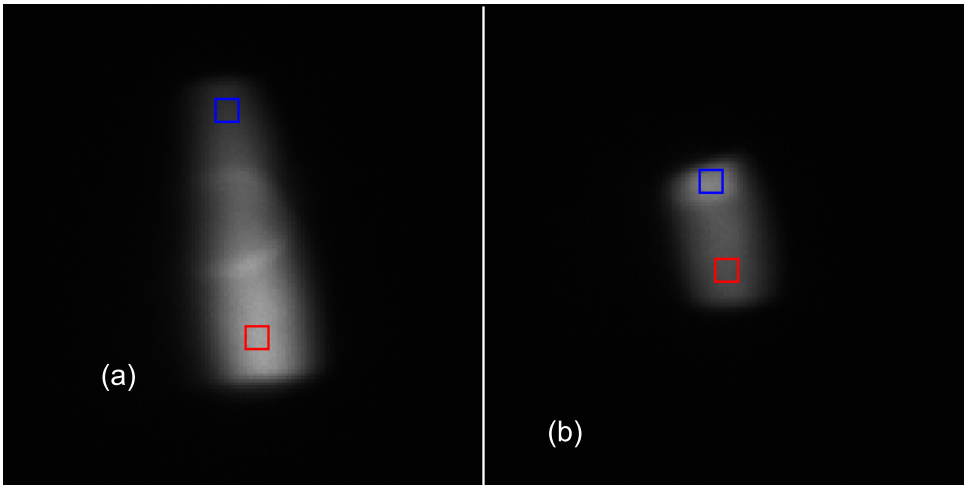

Figure 6.7: Representative optical data from devices N2 (left) and N6 (right), along with ROIs over areas of differing thickness used in pyrometry.

One result of using mechanical exfoliation to produce graphene samples is that often the sample produced consists of regions with differing numbers of layers, as can be seen in Fig. 6.1. Therefore, on a large enough device, we can perform pyrometry on independent regions and measure emissivities consistent with this layer differential. For both these devices, the mean counts are measured over a square of $\sim 5 \times 5$ pixels^2 in two separate regions believed to be of different thicknesses, shown in Fig. 6.7.

Figure 6.8 and its legend summarize the results for this pyrometry. We find that for each region, temperatures of both polarizations are consistent; yet the temperature on one end of the device differs from that at the other. Because of the layer number differential, the sheet admits a non-isotropic current density, resulting in a slight temperature gradient along the width of the graphene.

Device N2 is found to consist of subsections with emissivities $.13 \pm .03$ and $.16 \pm .04$, consistent with being comprised of 6 ± 1 and 7 ± 1 layer graphene, respectively. Similarly, two emissivities of $.04 \pm .01$ and $.06 \pm .01$ measured on device N6 indicates it consists of a double layer of graphene with a small triple layer region.

Finally, as with MWCNTs, the thermal conductivity can be determined by fitting $T_{\max}(P)$ to Eq. 2.23. We find room temperature thermal conductivities between 5000 and 21000 W/m·K,

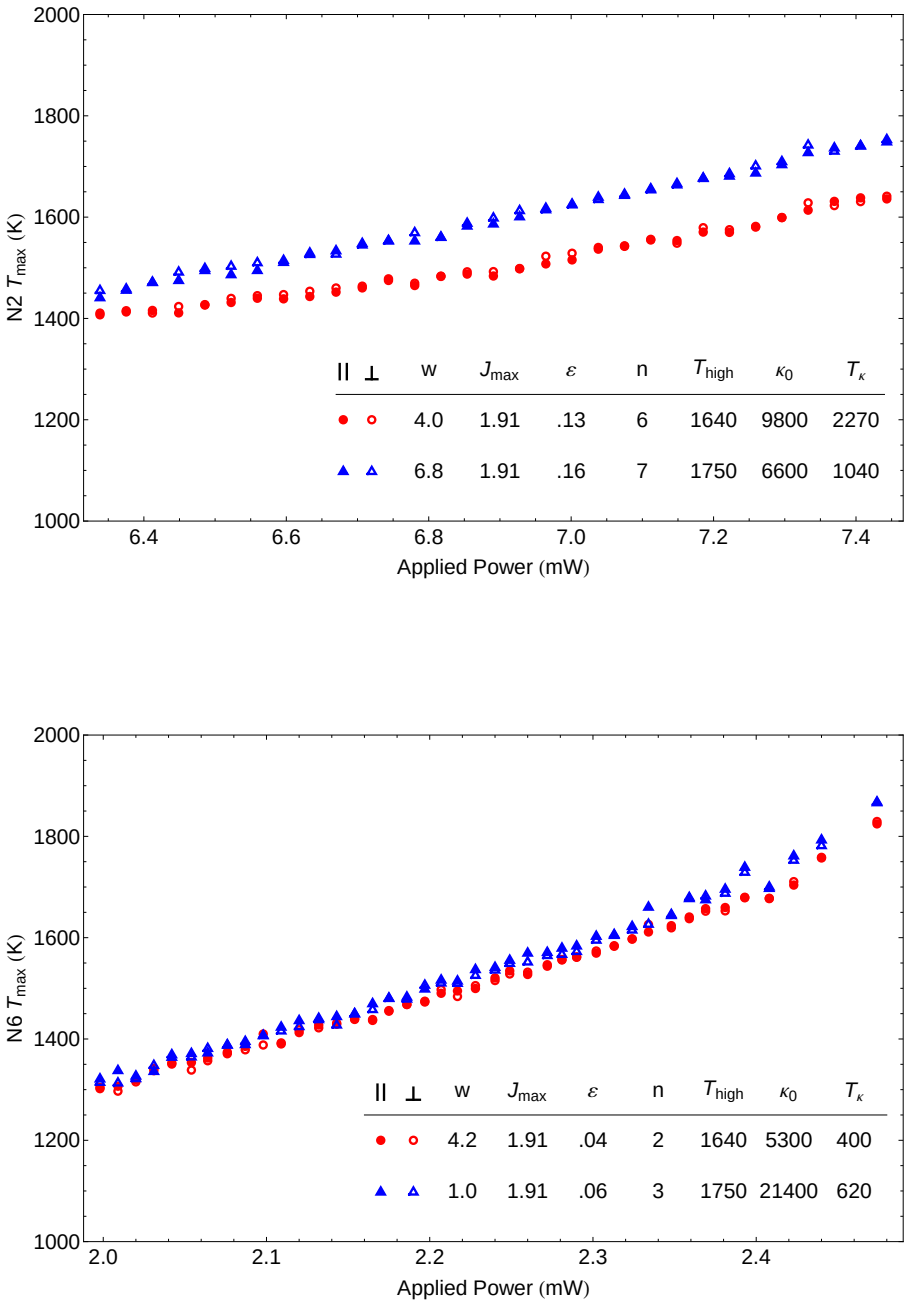

Figure 6.8: Temperature as a function of power for devices N2 and N6. Polarizations are defined by parallel (perpendicular) along the graphene's length (width). Current densities are in mA and widths are in mum.

consistent with values measured previously[84, 85] to within a factor of 4, and that Umklapp scattering becomes dominant at much lower temperatures for the thinner graphene sample than for the thicker one.

6.4.3 Absorption and Kirchoff's Law

In addition to measuring the emissivity by optical pyrometry, the absorption can also be measured in our setup optically. The membrane on both devices measured had a hole, allowing the absolute number of photons incident on the membrane by our backlight to be obtained. Furthermore, having biased the graphene samples to temperatures in excess of 1800 K each for many hours, the already thinned membrane evaporated has sublimated underneath the incandescent region of the graphene. The suspension was confirmed using TEM microscopy, seen in Fig. 6.9.

The reflection of graphene is second-order in $\pi\alpha \ll 1$, therefore $A = 1-T$. The ratio of the intensity observed on the graphene sheet to that in the membrane hole in a backlit, unbiased exposure gives the transmission, and therefore the absorption, of the graphene sheets. One such spectrum is shown in Fig. 6.10. To compare the absorption to the emission, we average data up to 1000 nm; the absorptions obtained thus are plotted versus the emissivity as a function of applied power in Fig. 6.11. The absorptivity is found to be consistent with the emissivity, as expected by Kirchoff's law.

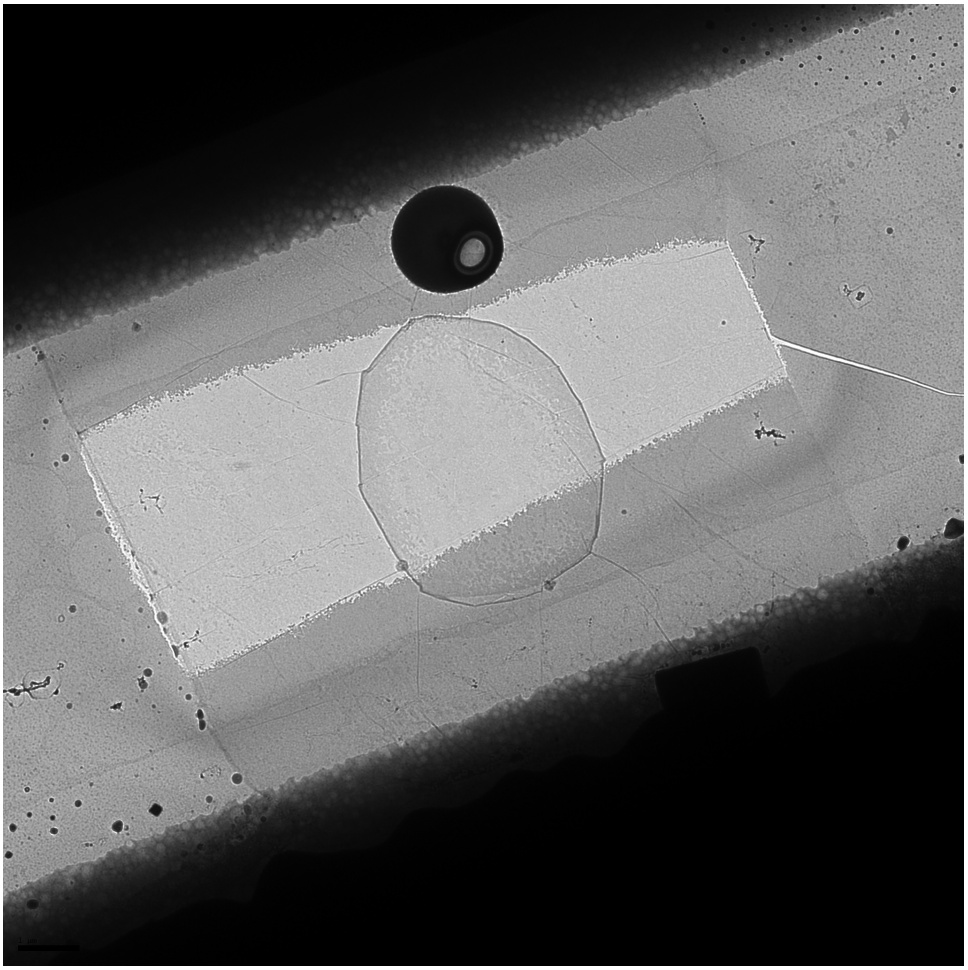

Figure 6.9: Bright field TEM image of N6, indicating that the membrane underneath the graphene has evaporated after many hours of biasing. Image courtesy of William Hubbard.

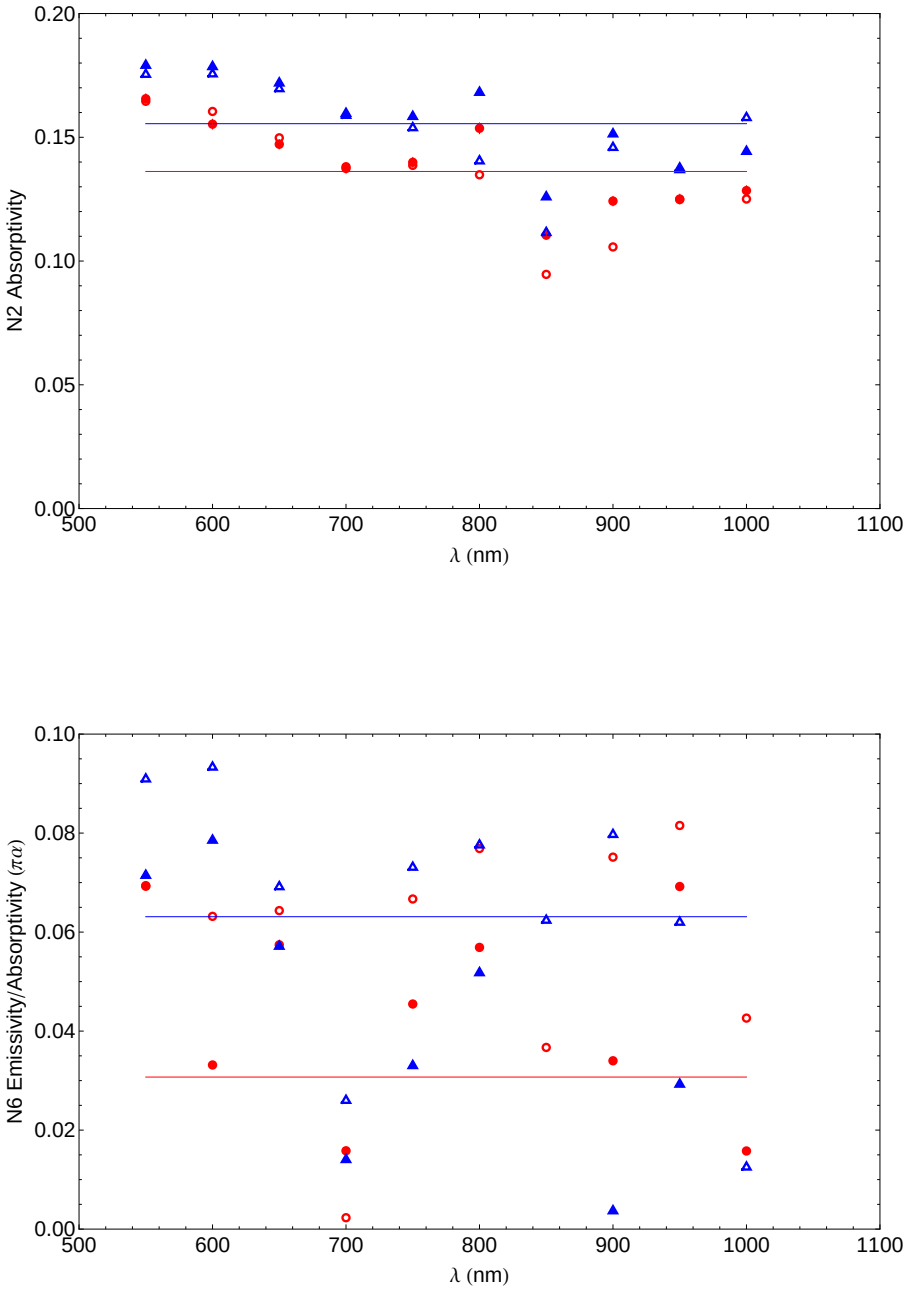

Figure 6.10: Absorption as a function of wavelength calculated by measuring transmisson through the graphene sheets and through holes in the membrane, and their associated means.

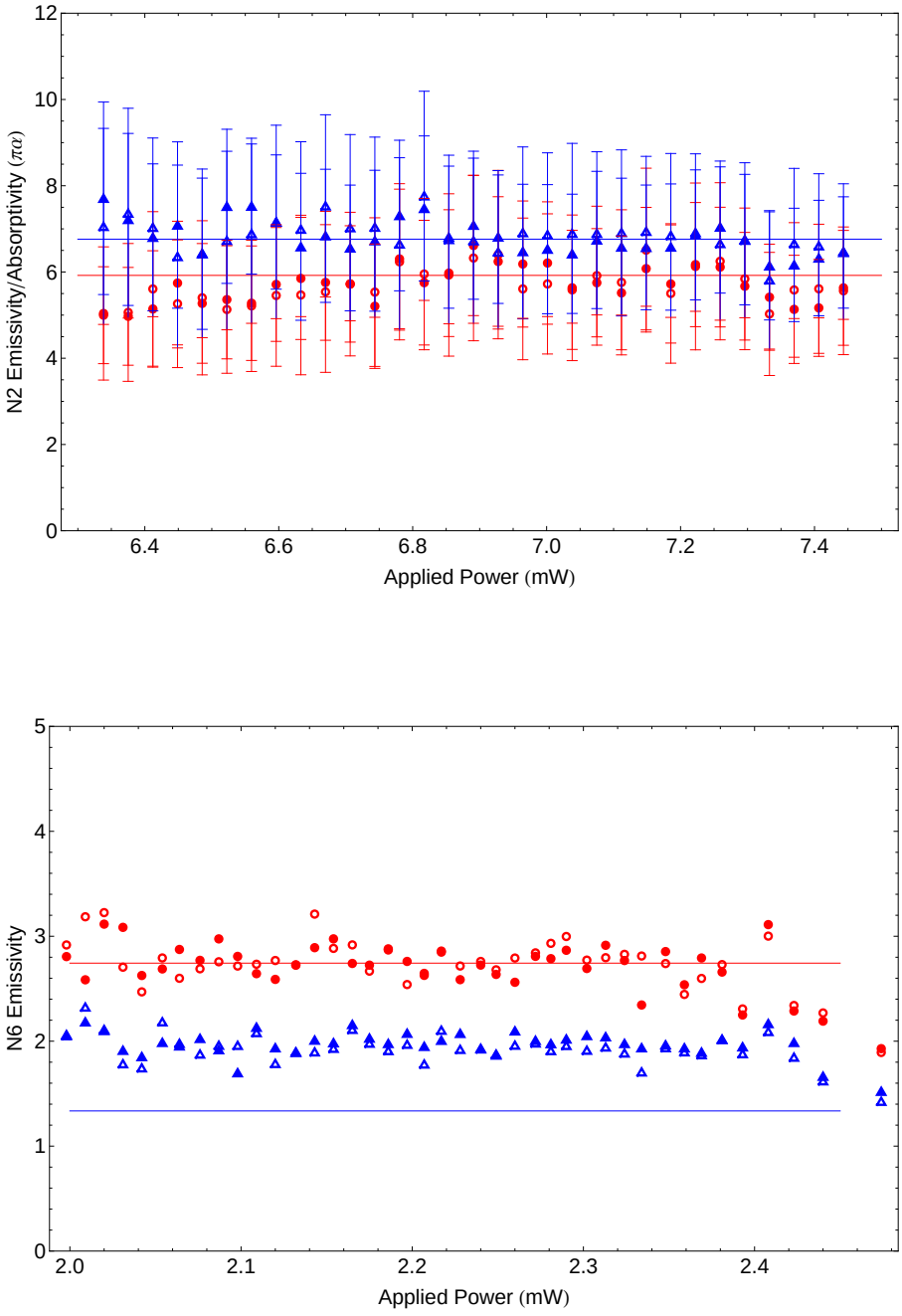

Figure 6.11: Emissivity as a function of power for devices N1 and N2 in units of $\pi\alpha$. Solid lines are the associated mean absorptivities.

CHAPTER 7

Conclusion

We have performed absolute pyrometric measurements on fully characterized MWCNTs and graphene joule-heated to temperatures in excess of 2000 K. By calibrating the optics used to image the incandescent nanodevices, we obtain spectra in the visible and near infrared of the total number of photons emitted into the numerical aperture of the microscope with an error of $\lesssim 10\%$. Data from both orthogonal polarizations of light are collected on the CCD simultaneously using a Wollaston prism in conjunction with the microscope. These data are recorded over a range of wavelengths and powers.

The emission of a MWCNT is modeled using the classical Mie theory for an infinitely long hollow cylinder. Each pixel on the CCD records an independent measurement of the emission; by measuring the CNT's geometry in a high resolution TEM and assuming that each nanotube wall has the 2-D conductivity of graphene $\sigma_g Z_0 = \pi\alpha$, we solve Planck's law to obtain temperature values. A weighted average across all wavelengths measured yields the temperature to ± 100 K–equivalently, the emissivity consistent with the Mie absorption coefficient Q to within a factor of 2. *In situ* observation of membrane evaporation in a TEM under nanotube bias allows us to correlate our measured temperatures with expected sublimation temperatures of SiO_2 and Si_3N_4. Similarly, polarization measurements give the emissivity as within a factor of 2 from Q predicted by Mie absorption.

By enforcing the constraint that the temperature given by both polarizations must be equal, we solve for the CNT optical conductivity and find that $\sigma_0 = (1.0 \pm 0.5)\pi\alpha$. The thermal conductivity is obtained from fitting $T(P)$ to an Umklapp scattering model, and we find values for our MWCNTs consistent with the literature.

This technique is applied to incandescent sheets of graphene as well. Our pyrometry confirms that suspended graphene emits as a graybody with the theoretical emissivity $= n\pi\alpha$

where n is the number of layers. Furthermore, with large graphene sheets, the absorptivity is also measured and found to match this emissivity, in agreement with Kirchoff's law of thermal radiation. The thermal conductivity is also measured to within a factor of 4 of literature values. Finally, the graphene sheets are found to be unpolarized in their brightest regions, but display polarization on the order of 18% in the direction of the length near the edge. Surprisingly, the sheet is also polarized along its width to the order of 7% away from the bright spot.

The spectra of the graphene samples display infrared suppression at high temperature, an effect also seen in the MWCNT spectra and polarization. This decrease in signal is believed to originate from a shift of the Fermi energy due to trapped surface charges, which causes interband optical transitions to become forbidden. As the CNT energy bands derive from graphene's band structure, we conclude that a similar effect arises in MWCNT emission and supresses polarization as well.

In conclusion, we have demonstrated that pyrometry of thermal emitters with $r \ll \lambda$ is not only possible, but tractable with the classical electrodynamics definition of a cross-section as the emitting area in Planck's law. Furthermore, a reasonable emission model not only yields the temperature of the object, but its optical and thermal conductivities as well. Thus pyrometry is indeed a powerful tool in probing subwavelength objects at thermal extremes. The properties of graphene and MWCNTs obtained in this way indicate that precise optical modulation of the visible thermal spectrum is possible with the correct biasing conditions, leading the way to novel carbon electrooptical devices.

APPENDIX A

Absorption Coefficients of an Infinitely-Thin Conducting Sheet

A.0.4 Incident, Reflected, and Transmitted Waves

Consider two regions of space, designated I and II, separated by an infinitely thin conducting plane at $z = 0$. A plane wave propagating in region I is incident on this conductor with angle θ_i. The wave is partially reflected, propagating in region I away from the sheet, at angle θ_i, and partially transmitted, propagating in region II at angle θ_t. The angles are related by Snell's law: $m_I \sin\theta_i = m_{II} \sin\theta_t$, where m_I and m_{II} are the indices of refraction in the related region.

The wavevectors of the incident, reflected, and transmitted waves are

$$\begin{aligned} \vec{k_i} &= k_I(\sin\theta_i\hat{x} + \cos\theta_i\hat{z}) \\ \vec{k_r} &= k_I(\sin\theta_i\hat{x} - \cos\theta_i\hat{z}) \\ \vec{k_t} &= k_{II}(\sin\theta_i\hat{x} + \cos\theta_i\hat{z}) \end{aligned} \tag{A.1}$$

with $k_I = 2\pi m_I/\lambda$. Maxwell's equations give the boundary conditions at $z = 0$:

$$\begin{aligned} (\vec{E}_I - \vec{E}_{II})\Big|_{z=0} \times \hat{n} &= 0 \\ (\vec{H}_I - \vec{H}_{II})\Big|_{z=0} \times \hat{n} &= \vec{K}_{\text{free}} \end{aligned} \tag{A.2}$$

with $\vec{K}_{\text{free}}$ the free surface current density in the conducting plane.

A.0.5 s-polarization

We must consider two cases of polarization: $\vec{E}_i$ parallel and perpendicular to the surface, denoted as s and p polarizations, respectively. We shall consider the parallel case first. Since

we have defined the wavevector to be in the x-z plane, the polarization where the electric field is always parallel to the surface is the $\hat{y}$ direction. Thus, $\vec{E}_i = E_i\hat{y}$, $\vec{E}_r = E_r\hat{y}$, and $\vec{E}_t = E_t\hat{y}$, and the magnetic fields are given by $\vec{H} = \vec{k} \times \vec{E}/Z$, where Z is the impedance of the medium. By Ohm's law, the free current is the conductivity by the electric field in the x-y plane at $z = 0$:

$$\vec{K}_{\text{free}} = \frac{\sigma_{2D}}{2}(E_i + E_r + E_t)\hat{y} = \sigma_{2D}(E_i + E_r)\hat{y} = \sigma_{2D}E_t\hat{y}. \tag{A.3}$$

Solving the four equations of the boundary conditions yields the ratios of the incident field that is reflected or transmitted:

$$\begin{aligned}
\frac{E_r}{E_i} &= \frac{Z_{II}\cos\theta_i - Z_I\cos\theta_t - Z_IZ_{II}\sigma_{2D}}{Z_{II}\cos\theta_i + Z_I\cos\theta_t + Z_IZ_{II}\sigma_{2D}} = \frac{Z_{II}\cos\theta_i - Z_I\sqrt{1 - \frac{m_I}{m_{II}}\sin^2\theta_i} - Z_IZ_{II}\sigma_{2D}}{Z_{II}\cos\theta_i + Z_I\sqrt{1 - \frac{m_I}{m_{II}}\sin^2\theta_i} + Z_IZ_{II}\sigma_{2D}} \\
\frac{E_t}{E_i} &= \frac{2Z_{II}\cos\theta_i}{Z_{II}\cos\theta_i + Z_I\cos\theta_t + Z_IZ_{II}\sigma_{2D}} = \frac{2Z_{II}\cos\theta_i}{Z_{II}\cos\theta_i + Z_I\sqrt{1 - \frac{m_I}{m_{II}}\sin^2\theta_i} + Z_IZ_{II}\sigma_{2D}}.
\end{aligned} \tag{A.4}$$

The reflected and transmitted intensities are found by squaring the norm of these ratios:

$$\begin{aligned}
R^s(\theta) &= \left|\frac{Z_{II}\cos\theta_i - Z_I\sqrt{1 - \frac{m_I}{m_{II}}\sin^2\theta_i} - Z_IZ_{II}\sigma_{2D}}{Z_{II}\cos\theta_i + Z_I\sqrt{1 - \frac{m_I}{m_{II}}\sin^2\theta_i} + Z_IZ_{II}\sigma_{2D}}\right|^2 \\
T^s(\theta) &= \left|\frac{2Z_{II}\cos\theta_i}{Z_{II}\cos\theta_i + Z_I\sqrt{1 - \frac{m_I}{m_{II}}\sin^2\theta_i} + Z_IZ_{II}\sigma_{2D}}\right|^2.
\end{aligned} \tag{A.5}$$

A.0.6 p-polarization

The coefficients for perpendicular polarization are solved in the same manner, with the following substitution for fields: $\vec{E}_i = E_i(-\cos\theta_i\hat{x} + \sin\theta_i\hat{z})$, $\vec{E}_r = E_r(\cos\theta_i\hat{x} + \sin\theta_i\hat{z})$, and $\vec{E}_t = E_t(-\cos\theta_t\hat{x} + \sin\theta_t\hat{z})$, and the corresponding expressions for $\vec{H}$. With this polarization, the free current density is

$$\vec{K}_{\text{free}} = -\frac{\sigma_{2D}}{2}(\cos\theta_i(E_i + E_r) + \cos\theta_tE_t)\hat{y} = -\sigma_{2D}\cos\theta_i(E_i + E_r)\hat{y} = -\sigma_{2D}\cos\theta_tE_t\hat{y}. \tag{A.6}$$

The reflection and transmission coefficients are found to be

$$R^p(\theta) = \left(\frac{Z_{II}\sqrt{1-\frac{m_I}{m_{II}}\sin^2\theta_i} - Z_I\cos\theta_i - Z_IZ_{II}\sigma_{2D}\cos\theta_i\sqrt{1-\frac{m_I}{m_{II}}\sin^2\theta_i}}{Z_{II}\sqrt{1-\frac{m_I}{m_{II}}\sin^2\theta_i} + Z_I\cos\theta_i + Z_IZ_{II}\sigma_{2D}\cos\theta_i\sqrt{1-\frac{m_I}{m_{II}}\sin^2\theta_i}} \right)^2$$
$$T^p(\theta) = \left(\frac{2Z_{II}\cos\theta_i}{Z_{II}\sqrt{1-\frac{m_I}{m_{II}}\sin^2\theta_i} + Z_I\cos\theta_i + Z_IZ_{II}\sigma_{2D}\cos\theta_i\sqrt{1-\frac{m_I}{m_{II}}\sin^2\theta_i}} \right)^2. \tag{A.7}$$

At normal incidence, $\theta_i = \theta_t = 0$, Eqs. A.5 and A.7 approach the same values

$$R(0) = R^s(0) = R^p(0) = \left(\frac{Z_{II} - Z_I - Z_IZ_{II}\sigma_{2D}}{Z_{II} + Z_I + Z_IZ_{II}\sigma_{2D}} \right)^2$$
$$T(0) = T^s(0) = T^p(0) = \left(\frac{2Z_{II}}{Z_{II} + Z_I + Z_IZ_{II}\sigma_{2D}} \right)^2. \tag{A.8}$$

A.0.7 Absorption Coefficients

These coefficients are in their most general form, which is useful for measuring the reflection or transmission for graphene on a substrate. A useful limit, however, occurs when the graphene is suspended, or when $m_I = m_{II}$. The reflections and transmissions are

$$R^s = \left(\frac{\sigma_{2D}Z}{2\cos\theta+\sigma 2DZ}\right)^2 \quad T^s = \left(\frac{2\cos\theta}{2\cos\theta+\sigma_{2D}Z}\right)^2$$
$$R^p = \left(\frac{\sigma_{2D}Z\cos\theta}{2+\sigma_{2D}Z\cos\theta}\right)^2 \quad T^p = \left(\frac{2}{2+\sigma_{2D}Z\cos\theta}\right)^2. \tag{A.9}$$

and at normal incidence,

$$R(0) = R^s(0) = R^p(0) = \left(\frac{\sigma_{2D}Z}{2 + \sigma_{2D}Z} \right)^2$$
$$T(0) = T^s(0) = T^p(0) = \left(\frac{2}{2 + \sigma_{2D}Z} \right)^2. \tag{A.10}$$

However, moreso than reflection and transmission, we are interested in absorption, defined here by $A = 1 - T - R$. The absorption coefficients for a suspended conducting sheet are

$$A^s(\theta) = \frac{4\cos\theta\sigma_{2D}Z}{(2\cos\theta + \sigma_{2D}Z)^2}$$
$$A^p(\theta) = \frac{4\cos\theta\sigma_{2D}Z}{(2 + \sigma_{2D}Z\cos\theta)^2} \tag{A.11}$$

which both become, at normal incidence,

$$A^s(0) = A^p(0) = \frac{4\sigma_{2D}Z}{(2 + \sigma_{2D}Z)^2}. \tag{A.12}$$

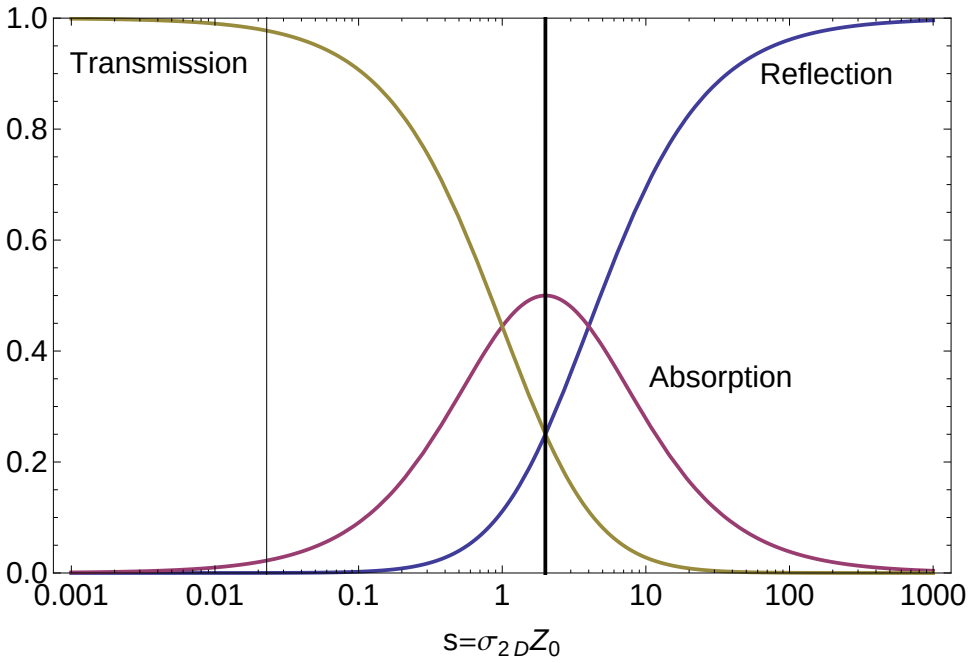

Figure A.1: Plot of the transmission, reflection, and absorption coefficients at normal incidence for a infinitely thin 2d conduction sheet as a function of $s = \sigma_{2D} Z$.

The quantity $s \equiv \sigma_{2D} Z$ is unitless, and values for R, T, and A, are plotted in Fig. A.1 as a function of s. In the insulator limit, when s is small, transmission dominates; in the conductor limit, when s is large, reflection dominates. However, for mediocre conductors, absorption becomes greater than both reflection and transmission, reaching a maximum of $1/2$ when $s = 2$, or $\sigma_{2D} = 2/Z$.

APPENDIX B

TEM Images of MWCNT Devices

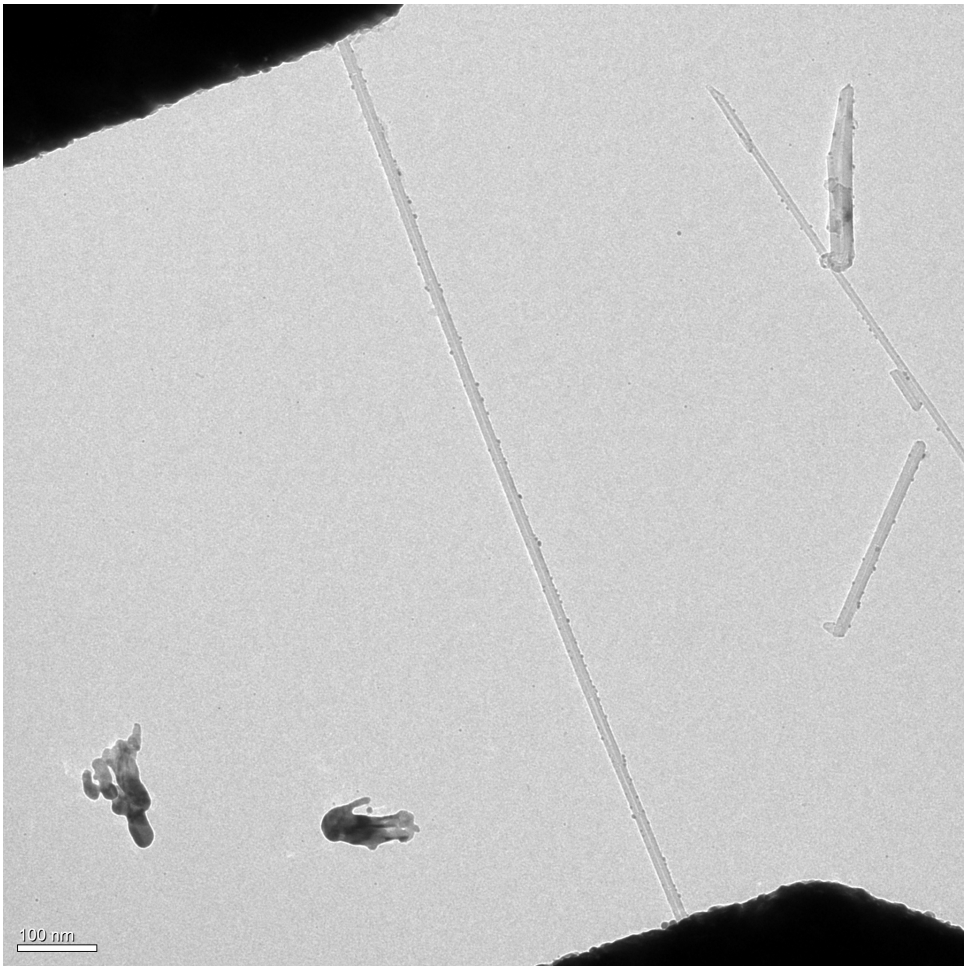

Figure B.1: TEM image of device A1001C. Image courtesy of Matthew Mecklenburg.

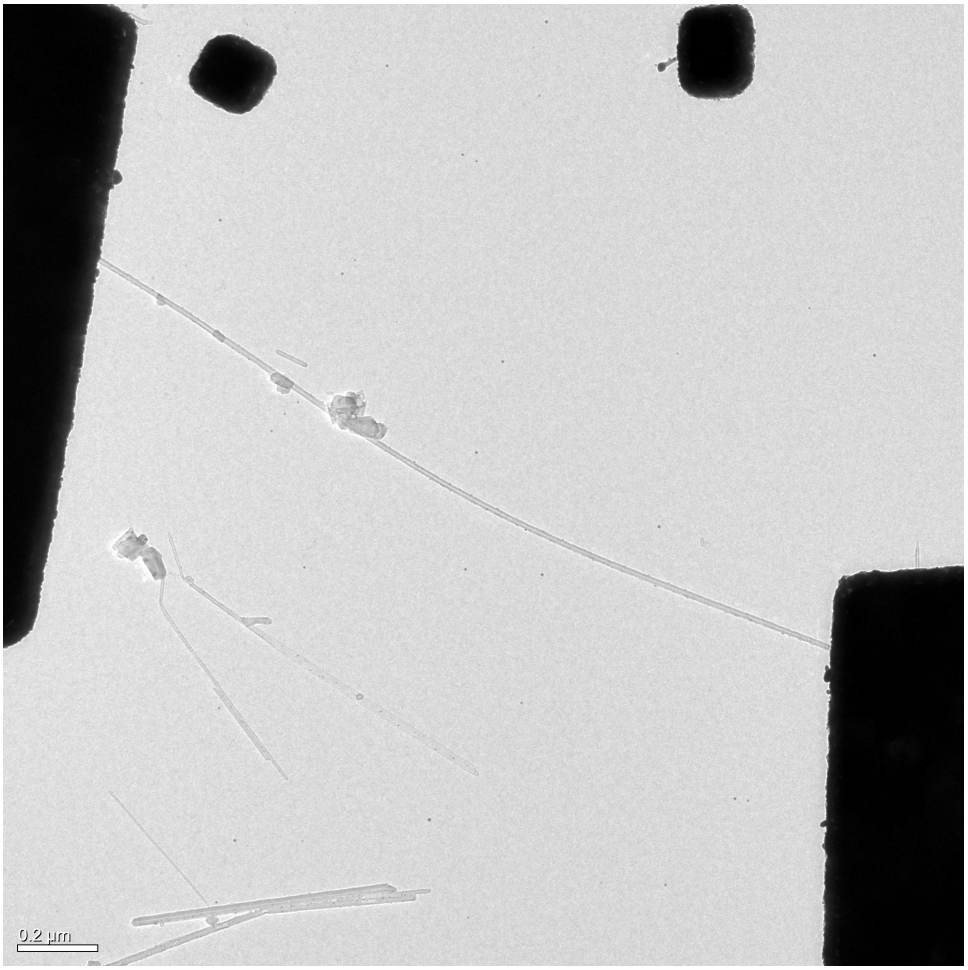

Figure B.2: TEM image of device A1003H. Image courtesy of Matthew Mecklenburg.

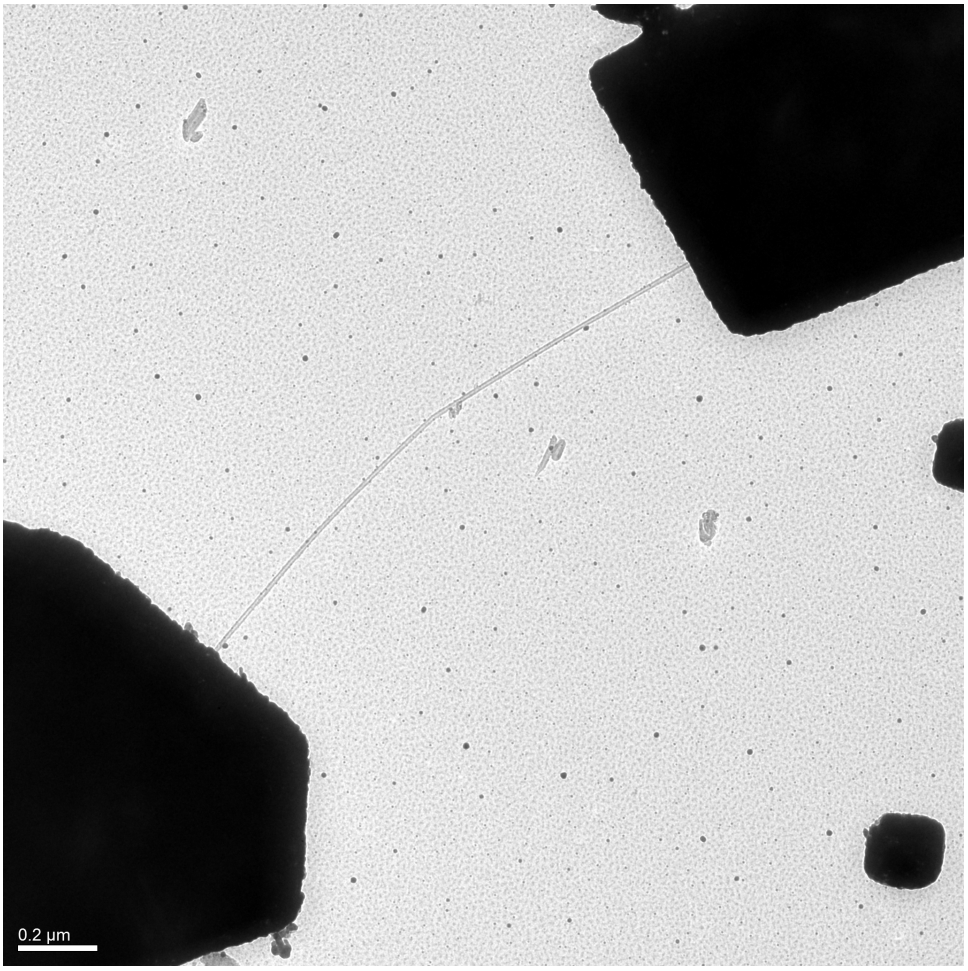

Figure B.3: TEM image of device A1008I. Image courtesy of Matthew Mecklenburg.

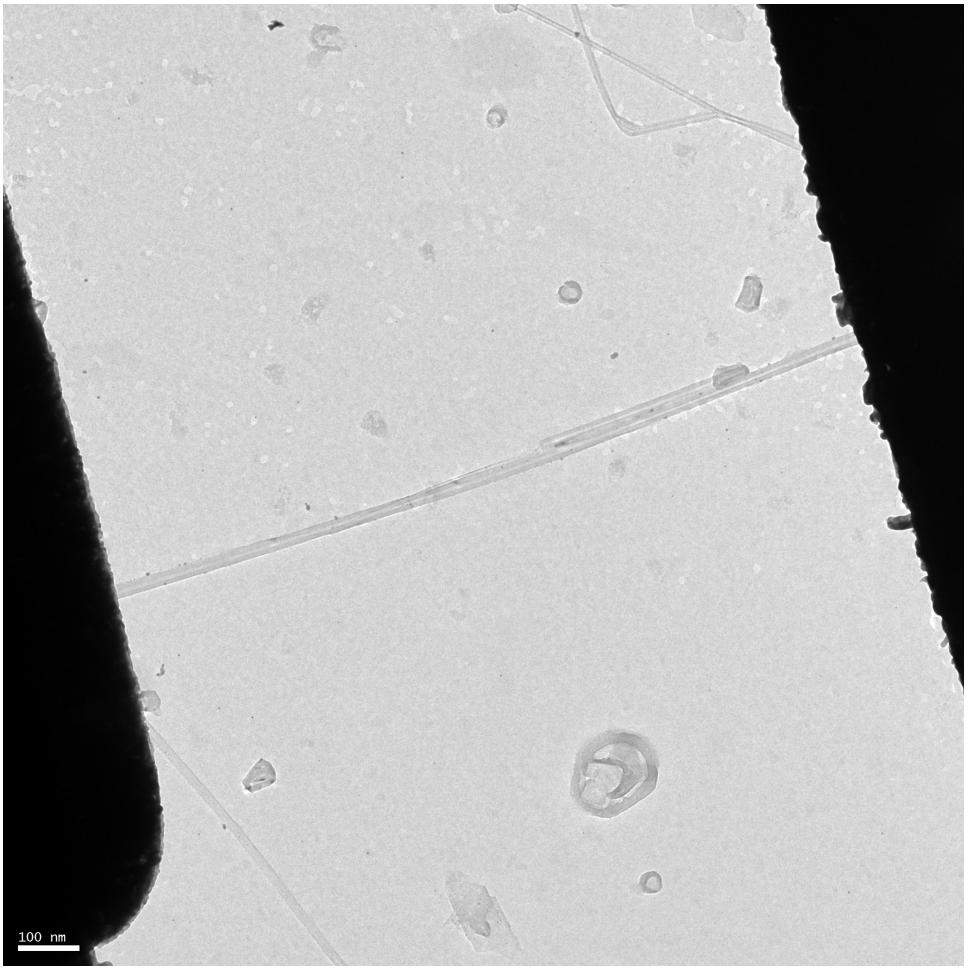

Figure B.4: TEM image of device A1308G. Image courtesy of Matthew Mecklenburg.

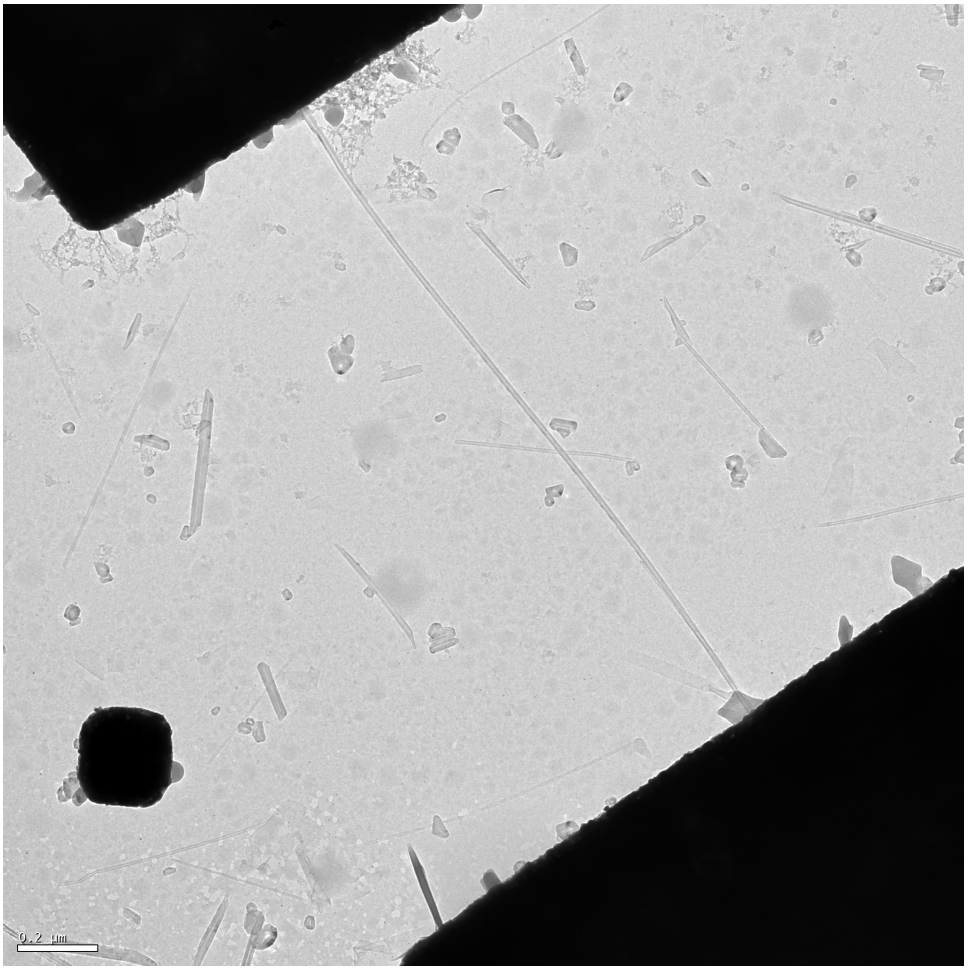

Figure B.5: TEM image of device A1321F. Image courtesy of Matthew Mecklenburg.

Figure B.6: TEM image of device A1321J. Image courtesy of Matthew Mecklenburg.

APPENDIX C

Fabrication Recipe

C.0.8 SiO2 film growth

For new wafers direct from factory, a preclean is not necessary. Otherwise, clean the wafers with Piranha (5:1 H_2SO_4:H_2O_2) for at least an hour to remove organic residue. Native oxides can be removed with a preclean of Buffered Oxide Etch (BOE).

Place the wafers in the oxidation furnace and grow oxide to the desired thickness. Many tools are online for calculating the growth time necessary given a starting and ending thickness and temperature (growth rate for oxide slows exponentially). The wet recipe at 1100 °C has the fastest rate, but at the cost of potentially more pinhole defects. The recipe is not generally important, and neither are these defects for this process.

A good thickness to work with is around 800 nm. A layer as thin as 300 nm will be generally stable enough to withstand KOH etching and rinsing if there is not much over etching, but may rupture under the heat from plasma cleaning. Use the nanospec or ellipsometer to check the final thickness grown on the wafers.

C.0.9 Si3N4 film growth

Again, for new wafers direct from factory or just out of the oxidation furnace, a preclean is not necessary. Otherwise, preclean as described in the previous step.

Load the wafers into the LPCVD Nitride furnace. Center the wafers as well as possible in the boat, placing them two to three slots apart for ideal uniformity. Because the wafers are polished on both sides, the direction does not matter. Place a bare Si dummy wafer behind the device wafers with the shiny side facing out of the furnace.

Load the Nitride.002 program. Check the logbook to see the previous growth rate. The target thickness of 15 nm is grown in a short enough time that an inaccuracy of ±5 nm should be expected. On July 8, 2010, the furnace grew about 19 ± 1 nm of Si_3N_4 in 1 min 30 sec.

After removing the wafers from the furnace, check the nitride thickness on the Si dummy wafer using the Nanospec or ellipsometer. Check several locations on the wafer to test uniformity.

C.0.10 First Optical Lithography

Before spinning on the photoresist, dehydrate the wafer by placing it on a hot plate at 150 °C for 5 minutes and then placing it in the HMDS tank for 10 minutes.

After the wafer has been dehydrated, place it on the 4" wafer chuck in the photoresist spinner. Program a spinner recipe with that ramps to 4000 rpm at a rate of 1000 rpm/s and spins for 30 seconds. The second step should ramp back down to 0 rpm. Turn the vacuum on before spinning, else the wafer tends to fly off during the ramp up. Put at least 3 eyedroppers worth of AZ 5214E photoresist in the center of the wafer. Start the spin coater.

If the photoresist spin coating is not satisfactory, rinse with acetone, IPA, and water in that order to remove it. After rinsing, it is necessary to redo the dehydration steps. Once it has been baked above 120 °C then an ALEG355 bath is necessary to strip the photoresist!

Following the spin coating, perform a soft bake on a hot plate at 105 °C for 1 minute.

Put the KOH mask in the Karl Suss aligner. Make sure that the chrome side will be pressed against the wafer. If the mask features cannot be focused in the microscope after WEC, it probably is the wrong side up. Load the wafer photoresist side, ensure that the wafer calipers are sufficiently centered, and expose using Hard Contact mode for 13 seconds. The correct alignment for the KOH etch to work properly is to have the wafer flat parallel as the holes. That is, it should be along one of the mask directions, not at a 45° angle. There should be a marking on the chuck to which to align the wafer.

Make a solution of 1:6 AZ400K Developer:H_2O. Immerse the wafer for 45 seconds. Re-

move and rinse thoroughly with water. Hard bake the wafer on a hot plate at 125 °C for 3 minutes. After this step it is ok to take the wafer into normal light. Check features in a microscope to make sure the patterns are as desired.

C.0.11 Plasma Etch

Using a spatula, apply a bit of cool grease to a clean 400 nm or 500 nm thick carrier wafer. Place the wafer on cleanroom paper and, using a Q-tip, spread a thin layer of cool grease on the whole of the wafer. If you use too little, the PR will burn and the oxide will be etched. If you use too much, it will be harder to remove the grease, creating more scratches on the oxide where the KOH can get through. A good metric is the grease shouldn't be glaringly white, but noticeably there while some shinyness from the wafer can still be seen.

Place the exposed wafer PR side up on the carrier wafer and cool grease, with the major flats aligned. Use tweezers to apply a bit of pressure to ensure that the wafer sits flat on the carrier wafer - *i.e.* that it is in contact with the cool grease everywhere. Clean the bottom of the carrier wafer and the side of the sandwich as well as possible from cool grease by using a paper towel or Q-tip with acetone.

Put the carrier wafer/device wafer combo in the STS AOE with the flats aligned to the mark in the machine. Run the Oxidapic recipe for 1 minute with the RIE power 700 W and ICP power 100 W. The standard etch rate for this recipe is 300 nm SiO_2/min. After the machine vents, remove wafer and check the thickness of the SiO_2 in the holes using the Nanospec. In general, the 10x magnification should be sufficient to see the holes (the eyepiece's dot just needs to rest inside the area of interest), but for smaller features use the 40x objective on the Nanospec. This thickness measurement gives a more accurate value for the AOE's etch rate. Based on that etch rate, run the Oxidapic recipe again for the appropriate length of time to etch the remaining oxide.

C.0.12 KOH Etch

Put the wafer sandwich in a beaker with acetone to help dissolve the cool grease gluing the two wafers together. Let it sit for at least 30 minutes. When separating the wafers, applying

a rotational or lateral force to the device wafer is best. Pulling or pushing it transverse to the wafer is a great way to destroy it; it is not only thinner than the carrier wafer but now it has been significantly weakened by being etched in important crystal directions. Try to wedge the wafer tweezers in between the two wafers slightly and then rotate them along the wafer circumference to start the separation. This should make it significantly easier to separate.

After cleaning any remaining cool grease off the wafer with acetone, immerse it in the yellow room's photoresist stripping tank. It is filled with ALEG355, and should be set for 75 °C. After it reaches temperature, put the wafer in a Teflon holder, using the clamp so that the wafer doesn't fall out, and lower the wafer into the tank, anchoring it so it doesn't fall in. Let the wafer soak for 10 to 20 minutes, remove, and rinse with water.

In a large beaker, create a solution of 30% KOH. Because the KOH in the nanolab is 45% concentration, a mixture of about 1000:500 mL KOH:DI water should be sufficient to fill the beaker above wafer level. Adding some IPA to the surface will help the etch run at the proper rate and prevent evaporation of the mixture. Connect the temperature sensor to the hotplate. Turn the hotplate on to 80 °C with a stir bar stirring at 200 rpm. Place the beaker on the hotplate, lower the sensor into the beaker, and cover. It will take roughly 20-30 minutes for the solution to reach temperature.

Place the device wafers feature side up in the wafer cassette with at least one slot between wafers and at least 2 or 3 up from the bottom to make room for the spinner. Carefully lower the cassette into the beaker. The etch theoretically etches at a rate of 1 μm/min - for a 200 μm thick wafer, the etch takes 3 hours and 20 min. KOH also etches SiO_2 at a rate of 10 nm/min, so care should be taken not to overetch by more than 30 minutes. After the etch runs to completion, remove the wafers carefully-as they are much more fragile now-and rinse them in methanol, as if the membranes have been thinned by overetching a water rinse might rupture them.

C.0.13 Second Optical Lithography

Spin AZ 5214E resist on the unetched side of the wafer with the parameters used previously. Using backside alignment, expose the photoresist with the Electrode mask in the Karl Suss with the same exposure settings used in the first optical lithography step. There are three sets of plus-shaped alignment marks on the current mask on axes 45° to the wafer flats. The marks nearest an intersection of e-beam square cleavage lines are easiest to find and do not fill up the screen on the high magnification. Using these marks should produce alignment +/- 1 μm. Develop the photoresist as before.

Load the wafer into either the old or new CHA, and use the Cr/Au program. Set the evaporator to evaporate 60 Åof Cr and 1200 Åof Au at the respective rates of 1 Å/s and 3 Å/s. This is process 18 on the new CHA and it runs for about 3 hours. Place the wafer in a beaker of acetone for at least 60 minutes to liftoff the metal.

Following metal liftoff, place the wafer on a cleanroom paper towel and use a diamond scribe to separate it into the 1.2 cm x 1.2 cm ebeam squares.

C.0.14 Nanotube Dispersion

Measure out approximately 250 μg of MWCNT from the green-capped MER bottle or the arc-discharge stick in a 1.5 mL plastic tube using the analytic balance. Add 1 mL of IPA with the 1 mL pipette and shake thoroughly. Hold the tube in the ultrasound tank for 5 minutes at power 4 at one of the tank's antinodes. Usually a ripple effect is seen; the center of the ripples is the antinode. The nanotubes should start to disperse and the liquid in the tube should go from clear to a cloudy gray within a minute or two if positioned correctly.

After 5 minutes of sonication, remove the tube and shake for 30 seconds. Repeat the sonication and shaking 3 more times. Centrifuge the tube at 8000 rpm for 30 minutes, using a tube with 1 mL water in the opposite slot to equalize the weight distribution. If the nanotubes have been dispersed sufficiently, the tube should have a uniform dark gray blast pattern on the half which was facing the outside part of the centrifuge, and the liquid should be clear or a light gray. If the blast pattern consists predominately of black carbon chunks

or there is anything macroscopic floating in the liquid, the dispersion most likely did not succeed at the required densities.

Stick the square to a piece of the blue sticky tape in our lab. Turn on the N_2 and vacuum flows to the spin coater, and place the wafer on the chuck. Turn on the vacuum to make sure that the wafer is held firmly. Once the vacuum has been turned on, turning it off ruins the blue tape and will require the use of a new piece. Program C will start spinning the wafer at 500 rpm for 10 seconds and then ramp up to 3500 rpm. If the wafer does not seem secure at 500 rpm, stop the spinning and redo the tape.

Once the wafer is spinning at 3500 rpm, using the 100 μL pipette, draw clear liquid from the tube (avoiding darker gray part of the solution; it is full of carbon junk) and deposit it on the wafer one drop at a time. Allow the wafer to dry between drops (the wafer will appear to change from purple to green) lest the nanotubes clump into bundles. For one ebeam square, apply 400 or 500 μL of solution.

C.0.15 Nanotube Mapping

Load an ebeam square into the FIB by mounting as little of the corner as possible onto a small of carbon tape. The square should be affixed but still easy to remove so that it won't break from application of too much force during removal. If the carbon tape being used is new, press a clean glove against it a few times to reduce the stickiness. The standard settings used on the FIB are 2 kV accelerating voltage and spot 3 (53 pA).

Take a picture at 5000x for each electrode with the 10 μm square alignment marks visible. During the capture the contrast may need to be turned to near 100% and then back down as the beam scans along the membrane so that the tubes are visible. Find the best nanotubes on the membrane and take a high magnification picture.

If the nanotube density is too high, plasma clean the square in either the Tegal Asher or the Technics FRIE (using O_2 only) for 2-3 minutes; alternatively, a piranha etch will remove the tubes as well. If the density is low, plasma cleaning is optional. In either case, redeposit tubes until the desired density is attained.

The Labview VI "EbeamMaskWriter.vi" allows one to create the pattern used by the

Vistec e-beam writer. Load the 5000x picture for each electrode, draw contacts to the nanotube's position using the closed polygon tool, draw alignment marks, specify whether the electrode is the left, middle, or right one, and add the grid of squares. Move the big alignment squares to a location on the membrane away from the contacts. Delete the squares that lay on or near the nanotube itself and save the file. The pattern will be saved as an AutoCAD .scr script file.

Run these three script files in AutoCad, and save the resulting pattern as a .dxf file. This .dxf file can be converted to a .gds file using LinkCAD, which is installed in the nanolab office. Using the CATS program in the ISNC office, convert the .gds file into a .gpf file with a resolution between 5 and 40 nm.

C.0.16 Electron-beam Lithography

With the 12.6 mm by 12.6 mm e-beam square in the spin coater, place 3 to 4 drops of PMMA A4 e-beam resist to cover the square (make sure the PMMA is not expired). Spin the square for 45 seconds at 6000 rpm, again ramping at 1000 rpm/sec. Bake the resist on a hot plate set at 180 °C for 15 minutes.

Load the chip into the Vistec e-beam writer, and expose the patterns at 100 keV with a dose of 1400 μC/cm^2. Immerse the chip in a solution of MIBK:IPA in a 1:3 ratio for 45 secs, rinse in IPA, and N_2 blow dry. Check the exposure in the optical microscope. The exposed areas will have a faint blue outline, and the alignment marks should appear to line up at this magnification. If there is a macroscopic misalignment (probably ¿ 5 μm), remove the PMMA with a 5 minute acetone soak and redo the lithography.

Use the New CHA to deposit 500 Åof Pd at 1 Å/s and 800 Åof Au at 3 Å/s. This recipe is 4 on the CHA. Be sure to check that recipe 4 on the controller is set up for Pd/Au before running. The process takes about 3 hours. Lift off by immersion in acetone for 60 minutes. While not necessary, a gentle stirring of the acetone or adding more on the chip with the spray bottle during liftoff helps expedite the process.

C.0.17 Post-Lithography Characterization

Anneal the chips by heating to 300 °C on a hotplate for 20 minutes. If using the Macor/aluminum hotplate, set the variac to 61%, which allows the aluminum to reach about 305 °C at equilibrium. Using the diamond scribe, cut the square into the individual chips by applying pressure straight down on the top side opposite the KOH cleavage lines.

Probe each device in the probe station. Be sure to turn the Keithley on prior to touching the probes to the chips, and test the connection by shorting the two probes on a pad before probing any devices. This also ensures that the probes will discharge safely in the case of accumulated potential. Probe the devices with an IV of maximum voltage .001 V to prevent destroying the nanotubes in air. Record the low bias resistances.

C.0.18 HF Vapor Etch

Pour a small amount of 49% concentrated HF into the small Teflon beaker. The HF should level should be about a centimeter, but no higher than halfway up the beaker. Using plastic tweezers, position the chips to be etched on the Teflon carrier such that the center of the chip is above one of the holes. Place the carrier on top of the Teflon beaker and begin timing. An etch time for 25 seconds is about sufficient for 300 μm thick SiO2. For 800 μm thick, 4 minutes seems to be ideal. One of the by-products of the etch is H_2O, which can build up on the bottom of the chip and rupture the membrane violently if it evaporates and the etch hasn't finished. For this reason, it might prove prudent to etch only in 30 second chunks. Be very careful while handling the HF and always wear safety equipment!

C.0.19 Final Processing

Take the chips to the FIB, and image at 10 kV spot 3 (.13 nA). Now that the tubes should be connected to at least one electrode they will prove much easier to image, and the higher accelerating voltage produces a picture that can tell if the tube connected is actually 2 tubes, and so forth.

Sometimes due to bad liftoff from the optical lithography, the ebeam contacts will be

broken where they should connect to the optical contacts. Also, perhaps one of the optical contacts is scratched/broken somewhere. In either case, the FIB can deposit Pt using the e-beam to mend these contacts. If the break is ¿ 5 μm away from the nanotube, it will usually survive the process (not the case if ion beam deposition is performed).

Anneal once more at 300 °C. Perform a final probe on the good chips, recording the intact devices. These chips are now ready for TEM.

References

[1] SCHOTT, "Optical Glass Collection Datasheet," 2011.

[2] H. S. Skulason, P. E. Gaskell, and T. Szkopek, "Optical reflection and transmission properties of exfoliated graphite from a graphene monolayer to several hundred graphene layers.," *Nanotechnology*, vol. 21, p. 295709, July 2010.

[3] O. Lummer and E. Pringsheim *Transactions of the German Physical Society*, vol. 2, p. 163, 1900.

[4] H. Rubens and F. Kurlbaum *Proceedings of the Imperial Academy of Science*, p. 929, 1900.

[5] W. Wien *Report of the Paris Congress*, vol. 2, p. 40, 1900.

[6] M. Planck, "On the Law of Distribution of Energy in the Normal Spectrum On the Law of Distribution of Energy in the Normal Spectrum," *Annalen der Physik*, vol. 4, p. 553, 1901.

[7] L. Spietz, K. W. Lehnert, I. Siddiqi, and R. J. Schoelkopf, "Primary electronic thermometry using the shot noise of a tunnel junction.," *Science*, vol. 300, p. 1929, June 2003.

[8] G. Begtrup, K. Ray, B. Kessler, T. Yuzvinsky, H. Garcia, and A. Zettl, "Probing Nanoscale Solids at Thermal Extremes," *Physical Review Letters*, vol. 99, p. 155901, Oct. 2007.

[9] J. C. Mather, E. S. Cheng, J. Eplee, R. E., R. B. Isaacman, S. S. Meyer, R. A. Shafer, R. Weiss, E. L. Wright, C. L. Bennett, N. W. Boggess, E. Dwek, S. Gulkis, M. G. Hauser, M. Janssen, T. Kelsall, P. M. Lubin, J. Moseley, S. H., T. L. Murdock, R. F. Silverberg, G. F. Smoot, and D. T. Wilkinson, "A preliminary measurement of the cosmic microwave background spectrum by the Cosmic Background Explorer (COBE) satellite," *Astrophysical Journal*, vol. 354, p. L37, 1990.

[10] B. W. Mangum, "The new International Temperature Scale of 1990 (ITS-90).," *Metrologia*, vol. 27, p. 3, Mar. 1990.

[11] F. Reif, *Customized Complete Statistical Physics*. San Francisco: McGraw-Hill, 1998.

[12] R. G. Ames and T. S. Edwards, "Theoretical Analysis of the Uncertainties Associated with Optical Pyrometry Techniques," in *42nd AIAA Aerospace Sciences Meeting and Exhibit*, 2004.

[13] P. B. Coates, "Multi-Wavelength Pyrometry," *Metrologia*, vol. 17, p. 103, 1981.

[14] G. B. Hunter and T. W. Eagar, "Multiwavelength pyrometry : an improved method," *Optical Engineering*, vol. 24, p. 1081, 1985.

[15] C.-D. Wen and I. Mudawar, "Emissivity characteristics of polished aluminum alloy surfaces and assessment of multispectral radiation thermometry (MRT) emissivity models," *International Journal of Heat and Mass Transfer*, vol. 48, p. 1316, Mar. 2005.

[16] K. S. Novoselov, a. K. Geim, S. V. Morozov, D. Jiang, Y. Zhang, S. V. Dubonos, I. V. Grigorieva, and a. a. Firsov, "Electric field effect in atomically thin carbon films.," *Science*, vol. 306, p. 666, Oct. 2004.

[17] S. Berciaud, M. Y. Han, K. F. Mak, L. E. Brus, P. Kim, and T. F. Heinz, "Electron and Optical Phonon Temperatures in Electrically Biased Graphene," *Physical Review Letters*, vol. 104, p. 227401, June 2010.

[18] V. Perebeinos and P. Avouris, "Inelastic scattering and current saturation in graphene," *Physical Review B*, vol. 81, p. 195442, May 2010.

[19] M. Freitag, H.-Y. Chiu, M. Steiner, V. Perebeinos, and P. Avouris, "Thermal infrared emission from biased graphene.," *Nature nanotechnology*, vol. 5, p. 497, July 2010.

[20] D. Yu and L. Dai, "Voltage-induced incandescent light emission from large-area graphene films," *Applied Physics Letters*, vol. 96, p. 143107, 2010.

[21] M. Engel, M. Steiner, A. Lombardo, and A. C. Ferrari, "Light-matter interaction in a microcavity-controlled graphene transistor." 2012.

[22] R. R. Nair, P. Blake, a. N. Grigorenko, K. S. Novoselov, T. J. Booth, T. Stauber, N. M. R. Peres, and a. K. Geim, "Fine structure constant defines visual transparency of graphene.," *Science (New York, N.Y.)*, vol. 320, p. 1308, June 2008.

[23] V. G. Kravets, a. N. Grigorenko, R. R. Nair, P. Blake, S. Anissimova, K. S. Novoselov, and a. K. Geim, "Spectroscopic ellipsometry of graphene and an exciton-shifted van Hove peak in absorption," *Physical Review B*, vol. 81, p. 155413, Apr. 2010.

[24] M. Liu, X. Yin, E. Ulin-Avila, B. Geng, T. Zentgraf, L. Ju, F. Wang, and X. Zhang, "A graphene-based broadband optical modulator.," *Nature*, vol. 474, p. 64, June 2011.

[25] S. Thongrattanasiri, F. Koppens, and F. García de Abajo, "Complete Optical Absorption in Periodically Patterned Graphene," *Physical Review Letters*, vol. 108, p. 047401, Jan. 2012.

[26] V. G. Zubko, V. Mennella, L. Colangeli, and E. Bussoletti, "Optical constants of cosmic carbon analogue grains - I. Simulation of clustering by a modified continuous distribution of ellipsoids," *Mon. Not. R. Astron. Soc.*, vol. 282, p. 1321, 1996.

[27] E. Krugel, *The Physics of Interstellar Dust*. Philadelphia: Institute of Physics Publishing, 2003.

[28] K. Kim, W. Regan, B. Geng, B. Alemán, B. M. Kessler, F. Wang, M. F. Crommie, and A. Zettl, "High-temperature stability of suspended single-layer graphene," *physica status solidi (RRL) - Rapid Research Letters*, vol. 4, p. 302, Nov. 2010.

[29] K. Zhang, G. M. Stocks, and J. Zhong, "Melting and premelting of carbon nanotubes," *Nanotechnology*, vol. 18, p. 285703, July 2007.

[30] J.-J. Greffet, R. Carminati, K. Joulain, J.-P. Mulet, S. Mainguy, and Y. Chen, "Coherent emission of light by thermal sources.," *Nature*, vol. 416, p. 61, Mar. 2002.

[31] L. J. Klein, H. F. Hamann, Y.-Y. Au, and S. Ingvarsson, "Coherence properties of infrared thermal emission from heated metallic nanowires," *Applied Physics Letters*, vol. 92, p. 213102, 2008.

[32] R. Saito, G. Dresselhaus, and M. S. Dresselhaus, *Physical Properties of Carbon Nanotubes*. London: Imperial College Press, 1998.

[33] T. Stauber, N. Peres, and A. Geim, "Optical conductivity of graphene in the visible region of the spectrum," *Physical Review B*, vol. 78, p. 085432, Aug. 2008.

[34] M. Mecklenburg, J. Woo, and B. C. Regan, "Tree-level electron-photon interactions in graphene," *Physical Review B*, vol. 81, p. 245401, June 2010.

[35] L. D. Landau and E. M. Lifshitz, *Theory of Elasticity*. Butterworth Heinemann, 3rd ed., 1986.

[36] A. G. Worthing, "Atomic Heats of Tungsten and of Carbon at Incandescent Temperatures," *Physical Review*, vol. 12, p. 199, 1918.

[37] I.-K. Hsu, R. Kumar, A. Bushmaker, S. B. Cronin, M. T. Pettes, L. Shi, T. Brintlinger, M. S. Fuhrer, and J. Cumings, "Optical measurement of thermal transport in suspended carbon nanotubes," *Applied Physics Letters*, vol. 92, p. 063119, 2008.

[38] V. Deshpande, S. Hsieh, A. Bushmaker, M. Bockrath, and S. Cronin, "Spatially Resolved Temperature Measurements of Electrically Heated Carbon Nanotubes," *Physical Review Letters*, vol. 102, p. 105501, Mar. 2009.

[39] P. Collins, M. Hersam, M. Arnold, R. Martel, and P. Avouris, "Current Saturation and Electrical Breakdown in Multiwalled Carbon Nanotubes," *Physical Review Letters*, vol. 86, p. 3128, Apr. 2001.

[40] E. Pop, D. Mann, J. Cao, Q. Wang, K. Goodson, and H. Dai, "Negative Differential Conductance and Hot Phonons in Suspended Nanotube Molecular Wires," *Physical Review Letters*, vol. 95, p. 155505, Oct. 2005.

[41] H.-Y. Chiu, V. Deshpande, H. Postma, C. Lau, C. Mikó, L. Forró, and M. Bockrath, "Ballistic Phonon Thermal Transport in Multiwalled Carbon Nanotubes," *Physical Review Letters*, vol. 95, p. 226101, Nov. 2005.

[42] G. Chen, *Nanoscale Energy Transport and Conversion: A Parallel Treatment of Electrons, Molecules, Phonons, and Photons*. New York: Oxford University Press, 2005.

[43] C. F. Bohren and D. R. Huffman, *Absorption and Scattering of Light by Small Particles*. New York: Wiley, 1983.

[44] M. a. van Dijk, a. L. Tchebotareva, M. Orrit, M. Lippitz, S. Berciaud, D. Lasne, L. Cognet, and B. Lounis, "Absorption and scattering microscopy of single metal nanoparticles.," *Physical chemistry chemical physics : PCCP*, vol. 8, p. 3486, Aug. 2006.

[45] M. Rosenberg, R. D. Smirnov, and a. Y. Pigarov, "On thermal radiation from heated metallic dust grains," *Journal of Physics D: Applied Physics*, vol. 41, p. 015202, Jan. 2008.

[46] C. F. Bohren and D. R. Huffman, "Absorption cross-section maxima and minima in IR absorption bands of small ionic ellipsoidal particles," *Applied Optics*, vol. 20, p. 959, 1981.

[47] Z. Liu, A. Bushmaker, M. Aykol, and S. B. Cronin, "Thermal Emission Spectra from Individual Suspended Carbon Nanotubes," *Nano Letters*, vol. 5, p. 4634, 2011.

[48] H. Seidel, L. Csepregi, A. Heuberger, and H. Baumgartel, "Anisotropic Etching of Crystalline Silicon in Alkaline Solutions: I. Orientation Dependence and Behavior of Passivation Layers," *J. Electrochem. Soc.*, vol. 137, p. 3612, 1990.

[49] Z. Chen, J. Appenzeller, J. Knoch, Y.-m. Lin, and P. Avouris, "The role of metal-nanotube contact in the performance of carbon nanotube field-effect transistors.," *Nano letters*, vol. 5, p. 1497, July 2005.

[50] Q. Ngo, S. Krishnanl, A. Stimpfle, M. Meyappan, and C. Y. Yang, "Schottky Barrier Behavior of Metallic Multi-wall Carbon Nanotube- on-Metal Systems," *4th IEEE Conference on Nanotechnology*, p. 119, 2004.

[51] B. Zhang and J. Zerubia, "Gaussian approximations of fluorescence microscope point-spread function models," *Applied Optics*, vol. 46, p. 1819, 2007.

[52] M. Islam, D. Milkie, C. Kane, A. Yodh, and J. Kikkawa, "Direct Measurement of the Polarized Optical Absorption Cross Section of Single-Wall Carbon Nanotubes," *Physical Review Letters*, vol. 93, p. 37404, July 2004.

[53] Y. Murakami, E. Einarsson, T. Edamura, and S. Maruyama, "Polarization Dependence of the Optical Absorption of Single-Walled Carbon Nanotubes," *Physical Review Letters*, vol. 94, p. 087402, Mar. 2005.

[54] J. Hwang, H. Gommans, A. Ugawa, H. Tashiro, R. Haggenmueller, K. Winey, J. Fischer, D. Tanner, and A. Rinzler, "Polarized spectroscopy of aligned single-wall carbon nanotubes," *Physical Review B*, vol. 62, p. R13310, Nov. 2000.

[55] P. Li, K. Jiang, M. Liu, Q. Li, S. Fan, and J. Sun, "Polarized incandescent light emission from carbon nanotubes," *Applied Physics Letters*, vol. 82, p. 1763, 2003.

[56] Y. Wang, K. Kempa, B. Kimball, J. B. Carlson, G. Benham, W. Z. Li, T. Kempa, J. Rybczynski, A. Herczynski, and Z. F. Ren, "Receiving and transmitting light-like radio waves: Antenna effect in arrays of aligned carbon nanotubes," *Applied Physics Letters*, vol. 85, p. 2607, 2004.

[57] E. Cubukcu, F. Degirmenci, C. Kocabas, M. a. Zimmler, J. a. Rogers, and F. Capasso, "Aligned carbon nanotubes as polarization-sensitive, molecular near-field detectors.," *Proceedings of the National Academy of Sciences of the United States of America*, vol. 106, p. 2495, Feb. 2009.

[58] A. Hartschuh, H. N. Pedrosa, L. Novotny, and T. D. Krauss, "Simultaneous fluorescence and Raman scattering from single carbon nanotubes.," *Science (New York, N.Y.)*, vol. 301, p. 1354, Sept. 2003.

[59] J. Lefebvre, J. Fraser, P. Finnie, and Y. Homma, "Photoluminescence from an individual single-walled carbon nanotube," *Physical Review B*, vol. 69, p. 075403, Feb. 2004.

[60] D. Mann, Y. K. Kato, A. Kinkhabwala, E. Pop, J. Cao, X. Wang, L. Zhang, Q. Wang, J. Guo, and H. Dai, "Electrically driven thermal light emission from individual single-walled carbon nanotubes.," *Nature nanotechnology*, vol. 2, p. 33, Jan. 2007.

[61] S. Moritsubo, T. Murai, T. Shimada, Y. Murakami, S. Chiashi, S. Maruyama, and Y. Kato, "Exciton Diffusion in Air-Suspended Single-Walled Carbon Nanotubes," *Physical Review Letters*, vol. 104, p. 247402, June 2010.

[62] A. Jorio, A. G. Souza Filho, V. W. Brar, A. K. Swan, M. S. Ünlü, B. B. Goldberg, A. Righi, J. H. Hafner, C. M. Lieber, R. Saito, G. Dresselhaus, and M. S. Dresselhaus, "Polarized resonant Raman study of isolated single-wall carbon nanotubes: Symmetry selection rules, dipolar and multipolar antenna effects," *Physical Review B*, vol. 65, p. 121402(R), Mar. 2002.

[63] M. Y. Sfeir, F. Wang, L. Huang, C.-C. Chuang, J. Hone, S. P. O'brien, T. F. Heinz, and L. E. Brus, "Probing electronic transitions in individual carbon nanotubes by Rayleigh scattering.," *Science (New York, N.Y.)*, vol. 306, p. 1540, Nov. 2004.

[64] D. Y. Joh, J. Kinder, L. H. Herman, S.-Y. Ju, M. a. Segal, J. N. Johnson, G. K.-L. Chan, and J. Park, "Single-walled carbon nanotubes as excitonic optical wires.," *Nature nanotechnology*, vol. 6, p. 51, Jan. 2011.

[65] S. Berciaud, L. Cognet, P. Poulin, R. B. Weisman, and B. Lounis, "Absorption spectroscopy of individual single-walled carbon nanotubes.," *Nano letters*, vol. 7, p. 1203, May 2007.

[66] R. Agdur, G. Boling, F. Sellberg, and Y. Ohman, "Scattering, Absorption, and Emission of Light by Thin Metal Wires," *Physical Review*, vol. 130, p. 996, 1963.

[67] V. A. Golyk, M. Kruger, and M. Kardar, "Heat radiation from long cylindrical objects." 2011.

[68] Z. G. Zhao, F. Li, C. Liu, and H. M. Cheng, "Light emission and degradation of single-walled carbon nanotube filament," *Journal of Applied Physics*, vol. 98, p. 044306, 2005.

[69] X. Cai, S. Akita, and Y. Nakayama, "Current induced light emission from a multiwall carbon nanotube," *Thin Solid Films*, vol. 464-465, p. 364, Oct. 2004.

[70] Y. Wei, D. Weng, Y. Yang, X. Zhang, K. Jiang, L. Liu, and S. Fan, "Efficient fabrication of field electron emitters from the multiwalled carbon nanotube yarns," *Applied Physics Letters*, vol. 89, p. 063101, 2006.

[71] M. Sveningsson, M. Jonsson, O. a. Nerushev, F. Rohmund, and E. E. B. Campbell, "Blackbody radiation from resistively heated multiwalled carbon nanotubes during field emission," *Applied Physics Letters*, vol. 81, p. 1095, 2002.

[72] Y. Zhang, T. Gong, W. J. Liu, J. Q. Wei, X. F. Zhang, K. L. Wang, M. L. Zhong, and D. H. Wu, "Angle-dependent light emission from aligned multiwalled carbon nanotubes under CO(2) laser irradiation.," *Nanotechnology*, vol. 18, p. 075710, Feb. 2007.

[73] A. E. Aliev and A. A. Kuznetsov, "The origin of polarized blackbody radiation from resistively heated multiwalled carbon nanotubes," *Physics Letters A*, vol. 372, p. 4938, July 2008.

[74] Z. H. Lim, A. Lee, K. Y. Y. Lim, Y. Zhu, and C.-H. Sow, "Systematic investigation of sustained laser-induced incandescence in carbon nanotubes," *Journal of Applied Physics*, vol. 107, p. 064319, 2010.

[75] S. Natarajan, Z. Lim, G. Wee, S. Mhaisalkar, C.-H. Sow, and G. Ho, "Electrically driven incandescence of carbon nanotubes in controlled gaseous environments," *Scripta Materialia*, vol. 64, p. 564, Mar. 2011.

[76] P. Liu, L. Liu, Y. Wei, K. Liu, Z. Chen, K. Jiang, Q. Li, and S. Fan, "Fast High-Temperature Response of Carbon Nanotube Film and Its Application as an Incandescent Display," *Advanced Materials*, vol. 21, p. 3563, Sept. 2009.

[77] P. Rocabois, C. Chatillon, and C. Bernard, "Thermodynamics of the Si-O-N System: I, High-temperature Study of the Vaporization Behavior of Silicon Nitride by Mass Spectrometry," *J. Am. Ceram. Soc.*, vol. 79, p. 1351, 1996.

[78] A. Hashimoto, "Evaporation kinetics of forsterite and implications for the early solar nebula," *Nature*, vol. 347, p. 53, 1990.

[79] J. R. Haines and C. C. Tsai, "Graphite Sublimation Tests for the Muon Collider / Neutrino Factory Target Development Program," Tech. Rep. February, 2002.

[80] W.-h. Zhu, G.-h. Ding, and B. Dong, "The enhanced optical conductivity for zigzag-edge graphene nanoribbons with applied gate voltage," *Applied Physics Letters*, vol. 100, p. 103101, 2012.

[81] T. B. A. Senior, "Half plane edge diffraction," *Radio Science*, vol. 10, p. 645, 1975.

[82] I. Anderson, "Plane Wave Diffraction by a Thin Dielectric Half-Plane," *IEEE Transactions on Antennas and Propagation*, vol. 27, p. 584, 1979.

[83] A. Yazici and A. H. Serbest, "Scattering of Plane Waves by an Anisotropic Dielectric Half-Plane," *IEEE Transactions on Antennas and Propagation*, vol. 47, p. 1476, 1999.

[84] A. A. Balandin, S. Ghosh, W. Bao, I. Calizo, D. Teweldebrhan, F. Miao, and C. N. Lau, "Superior Thermal Conductivity of Single-Layer Graphene," *Nano letters*, vol. 8, p. 902, 2008.

[85] S. Ghosh, I. Calizo, D. Teweldebrhan, E. P. Pokatilov, D. L. Nika, and A. A. Balandin, "Extremely high thermal conductivity of graphene : Prospects for thermal management applications in nanoelectronic circuits," *Applied Physics Letters*, vol. 92, p. 151911, 2008.

[86] S. Adam and S. Das Sarma, "Transport in suspended graphene," *Solid State Communications*, vol. 146, p. 356, 2008.

[87] S. Adam and S. Das Sarma, "Boltzmann transport and residual conductivity in bilayer graphene," *Physical Review B*, vol. 77, p. 115436, Mar. 2008.

[88] S. Adam, E. H. Hwang, V. M. Galitski, and S. Das Sarma, "A self-consistent theory for graphene transport," *PNAS*, vol. 104, p. 18392, 2007.

[89] M.-h. Bae, Z.-y. Ong, D. Estrada, and E. Pop, "Infrared Microscopy of Joule Heating in Graphene Field Effect Transistors," in *9th IEEE Conference on Nanotechnology*, vol. 8, p. 818, 2009.

[90] J.-H. Chen, C. Jang, S. Xiao, M. Ishigami, and M. S. Fuhrer, "Intrinsic and extrinsic performance limits of graphene devices on SiO2.," *Nature nanotechnology*, vol. 3, p. 206, Apr. 2008.

[91] M. Freitag, M. Steiner, Y. Martin, V. Perebeinos, Z. Chen, J. C. Tsang, and P. Avouris, "Energy dissipation in graphene field-effect transistors.," *Nano letters*, vol. 9, p. 1883, May 2009.

[92] a. K. Geim and K. S. Novoselov, "The rise of graphene," *Nature materials*, vol. 6, p. 183, Mar. 2007.

[93] M. V. Gorenstein and G. F. Smoot, "Large-Angular-Scale Anisotropy in the Cosmic Background Radiation," *Astrophysical Journal*, vol. 244, 1981.

[94] E. Hecht, *Optics*. Menlo Park: Addison-Wesley Publishing Company, Inc., 1987.

[95] J. Horng, C.-F. Chen, B. Geng, C. Girit, Y. Zhang, Z. Hao, H. Bechtel, M. Martin, A. Zettl, M. Crommie, Y. Shen, and F. Wang, "Drude conductivity of Dirac fermions in graphene," *Physical Review B*, vol. 83, p. 165113, Apr. 2011.

[96] A. B. Kuzmenko, E. van Heumen, F. Carbone, and D. van der Marel, "Universal Optical Conductance of Graphite," *Physical Review Letters*, vol. 100, p. 117401, Mar. 2008.

[97] Z. Q. Li, E. a. Henriksen, Z. Jiang, Z. Hao, M. C. Martin, P. Kim, H. L. Stormer, and D. N. Basov, "Dirac charge dynamics in graphene by infrared spectroscopy," *Nature Physics*, vol. 4, p. 532, June 2008.

[98] K. M. McCreary, K. Pi, and R. K. Kawakami, "Metallic and insulating adsorbates on graphene," *Applied Physics Letters*, vol. 98, p. 192101, 2011.

[99] H. O. McMahon, "Thermal Radiation from Partially Transparent Reflecting Bodies," *Journal of the Optical Society of America*, vol. 40, p. 376, 1950.

[100] S. Morozov, K. Novoselov, M. Katsnelson, F. Schedin, D. Elias, J. Jaszczak, and A. Geim, "Giant Intrinsic Carrier Mobilities in Graphene and Its Bilayer," *Physical Review Letters*, vol. 100, p. 016602, Jan. 2008.

[101] K. S. Novoselov, a. K. Geim, S. V. Morozov, D. Jiang, M. I. Katsnelson, I. V. Grigorieva, S. V. Dubonos, and a. a. Firsov, "Two-dimensional gas of massless Dirac fermions in graphene.," *Nature*, vol. 438, p. 197, Nov. 2005.

[102] A. A. Penzias and R. W. Wilson, "A Measurement of Excess Antenna Temperature at 4080 Mc/s.," *Astrophysical Journal*, vol. 142, p. 419, 1965.

[103] N. Peres, "Colloquium: The transport properties of graphene: An introduction," *Reviews of Modern Physics*, vol. 82, p. 2673, Sept. 2010.

[104] Y.-W. Tan, Y. Zhang, H. L. Stormer, and P. Kim, "Temperature dependent electron transport in graphene," *The European Physical Journal Special Topics*, vol. 148, p. 15, Sept. 2007.

[105] T. Wehling, M. Katsnelson, and A. Lichtenstein, "Adsorbates on graphene: Impurity states and electron scattering," *Chemical Physics Letters*, vol. 476, p. 125, July 2009.

[106] V. G. Zubko, V. Mennella, L. Colangeli, and E. Bussoletti, "Optical constants of cosmic carbon analogue grains - I. Simulation of clustering by a modified continuous distribution of ellipsoids," *Monthly Notices of the Royal Astronomical Society*, vol. 282, p. 1321, 1996.